University of Nevada, Reno

Relationship Between Magmatism and Mineralization in the RBM Gold Deposit, White Pine County, Nevada

A thesis submitted in partial fulfillment of the requirements for the degree of Master of Science in Geology

by

Daniel W. Pace

John L. Muntean/Thesis Advisor

December, 2009

University of Nevada, Reno
Statewide · Worldwide

THE GRADUATE SCHOOL

We recommend that the thesis
prepared under our supervision by

DANIEL W. PACE

entitled

Relationship Between Magmatism and Mineralization in the RBM Gold Deposit, White Pine County, Nevada

be accepted in partial fulfillment of the
requirements for the degree of

MASTER OF SCIENCE

John L. Muntean, Ph. D., Advisor

Tommy B. Thompson, Ph. D., Committee Member

Victor R. Vasquez, Ph. D., Graduate School Representative

Marsha H. Read, Ph. D., Associate Dean, Graduate School

December, 2009

ABSTRACT

The RBM deposit in the Bald Mountain mining district is a breccia-hosted intrusion-related gold deposit. Petrography, core logging, and mapping of the RBM open pit are used to characterize the deposit in detail and define its relationship to magmatism. Statistical analysis of trace elements from drill core and surface samples from in and around the RBM pit are combined with detailed petrography and microprobe analyses to identify the mineralogical and geochemical signatures of distinct mineralization events. These data define an early mineralization event characterized by potassic alteration, skarn, and hornfels formation that is overprinted by sericitic alteration. Minor gold along with molybdenite, some copper, and base-metal skarn mineralization occurred during this early event. A second mineralization event, which accounts for the bulk of the gold in the deposit is characterized by advanced argillic alteration, free gold, and abundant pyrite in the matrix of magmatic-hydrothermal breccias. This event has a distinct geochemical signature characterized by gold, bismuth, tin, and, to a lesser extent, tellurium. Subsequent mineralization events include late arsenic-rich marcasite mineralization associated with further argillic alteration, and late carbonate-pyrite veins, neither of which appear to be associated with significant gold deposition. Four U/Pb dates on intrusive phases, including one that appears to post-date gold mineralization, define the intrusive system as Jurassic in age. Apatites and zircons were dated using the (U-Th)/He system, and phlogopite was dated using the $^{40}Ar/^{39}Ar$ system in an attempt to define the thermal history and the age of hydrothermal alteration in the

deposit. In addition to the Jurassic hydrothermal activity, these data, along with previously published apatite fission track dates from the district, indicate a later Miocene hydrothermal event that appears to have been a low-temperature (<~170° C), short-duration hydrothermal event with little to no associated gold mineralization.

ACKNOWLEDGMENTS

Thanks to Barrick Gold and the Nevada Bureau of Mines and Geology Student Research Grant for funding this research. Thanks to my advisor John Muntean for strong guidance, constructive criticism, and a high energy level, which rubs off on those around him. Thanks to Tommy Thompson and Warren Rehn for constructive reviews and guidance, and to Victor Vasquez for serving on my committee. This research was developed with an incredible amount of support from Keith Bettles and all the Bald Mountain Geologists whose guidance and constructive discussions throughout the process helped to develop and refine new ideas for the district. A special thanks to all the residents of the Home Ranch for countless hours of discussion and debate. Thanks to Randy, Cheech, and all the CREG students for spirited learning and debate through the long days and nights of Masters research, and to Bets and the roommates for putting up with the resulting schedule. Finally, thanks to Dr. Donald Allen for inspiring me to go west and enter the field of economic geology.

Table of Contents

Table of Tables

List of Figures

I. Introduction

Nevada produces about 80% of the gold in the U.S., making it the fourth largest gold producer in the world (Price, 2008). Most of the gold produced in Nevada comes from Eocene-age Carlin-type deposits, which predominantly occur along two major trends; the Battle Mountain-Eureka trend and the Carlin trend (cf. Hofstra and Cline, 2000; Cline et al., 2005). Along the southern projection of the Carlin trend lies the Bald Mountain mining district, which has produced 3.6 Moz of gold (Morrell et al., 2009). Included within the Bald Mountain mining district are a series of gold deposits in the northern portion of the district that are spatially associated with Jurassic intrusions (Hitchborn et al., 1996; Nutt and Hofstra, 2007), and a series of sedimentary rock-hosted disseminated gold deposits in the southern and eastern part of the district (Ilchik, 1990; Nutt et al., 2000; Nutt and Hofstra, 2003).

Sedimentary rock-hosted disseminated gold mineralization occurs at Alligator Ridge and along the western margin of Mooney Basin, forming a ~40 km north-trending belt of gold deposits and prospects, the best described of which is the Vantage deposit (Ilchik, 1990). In these deposits, gold is hosted in Devonian through Mississippian sedimentary rocks, with most of the ore occurring in thin-bedded units of the Upper Devonian and Lower Mississippian Pilot Shale at the contact between underlying thick-bedded to massive carbonates and overlying calcareous clastic units (Nutt and Hofstra, 2003). Jurassic intrusive rocks are mostly absent from these deposits, however; Jurassic dikes have been dated at the Horseshoe deposit (Nutt et al., 2000; Mortensen et al., 2000). Orebodies form stratabound pods, and are commonly locally focused by fracture-sets or

faults (Ilchik, 1990; Nutt et al., 2000; Nutt and Hofstra, 2003). Deposits are associated with decalcification and silicification of sedimentary rocks (Ilchik, 1990; Nutt and Hofstra, 2003). Gold occurs in arsenian pyrite and is geochemically associated with As, Sb, Hg, and Tl (Nutt and Hofstra, 2003). The association of gold with a distinct stratigraphic horizon, along with the alteration types and geochemical signature, is similar to Carlin-type deposits identified elsewhere in Nevada (Hofstra and Cline, 2000; Cline et al., 2005), and has been used by Ilchik (1990) and Nutt and Hofstra (2003) to characterize them as Carlin-type deposits.

In contrast to the Carlin-type deposits at Alligator Ridge and Mooney Basin, the Bald Mountain deposits to the north have features not shared by most Carlin-type deposits. The gold deposits at Bald Mountain are spatially associated with the Jurassic Bald Mountain stock and Jurassic dikes and sills. The Bald Mountain deposits are hosted in multiple stratigraphic horizons ranging from Cambrian to Mississippian in age. Some deposits show a strong stratigraphic control (e.g., Rat) while others cross-cut multiple stratigraphic horizons (e.g., RBM). Arsenian pyrite mineralization with a similar texture to arsenian pyrite at Alligator Ridge (Ilchik, 1990, Nutt and Hofstra, 2003) is present in some Bald Mountain deposits (e.g., RBM), but the geochemical signature of the gold mineralization includes Bi, Sn, In ± Te (Nutt and Hofstra, 2003, this study), a signature more closely resembling intrusion-related ore deposits (Thompson et al., 1999; Thompson and Newberry, 2000; Lang et al., 2000; Baker et al., 2006), rather than Carlin-type deposits (Ilchik, 1990; Nutt and Hofstra, 2003; Nutt and Hofstra, 2007). The geochemical signature of ore deposits in the north, together with a much higher base

metal contents and spatial association to Jurassic intrusions, has been used by Nutt and Hofstra (2007) to classify the deposits as intrusion-related gold deposits of Jurassic age.

Despite the abundance of Mesozoic intrusions in Nevada, most are not genetically associated to economically significant gold deposits. The most abundant Mesozoic ore deposits in eastern Nevada are related to Cretaceous intrusions, and include the copper-(gold) porphyry, skarn, and sedimentary rock-hosted deposits in the Robinson district near Ely, Nevada (Fournier, 1967; Seedorff et al., 1995); Ag-Pb-Zn-Au carbonate replacement ± skarn mineralization near Eureka, NV (Nolan, 1962; Dilles et al., 1996; Margolis, 1997; Vikre, 1998; Marlowe and Russell, 2004), and polymetallic Au-Ag skarn mineralization at Mount Hamilton ~40 miles south of Bald Mountain (Myers et al., 1991). Jurassic gold mineralization has been identified in eastern Nevada, but is generally low-grade and of little economic significance. Auriferous quartz-base metal sulfide veins with sericitic alteration are associated with the Jurassic Goldstrike stock in the northern Carlin trend, but the gold mineralization associated with this event is considered insignificant compared with the Tertiary Carlin-type mineralization that overprints it (Emsbo et al., 2000; Heitt et al., 2003). In addition, Jurassic gold mineralization occurs with porphyry copper- mineralization in the Dolly Varden Mountains (Atkinson et al., 1982), silver-rich quartz veins spatially associated with quartz monzonite near Austin (Ross, 1953), and Ag-Pb carbonate replacement deposits in the Cortez Range (Stewart and McKee, 1977); however, all of these occurrences are insignificant compared with the 3.6 Moz of Au produced from Bald Mountain. The porphyry copper deposits at Yerington have been Nevada's most economically

significant Jurassic deposits, but are in western Nevada and contain little to no gold (Dilles, 1987).

Given the lack of identified gold mineralization associated with Jurassic intrusions in Nevada, and the presence of Carlin-type mineralization in the southern part of the Bald Mountain mining district, the identification of Jurassic intrusion-related gold deposits at Bald Mountain (Hitchborn et al., 1996; Nutt et al., 2000; Nutt and Hofstra, 2007) has been met with skepticism. In addition, the presence of late arsenian marcasite, a feature generally associated with Carlin-type deposits (cf. Cline et al., 2005), suggests the possibility that Carlin-type mineralization may have overprinted Jurassic mineralization at Bald Mountain, like at Goldstrike (Emsbo et al., 2000). This hypothesis was supported by Schmauder et al. (2005), who obtained Miocene apatite fission track (AFT) dates in and around the north deposits. A district study by Nutt and Hofstra (2007) utilized district-scale mapping, petrography, fluid inclusions, and Pb, S, O, and H isotope data to demonstrate the north deposits were part of a zoned Jurassic reduced intrusion-related gold system, rebutting Schmauder et al.'s (2005) data as being related to exhumation, and possibly later fluids which did not deposit significant gold.

The focus of this study is to document, in detail, a single deposit in the north part of the Bald Mountain district to characterize the time-space relationship between intrusive phases, hydrothermal alteration, and mineralization. Based on the study by Nutt and Hofstra (2007), Bald Mountain includes a central deep deposit (Top), peripheral deep deposits (LJ-ridge, Rat, the Numbers pits, and LBM), and a central shallow deposit (RBM). Strong structural and stratigraphic controls in the peripheral deep deposits resemble Carlin-type mineralization (Nutt and Hofstra, 2007). In contrast, gold

mineralization at RBM, 80% of which had been originally defined to occur in hydrothermally altered quartz-feldspar porphyry, does not show a strong stratigraphic control (Hitchborn et al., 1996; Nutt et al., 2000). In addition, the igneous rocks at RBM are finer grained than those at the Top deposit, and have been interpreted as rhyolite porphyries by Thompson (2004). These characteristics suggest that RBM is a shallow igneous end-member which may preserve the clearest relationship between gold mineralization and igneous activity. At most of the deposits in the north part of the Bald Mountain mining district, deep and pervasive oxidation and supergene advanced argillic alteration has destroyed sulfides and remobilized metals, thereby masking primary lithologies and hypogene alteration and mineralization. This is also the case in the open pit at RBM; however, drilling below the pit has identified unweathered, sulfide-bearing gold mineralization. Included in this sulfide suite are abundant base-metals, characteristic of intrusion-related deposits elsewhere (Lang and Baker, 2001), and fine-grained arsenian marcasite and pyrite, common to Carlin-type deposits in Nevada (Cline et al., 2005). For these reasons RBM appears to be the best deposit to document the association between mineralization and magmatism at Bald Mountain.

Previous work by Hitchborn et al. (1996), Nutt et al. (2000), Schmauder (2005), and Nutt and Hofstra (2007) have documented the association between gold mineralization and intrusions on a district scale. Hitchborn et al. (1996), used petrography and schematic cross-sections to show a spatial association between gold mineralization and sericitic alteration at RBM. Hitchborn et al. (1996) also documented the presence of multiple generations of alteration and mineralization; however, they did not find clear evidence linking gold mineralization to any one event. Schmauder et al.

(2005) used AFT dating coupled with oxygen isotopic data to identify Miocene ± Eocene hydrothermal fluid flow spatially associated with gold deposits; however, the samples were not linked to detailed mapping. Nutt and Hofstra (2007), added Pb, S, O, and H isotope and fluid inclusion data to classify the RBM deposit as a central shallow gold deposit that originally formed above the Top deposit, at 1-3 km depth. As mentioned above, Nutt and Hofstra argued that Schmauder et al.'s AFT dates were the result of exhumation and not hydrothermal alteration. In addition, they used microprobe analyses on multiple generations of pyrite to conclude that late pyrite-phases identified by Hitchborn et al. (1996) replaced earlier sulfides and did not result in the deposition of additional gold, supporting their conclusion that gold mineralization at Bald Mountain is best characterized as a Jurassic reduced intrusion-related gold deposit. Given the possibility that at least 2.4 Moz of gold were deposited during the emplacement of a Jurassic intrusive center at Bald Mountain and the lack of significant, identified, Jurassic gold mineralization elsewhere in the region, it is imperative to document the time-space relationship between intrusions, alteration, and mineralization at the deposit-scale in order to develop a comprehensive deposit model that can be applied to exploration for undiscovered Jurassic gold mineralization in Nevada and elsewhere.

Detailed mapping and core logging, supplemented with transmitted and reflected light petrography, were used to differentiate and describe the intrusive phases present in the RBM pit as well as their relationships to alteration and mineralization. Scanning-electron microscopy was used to document fine-grained mineral phases and their paragenetic relationships. In order to further link gold mineralization with specific paragenetic stages, microprobe analyses on selected samples were used to determine if

pyrite, marcasite, and/or other sulfides contained detectable gold. Statistical analyses on multi-element geochemical data from drilling in and around the RBM deposit were used to document the geochemical signature of mineralization events, and link them with alteration and mineralization as identified in mapping, logging, and petrography. These data are augmented with thermochronology (U-Pb, $^{40}Ar/^{39}Ar$, and (U-Th)/He) to test whether all exposed intrusions at RBM are indeed Jurassic, and to place further constraints on post-Jurassic thermal events that may have transported and deposited significant amounts of gold. The data obtained from this study were then integrated to develop a conceptual model for the formation of the deposit and an exploration model that can be used to discover new deposits.

II. Regional Geology of the Great Basin

The Bald Mountain mining district is located in the central portion of the Great Basin physiographic province. The stratigraphic sequence in the region is characterized by almost continuous sedimentation on the Precambrian craton along the western passive margin of North America from the upper Precambrian to the early Triassic (Stewart, 1980; Speed et al., 1988). Bald Mountain is in the foreland of the Devonian-Mississippian Antler orogeny, which thrust Devonian and older deepwater siliciclastic and basaltic rocks over the continental shelf along the Roberts Mountains thrust fault, and resulted in syn- and post-orogenic sedimentation in the district from erosion of the Antler highlands (Roberts, 1960; Poole et al., 1992; Miller et al., 1988). Mesozoic to early Tertiary Sevier thrusting developed a tectonic regime of southeast-directed compression that developed folds, reverse and thrust faults, and westerly-trending strike-slip faults in the district (Nutt and Hart, 2004; Nutt and Hofstra, 2007). Eocene fluvial and lacustrine sandstone, siltstone, conglomerate, and limestone unconformably overlie Devonian through Permian rocks indicating appreciable Mesozoic and/or early Cenozoic erosion in the Bald Mountain mining district (Nutt et al., 2000). This was followed by large-magnitude Tertiary extension expressed to the north by the Ruby Mountains-East Humbolt Range metamorphic core complex (Snoke and Howard, 1984; Snoke and Lush, 1984; Howard, 2003), and as north-striking normal faults in the Bald Mountain mining district (Nutt, 2000; Nutt and Hart, 2004).

The majority of intrusive rocks in northeastern Nevada were emplaced during three temporally distinct magmatic events. During the first major pulse of magmatism

from 155-165 Ma, intrusions of predominantly granodiorite were emplaced in a north-south belt (Miller and Hoisch, 1995). The belt is well inboard of the magmatic arc along the Jurassic continental margin to the west, and is best characterized as back-arc magmatism (DuBray, 2007). Studies of Jurassic intrusions in eastern Nevada indicate many were emplaced along dilational zones created by crustal-scale east-west oriented strike-slip motion (Miller and Hoisch, 1995). A second pulse of magmatism in the Cretaceous emplaced a series of intrusions from 55 to 120 Ma (DuBray, 2007) and is marked by a shift in magma chemistry and associated mineralization with time. Early Cretaceous intrusions are predominantly quartz-poor metaluminous granodiorites and associated mineralization, when present, is typically chalcophile, such as the porphryry Cu-Au system at Robinson mentioned above. Late Cretaceous intrusions are commonly peraluminous two-mica granites associated with lithophile-element skarn and greisen mineralization (Barton et al., 1988; Barton, 1990).

The third stage of major magmatism, mainly between 35 and 40 Ma in northeastern Nevada (DuBray, 2007), is widespread throughout the Basin and Range (Christiansen and Yeats, 1992). Mineral deposits associated with Tertiary magmatism include porphyry copper and skarn-related mineralization in the Battle Mountain mining district (Theodore and Blake, 1978), and porphyry molybdenum mineralization at Mount Hope (Westra and Riedell, 1996). Low-sulfidation epithermal gold deposits are also present in the Tuscarora volcanic field associated with Eocene intrusions (Castor et al., 2003). Carlin-type deposits, as described above, are temporally though not clearly genetically related to Eocene magmatism. An exception to this is the Cove McCoy system which has alteration patterns and geochemical associations which resemble

Carlin-style gold mineralization, but also contains high base metals, a high silver to gold ratio, and a clear spatial relationship to Early Tertiary intrusions (Johnston et al., 2008).

III. District Geology

Background of Exploration and Development at Bald Mountain

The Bald Mountain mining district is made up of a 380 square kilometer claim block controlled by Barrick Gold Corp. The original claim staked in the district was on silver chloride-bearing outcrops in 1869, near what is now the Top deposit (Hill, 1916). Early mining commenced in the 1870's, with minor Cu, Ag, Sb and Au mined from veins proximal to the Bald Mountain stock, with some veins running up to 31 ppm Au (Nutt et al., 2000). Placer gold was also recovered from Water Canyon on the west side of the range in the late 1800's (Smith and Vanderburg, 1932). Tungsten was discovered in scheelite-bearing skarns along the margins of, and as blocks within, the Bald Mountain stock in the early 1900's, and mined from the Zed Williams area between 1940 and 1950 (Hitchborn et al., 1996). The district was explored for porphyry copper mineralization by Bear Creek Mining Company in the 1950's and 1960's, before it was taken over by Placer Amex, the predecessor to Placer Dome (Nutt et al., 2000). In 1983, Placer Dome began modern gold production in the district with heap-leach production of oxide ore from the number 1 pit. Placer Dome continued mining heap-leachable oxide gold through 2006. Barrick gained control of the property in 2006 with the takeover of Placer Dome, and has continued mining and exploring in the district, with successes including identification of a new zone of gold mineralization southwest of the RBM pit. As of the end of 2008, 2.4 million ounces of gold has been produced from 14 pits on the main claim block, with an additional 1.2 million ounces produced from the south portion of the district and adjacent claims (Fig. 1; Morrell et al., 2008).

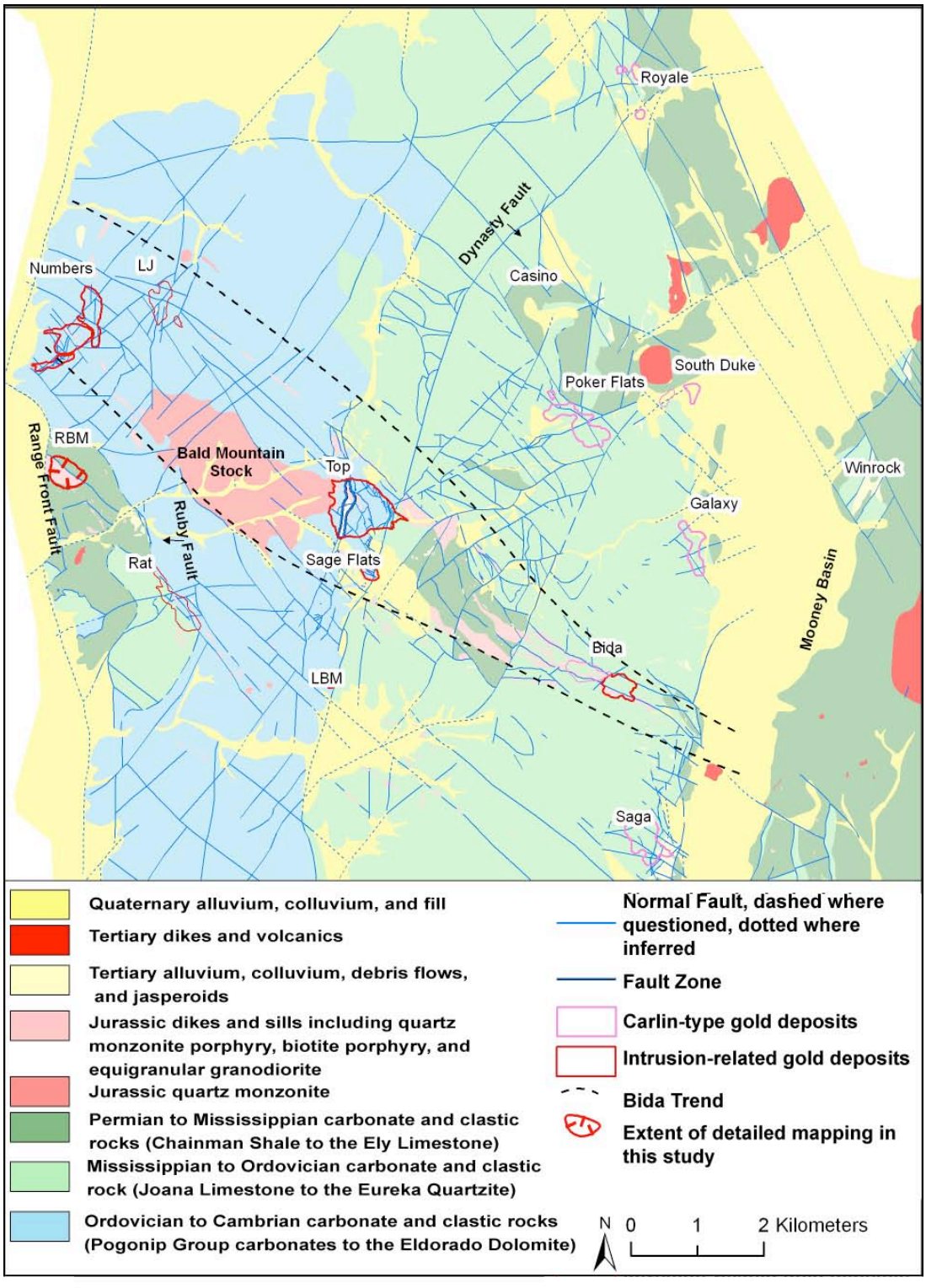

Figure 1. Geologic map of the Bald Mountain mining district compiled by Barrick Geologists.

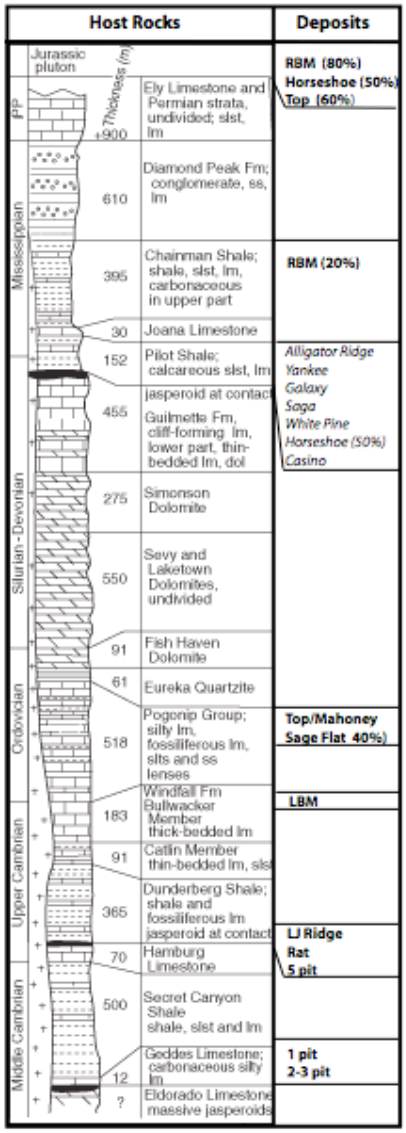

Figure 2. Stratigraphic column of the Paleozoic rocks in the Bald Mountain mining district (modified from Nutt and Hofstra, 2007). Deposits labeled next to respective host rocks. Intrusion-related deposits in bold, Carlin-type deposits in italics.

Stratigraphy

The exposed sedimentary sequence in the Bald Mountain mining district is comprised of Cambrian through Devonian shelf carbonates overlain by Mississippian and Pennsylvanian siliciclastics and lesser shelf-slope carbonates (Fig. 2). Sedimentary rock descriptions are summarized from regional and district-scale studies by Rigby (1960), Hose and Blake (1976), Hitchborn et al. (1996), Nutt et al. (2000), and Nutt and Hart (2004).

The oldest units exposed in the district are a Cambrian sequence of dolomites and limestones with minor shales and cherts. The lowermost unit is the Eldorado Dolomite, a medium- to thick-bedded limestone and dolomite with an upper contact marked by discontinuous to massive jasperoid that is locally brecciated and cemented by later silica. Carbonaceous shale and limestone of the Geddes Limestone conformably overlies the Eldorado Dolomite, and is in turn conformably overlain by thin-bedded silty limestone and limestone correlative with the Secret Canyon Shale. The upper Cambrian Hamburg Limestone overlies the Secret Canyon Shale, and is composed of fine- to medium-grained, thin-bedded to massive limestone. The Dunderburg Shale overlies the Hamburg, and is

made up of silty limestone and interbedded dark gray to black limestone. The Windfall Formation overlies the Dunderburg Shale, and is broken into the Catlin member, composed of light and dark banded cherty limestone at the base that is overlain by thin-bedded limestone with abundant black chert and lesser siltstone and sandstone, and the Bullwacker member, which is predominantly limestone.

Ordovician through Devonian units are composed of limestones, sandstones, and dolomites. The Ordovician Pogonip Group is made up of the Goodwin, Ninemile, and Antelope Valley formations, and is composed of thin-bedded to massive, locally cherty and locally bioclastic limestone and dolomite. The Eureka Quartzite is a white to medium gray, dense quartzite that overlies the Pogonip, and is the best marker bed in the district. The Fish Haven Dolomite overlies the Eureka Quartzite, and is a pale brown to dark grey dolomite with abundant gray to black chert along laminations. The Silurian to middle Devonian sequence is made up of a series of thick-bedded dolomites of the Laketown and Sevy Dolomites, and thin-bedded dolomite with abundant sand lenses of the Simonson Dolomite. The upper Devonian Guilmette is a relatively pure limestone with subordinate dolomite, and is commonly altered to jasperoid along its upper contact.

The Mississippian sequence at Bald Mountain is characterized by increasing clastic input from the Devonian-Mississippian Antler highlands to the west. The lowermost Pilot Shale is a calcareous shale and siltstone locally interbedded with thin limestone. The Joanna limestone overlies the Pilot Shale; it is a crinoid-rich limestone with abundant chert lenses. The Chainman Shale, which overlies the Joanna, is predominantly shale with local siltstone and thin-bedded limestone. The Chainman Shale grades upward into the Diamond Peak Formation, which is predominantly a chert pebble

conglomerate and sandstone at Bald Mountain. Sandstone lenses in the upper Chainman, and siltstone in the lower Diamond Peak, make this contact difficult to define. A more detailed description of the Chainman Shale and Diamond Peak Formation in the RBM area is presented below

Intrusive Rocks

The sedimentary sequence is intruded by the Jurassic Bald Mountain stock, as well as a series of Jurassic dikes and sills. Limited exposures of Tertiary rhyolitic tuffs, flows and porphyry dikes occur at Bald Mountain, mainly within the Mooney Basin and west of the Rat pit (Mortensen et al., 2000; Nutt and Hart, 2004). Seven phases of intrusive rocks have been identified in previous studies of the Bald Mountain mining district (Table 1). An aplite sill is the oldest intrusive rock in the district. Aplite crops out in the #3 pit as a shallow dipping north to northeast trending sill with an average grain size of <1 mm (Hitchborn et al., 1996). A U/Pb date of 185.9 ± 3.8 Ma by Mortensen et al. (2000) is a minimum emplacement age for the aplite sill. The largest intrusion in the district is the Bald Mountain stock, a 4 km by 2 km, northwest-trending body that intrudes Cambrian and Ordovician country rocks (Fig. 1) (Hitchborn et al., 1996). The stock is mostly a coarse-grained orthoclase-biotite-hornblende-quartz monzonite (Nutt and Hofstra, 2007), although is described by Hitchborn et al. (1996) as a composite stock that contains quartz monzonitic, granodioritic, and granitic phases. The stock is surrounded by a metamorphic aureole up to 1.5 km wide (Hitchborn et al., 1996; Nutt and Hofstra, 2007). Quartz-feldspar porphyry dikes 1 to 30 m thick with strike lengths in excess of 2,000 m crop out along the Bida trend, a large-scale structural feature described

below (Hitchborn et al., 1996). The mineralogy of quartz-feldspar porphyry dikes is similar to that of the main Bald Mountain stock, but the dikes have a clear porphyry texture characterized by a fine-grained groundmass and ~30% phenocrysts (Hitchborn et al., 1996). Porphyry dikes cross-cut the aplite sill in the #3 pit (Nutt et al., 2000). Zircons from the Bald Mountain stock, as well as 6 quartz-feldspar porphyry dikes from the district, have been dated using U/Pb, and all dates overlap at ~159 Ma (Fig. 3, Table 2) (Mortensen et al., 2000). Potassium-argon dates from Hitchborn et al. (1996) for the Bald Mountain stock range from 157.1 ± 5.1 to 139.3 ± 4.2 Ma. A potassium-argon date of 146.7 ± 4.4 Ma was also published by Hitchborn et al. (1996) from quartz-feldspar porphyry in the RBM pit. These young ages likely represent cooling ages of the intrusive system or partial argon loss from subsequent hydrothermal activity and/or weathering rather than emplacement ages for intrusions.

Unit	Rock Description / Mineralogy	Distribution
Aplite Sills (Hitchborn et al., 1996)	Light gray to white equigranular rock with an average grain size <1mm.	Shallow-dipping northeast-trending sills exposed in the number 3 pit.
Bald Mountain stock (Hitchborn et al., 1996)	Light to medium grained seriate to porphyritic rock with distinctive euhedral 1-4 cm pink orthoclase phenocrysts with biotite inclusions as well as plagioclase, biotite, hornblende, and accessory apatite and zircon (the size of phenocrysts is not documented). Ilmenite (<1vol %) and very minor magnetite identified by Nutt and Hofstra (2007)	Roughly elliptical, northwest-trending 4 x 2 km composite stock that includes quartz monzonitic, granodioritic, and granitic phases.
Quartz-feldspar porphyry dikes (Hitchborn et al., 1996)	Phenocrysts include 20-25% euhedral plagioclase, 10-25% quartz, and <5% subhedral biotite in a light gray groundmass.	Dominantly northwest-trending 1 to 30 m thick dikes along the Bida Trend; lesser plug-like bodies east of the Bald Mountain stock
Mafic dikes/Lamprophyres (Hitchborn et al., 1996)	Composed of hornblende, plagioclase, biotite, and Fe-Ti oxides	Mostly as dikes cutting the Bald Mountain stock, also present in the Numbers pits.
Lamprophyre (Nutt et al., 2000)	Principally composed of phlogopite, plagioclase, and minor dolomite (possibly an alteration mineral) with embayed quartz interpreted as xenocrysts. Titanomagnetite and Cr-magnetite identified by Nutt and Hofstra (2007).	Occurs at LJ Ridge.
Ultramafic dike (Nutt et al., 2000)	Primary mineralogy unknown. Altered to vermiculite, talc, clinochlore, and calcite with 23% Mg, 1,500 ppm Cr, and 900 ppm Ni.	Number 3 pit.
Quartz feldspar mafic porphyry (Wright, 2006)	Similar to quartz-feldspar porphyry but with small sparse quartz phenocrysts and 5-15% biotite.	Dikes that include the main dike in the Rat pit, though this lithology has only recently been mapped as a distinct phase.
Basaltic andesite (Wright, 2006)	Dark fine-grained dikes with a felted hornblende-plagioclase groundmass and subhedral to resorbed potassium feldspar and quartz xenocrysts.	Identified along Main Gold Road and LJ haul road.
Porphyry dike (Nutt et al., 2000)	Clay-altered, No mineralogy reported	East side of Mooney Basin

Table 1. Table of intrusive phases identified in the Bald Mountain mining district prior to this study. Mafic phases identified by Nutt et al. (2000), Hitchborn et al. (1996), and Wright (2006) likely overlap however rock type descriptions are not sufficient to identify if they are the same or different phases. Thompson (2004) described the intrusive phases at Bald Mountain with a different nomenclature that has not been used in published works, and is therefore not listed here.

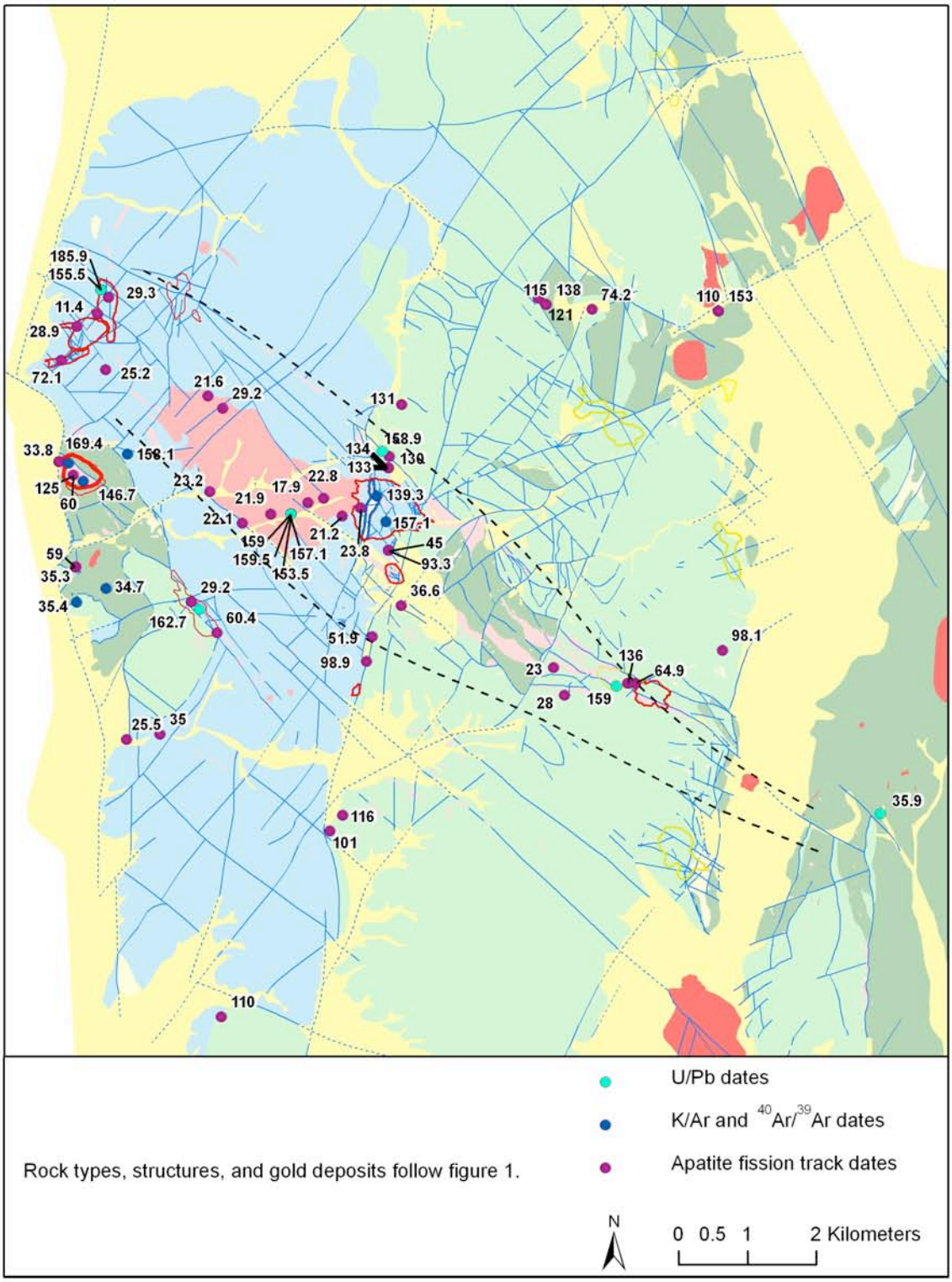

Figure 3. Geologic map of the Bald Mountain mining district with dates from previous studies labeled.

Age (Ma)	Error (2-σ)	Location	Unit	Dating Method	Reference	Sample Location X_SP	Y_SP
159	0.5	Geographic center of the pluton	Bald Mountain stock	U/Pb zircon	Mortensen et al. 2000	507220	1889972
159.5	1	Geographic center of the pluton	Bald Mountain stock	U/Pb unabraided titanite	Mortensen et al. 2000	507220	1889972
155.5	+7.7/ -8.8	#3 pit	Sparsely quartz phyric intermediate to felsic dike	U/Pb zircon	Mortensen et al. 2000	498159	1900697
185.9	3.8	East highwall of #3 pit	Aplite sill	U/Pb zircon	Mortensen et al. 2000	498159	1900697
152.6 - 153.4		South Rat pit	Sparsely quartz phyric porphyry dike	U/Pb zircon	Mortensen et al. 2000	502868	1885427
162.7	4.9	South Rat pit	Sparsely quartz phyric porphyry dike	U/Pb zircon tips	Mortensen et al. 2000	502868	1885427
158.9	0.4	North Sky prospect	Coarsely quartz phyric porphyry dike	U/Pb zircon	Mortensen et al. 2000	511590	1892976
158.5	8.7	North Sky prospect	Coarsely quartz phyric porphyry dike	U/Pb zircon needles	Mortensen et al. 2000	511590	1892976
159	0.7	Horseshoe pit	QFP dike	U/Pb zircon	Mortensen et al. 2000	522780	1881752
139.3	4.2	Bottom of Top pit	Stock (slightly altered)	K/Ar - phenocrystic biotite	Hitchborn et al. 1996	511340	1890836
153.5	5	not reported	Unaltered stock	K/Ar - phenocrystic biotite	Hitchborn et al. 1996	507220	1889972
157.1	5.1	not reported	Unaltered stock	K/Ar - phenocrystic biotite	Hitchborn et al. 1996	507220	1889972
158.1	5	900 m northeast of RBM	Unaltered QFP dike	K/Ar - phenocrystic biotite	Hitchborn et al. 1996	499426	1892845
146.7	4.4	Southeastern end of RBM pit	Pervasively altered porphyry	K/Ar - phenocrystic biotite	Hitchborn et al. 1996	497309	1891534
35.9	0.1	East side of Mooney Basin	Clay-altered quartz porphyry dike	U/Pb zircon	Mortensen et al. 2000	535386	1875662
36.27	0.11	Just east of map	Rhyolite	$^{40}Ar/^{39}Ar$ biotite	Nutt Map 145 cites R.J. Fleck, Oral Commun. 1999	uk	uk
36.56	0.1	Just east of map	Rhyolite	$^{40}Ar/^{39}Ar$ biotite	Nutt Map 145 cites R.J. Fleck, Oral Commun. 1999	uk	uk
35.4	0.9	1.5 km west of Rat pit	Crystal tuff	K/Ar biotite	Nutt cites Placer Dome 2003	496985	1885771
34.7	0.9	1 km west of Rat pit	Crystal tuff	K/Ar sanidine	Nutt cites Placer Dome 2003	498401	1886435

Table 2. Table of previously published dates for the Bald Mountain mining district with the dating method, location, and brief rock description provided in previous studies. Some K/Ar dates may be partially reset. AFT dates are not included in this table. Coordinates are in Nevada East State Plane, NAD27. Uk = unknown sample location.

Mafic dikes composed of hornblende, plagioclase, biotite, and Fe-Ti oxides cut quartz feldspar porphyry dikes, and locally contain xenocrysts of the Bald Mountain stock (Hitchborn et al., 1996). Lamprophyres have also been reported in the district, but are difficult to distinguish from mafic dikes, based on the published descriptions (Hitchborn et al., 1996; Nutt et al., 2000; Nutt and Hofstra, 2007; Wright, 2006). Lamprophyre dikes are primarily composed of phlogopite and plagioclase with minor dolomite (possibly an alteration product) and embayed quartz xenoliths (Nutt et al., 2000). Xenoliths of lamprophyre in quartz-feldspar porphyry dikes, and xenoliths of quartz-feldspar porphyry in lamprophyre dikes, indicate lamprophyre emplacement preceded, accompanied, and post-dated quartz-feldspar porphyry emplacement (Nutt and Hofstra, 2007).

Tertiary magmatism is present as tuffs and dikes in the Bald Mountain mining district. Placer Dome obtained K-Ar dates from biotite and sanidine in two samples of crystal-rich tuff, located about 1.5 km south of the RBM deposit. They were 35.4 ± 0.9 Ma and 34.7 ± 0.9 Ma, respectively (reported by Nutt and Hart, 2004). The dated samples overlie Eocene conglomerates and sandstones with fragments of Diamond Peak quartzite, volcaniclastic rocks, and silicified fine-grained rock (Nutt and Hart, 2004). Similar tuff is mapped in Mooney Basin and Alligator Ridge (Nutt and Hart, 2004). Zircons from a quartz-biotite-feldspar porphyry dike at the northern end of Alligator Ridge were dated by Mortensen et al. (2000) and yielded a U/Pb age of 35.9 ± 0.1 Ma. Nutt and Hofstra (2007) claim this dike was altered to clay; however, the alteration was not described by Mortensen et al. (2000). Similar ages have been obtained using $^{40}Ar/^{39}Ar$ on sanidine from reworked quartz-biotite tuff in Mooney Basin (Nutt, 2000).

Late Tertiary to modern geothermal activity in the district is indicated by a large travertine dome in the basin to the west of the RBM deposit, and warm surface springs at the Warm Springs Ranch ~8 miles to the southwest of the RBM deposit.

Structure

There are two dominant structural trends present in the northern portion of the Bald Mountain mining district. The Bida trend is a series of northwest-trending en-echelon faults with limited strike lengths that appear to control emplacement of the Jurassic Bald Mountain stock and associated dikes (Hitchborn et al., 1996; Nutt et al., 2000; Nutt and Hofstra, 2007). The trend is interpreted as a deep crustal scale fault zone based on the structural control of the Bald Mountain stock, the presence of lamprophyre dikes in the stock, stratigraphic facies changes, features consistent with structural inversion, and a magnetotelluric profile (Wannamaker and Doerner, 2002; Nutt and Hart, 2004; Nutt and Hofstra, 2007; Muntean et al., 2007). The amount and sense of displacement along faults of the Bida Trend are unclear; however, Nutt et al. (2000) contend at least part of the motion is strike-slip. A zone of northwest-striking, discontinuous high-angle faults and dikes sub-parallel to the Bida trend is present between the RBM and Rat deposits (Hitchborn et al., 1996; this study). A second structural trend, expressed as a series of north to northeast-striking normal faults, the most prominent of which is the Dynasty fault, cuts the district, and displaces orebodies in the vicinity of the Top deposit (Nutt and Hofstra, 2007). Offsets along the Dynasty fault and sympathetic northeast-striking faults are interpreted as Tertiary in age, although some appear to control intrusions and gold mineralization where they intersect northwest-

trending faults and intrusions in the area around the Top deposit, indicating they may be pre-Jurassic structures reactivated by Tertiary extension (Hitchborn et al., 1996; Nutt and Hart, 2004; Nutt and Hofstra, 2007). Abundant low-angle attenuation faults were mapped along lithologic contacts by Nutt (2000), and are intruded by Jurassic dikes and sills. The sense of displacement on many of these structures is poorly defined.

The Ruby fault is a major north-trending, west-dipping fault that crops out east of the RBM pit. It is expressed as a series of jasperoids and debris flows (Nutt and Hart, 2004). Some of the deeper holes in and around RBM have intercepted relatively unaltered thin-bedded limestones and dolomites overlain by biotite hornfels that are interpreted as the Cambrian Hamburg and Dunderburg formations, respectively, below the strongly altered Jurassic intrusions and Mississippian Chainman Shale that host much of the ore at RBM. The contact is marked by a zone of intense calcite veining and is interpreted to be the Ruby fault. A thick zone of fault gouge or sheared rock is generally absent. The gold mineralization is truncated at this contact, although it has been intercepted below the fault at the Hamburg-Dunderburg contact in one drill hole. Based on the mapped location of the Ruby Fault north and east of the RBM pit, and the intercepts below the RBM pit, the fault flattens considerably at depth. Nutt and Hart (2004) mapped the rocks in and around the RBM deposit as a Miocene to Eocene chaotic unit with slide blocks up to one-half kilometer in the hanging wall of the Ruby fault. The K/Ar dates on the crystal-rich tuff east of the Rat open pit, in the hangingwall of the Ruby fault, indicate the structure was active <35 Ma (Nutt and Hofstra, 2007). Nutt and Hofstra (2007) use the stratigraphic thickness of juxtaposed units across the fault to identify as much as 2.8 km of offset, and identify the RBM deposit itself as a fault block that was downdropped from

what would have been the upper levels of the Top deposit. Mapping in and around the RBM pit indicates that much of the area mapped by Nutt and Hart (2004) as a chaotic unit is intact bedrock (Mach, 2008). The Chainman and Diamond Peak Formations consistently dip 20-35° to the southeast around RBM, over an area of greater than 1 km. In addition, recent drilling in the RBM area has identified a large porphyry system to the south of the current pit with intrusions and alteration zoning delineating a large shallow porphyry system which is most likely related to the RBM deposit itself. The consistent orientation and zoning of intrusions and alteration, as well as the consistent dip of the sedimentary units indicate that this region is intact and, although it may be a large block downdropped along the Ruby fault after mineralization, it is not a chaotic unit as previously mapped.

Gold Deposits

The Bald Mountain mining district is made up of a series of gold deposits, which together have produced more than 3 million ounces of gold from oxide ore. Mineralization in the north deposits is spatially associated with Jurassic intrusions and is hosted in many different stratigraphic intervals, ranging from Cambrian through Mississippian in age (described by Hitchborn et al., 1996). The Top-Sage flats, Numbers, LJ Ridge, and Bida pits as well as historic vein workings and the Zed Williams skarn all lay along and within the northwest-striking Bida trend. The largest of the deposits is the Top-Sage flats deposit where gold is hosted in NE-oriented shear zones cutting the Bald Mountain stock, quartz-biotite-feldspar porphyry dikes, and skarn and recrystallized marbles of the Ordovician Pogonip Group. The 1-5 deposits, collectively termed the

Numbers pits, and the LJ Ridge deposit lie to the northwest of the Top deposit, where gold is hosted in north-striking steeply east-dipping fissures and shear zones within the Cambrian Secret Canyon Shale, the Catlin Member of the Windfall Formation, the Dunderberg Shale, and the Hamburg Formation.

Southeast of the main Bida trend, the LBM, Rat, and RBM deposits form a belt subparallel to the main Bida trend. Gold in the historic LBM deposit is hosted at the intersection of a Bida-parallel fault and the Dynasty fault in the Pogonip Group carbonates. Gold in the Rat deposit is focused along northwest-striking normal faults, with mineralization hosted in quartz-feldspar porphyry dikes, biotite-rich feldspar porphyry dikes, and along favorable stratigraphic horizons at the Hamburg Formation-Dunderberg Shale contact. In the RBM deposit, gold is hosted in Jurassic intrusions, breccias, and the Chainman Shale.

IV. Geology of the RBM Deposit

Methodology

Accessible exposures in the RBM deposit were mapped between June and August 2007 at a scale of 1:600. Mapping was supplemented by the logging of 7 core holes from in and around the RBM pit. A color-coded mapping and logging scheme similar to that used by the Anaconda Company in the 1960s was employed, which includes graphical and numerical data on rock type, structure, vein types, relative age of intrusions and vein types, mineral associations and approximate volume percent of the minerals and veins (cf. Einaudi, 1997). Field observations were documented and supplemented by transmitted, reflected, and scanning electron microscopy (SEM) at the University of Nevada, Reno on 85 polished thin sections. Four samples were also analyzed using an electron probe at the University of Nevada, Las Vegas to identify the presence and variation of 17 major and trace elements in sulfide phases (Appendix 1). An analytical spectral device (ASD) was used to collect spectral data from 222 samples from logged core holes to better define the mineralogy and extent of clay-bearing alteration. John Muntean interpreted the spectra. Representative samples collected from logged core holes were etched with 50% HF and stained with sodium cobaltinitrite to test for the presence of potassium feldspar. Potassic alteration, determined by staining, was then verified with energy dispersive spectroscopy (EDS) using the SEM. A survey was conducted using a gamma ray spectrometer on one bench of the RBM pit, with 120-second measurements taken to define variation in potassium concentration along and away from faults and intrusive contacts.

Mapping was compiled in ArcGIS to create a map of lithologies, alteration, mineralogy, and gold zones in the RBM pit (Plate 1). A cross-section was constructed from four of the logged core holes, supplemented by core and chip holes logged by Bald Mountain mine geologists (Fig. 4). Contours of gold grade in the RBM pit were interpreted from cyanide leachable assay data on blasthole cuttings from the benches that were mapped. For the cross section, gold contours were interpreted from fire assays of drill hole intervals that ranged from 2 to 10 feet in length.

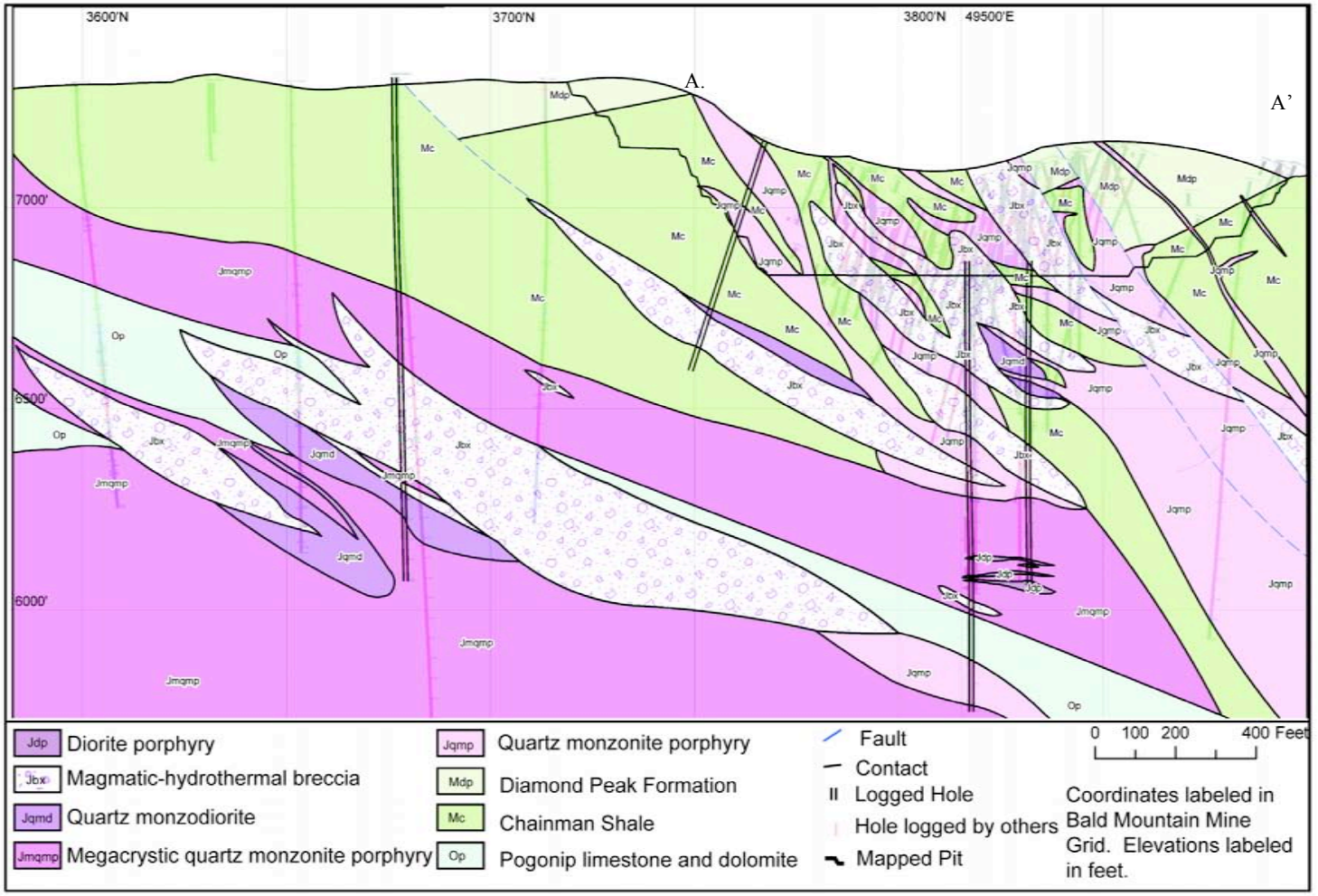

Figure 4A. Northwest cross-section looking southwest at the RBM pit and proximal drilling. See Plate 1 for location. Lithologies identified based on pit mapping, core logging in this study, and inferred from descriptions in logs by other geologists for holes not logged in this study. Cross-section extends above the mapped pit based on pre-mining drilling.

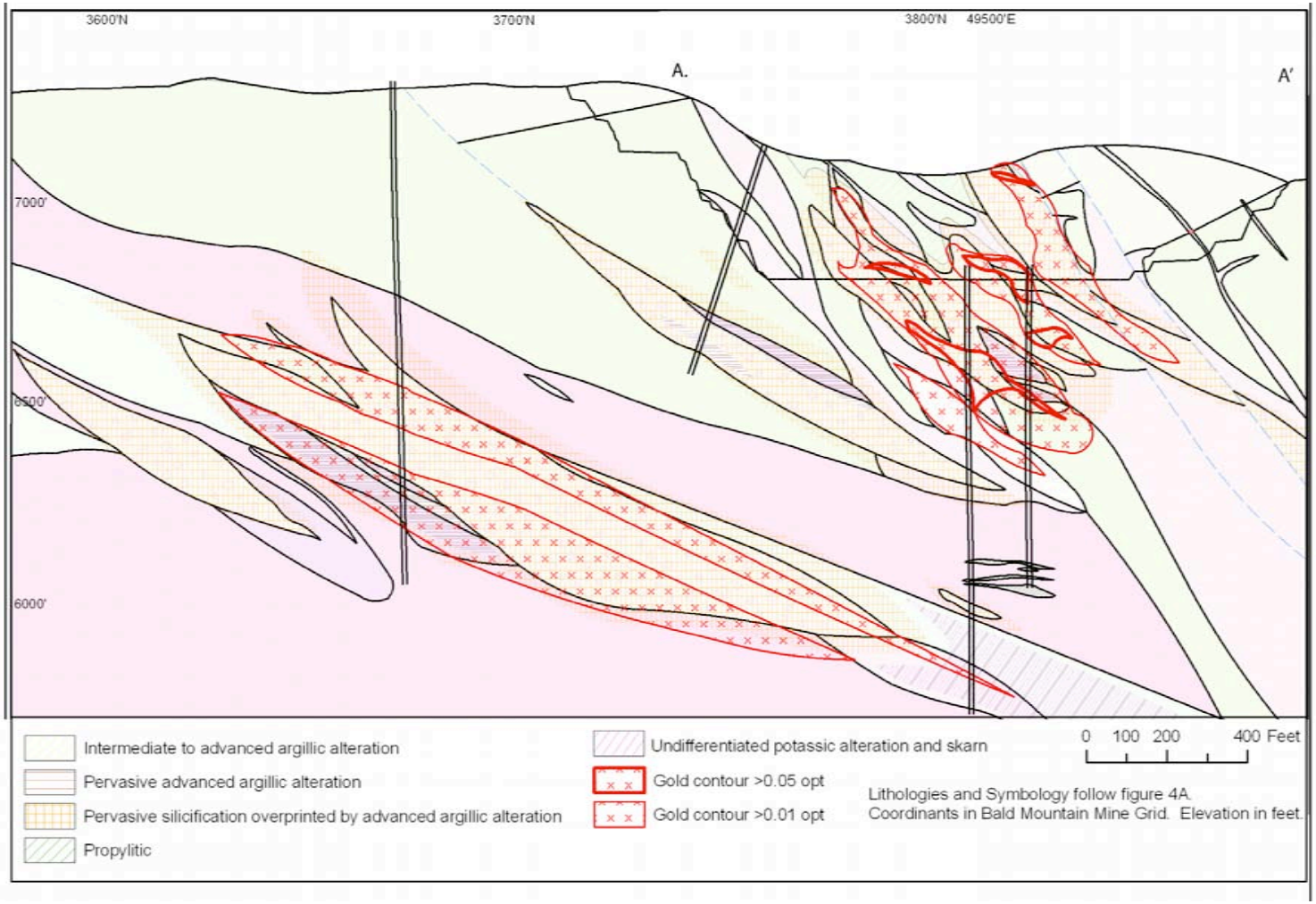

Figure 4B. Northwest-southeast cross-section of the RBM deposit looking southwest showing alteration and gold contours. Alteration types do not follow Plate 1 because advanced argillic alteration overprints silicification throughout breccia zones and differentiating silicified zones from silicified and advanced argillic-altered zones consistently is impossible.

Rock Descriptions

The RBM deposit is hosted mainly by a series of Jurassic intrusions and magmatic-hydrothermal breccias that were emplaced into Paleozoic sedimentary rocks. The volumetrically most abundant unit in the map area is the Chainman Shale, which is overlain on the northeastern and southeastern sides of the RBM open pit by the Diamond Peak Formation. In the mapped area, the Chainman Shale is a pale white to tan massive siltstone, which is intensely leached, variably silicified, and metamorphosed to albite-epidote hornfels. Bedding, which is commonly masked by alteration and metamorphism, strikes northeast and dips 20-30º to the southeast. The Diamond Peak Formation conformably overlies the Chainman Shale, and crops out above the 7050 foot bench in the RBM pit. The contact between the Chainman Shale and the Diamond Peak Formation is gradational, and was mapped by the first occurrence of coarse-grained sandstone lenses with chert clasts interbedded with siltstone (Fig. 5). Sandstone lenses range from cloudy white quartzite to poorly-sorted, medium-grained heterolithic sandstone containing conspicuous chert fragments. Drilling in and around the RBM pit has identified a carbonate unit underlying the Chainman Shale. The unit is made up of massive white marble and white to light grey, thin to medium-bedded dolomite with interbedded silt lenses, and local cm-scale recrystallized grey chert lenses. Recent drilling south of the RBM pit has identified a white quartzite unit, interpreted to be Eureka Quartzite, which overlies the carbonate unit, suggesting the carbonate unit is in the Ordovician Pogonip Group. The contact between the Ordovician units and the overlying Mississippian units is defined by drilling to be a low-angle to flat fault in the hangingwall of the Ruby fault, across which >2500 feet of strata are missing.

Figure 5. Mississippian Diamond Peak identified here by alternating siltstone and medium-grained sandstone lenses.

The sedimentary sequence is intruded by dikes, sills, and a plug of quartz monzonite porphyry, dikes and a stock of megacrystic quartz monzonite porphyry, dikes and sills of quartz monzodiorite, and dikes of diorite porphyry (Table 3). Intense alteration, particularly advanced argillic alteration, masks the primary mineralogy of many of these rock types. Nevertheless lithologies can commonly be differentiated based on the size and abundance of quartz phenocrysts and feldspar phenocryst sites. Trace-element geochemistry of immobile elements, particularly Cr, Co, and Ni, were also used to differentiate lithologies.

Lithology	Code	Description	Geometry	Names assigned in previous studies
Quartz monzonite porphyry	Jqmp	5-15% 0.2-4 mm resorbed quartz, 10-30% 0.5-3 mm feldspar*, 1-5% ~0.5 mm biotite, and 0.5-3% hornblende** in a fine-grained groundmass of 0.01-0.1 mm quartz and feldspar*.	Dikes, sills, and a plug	Quartz-feldspar porphyry (Nutt and Hofstra, 2007; Hitchborn et al., 1996; Wright, 2006), rhyolite porphyry (Thompson, 2004)
Megacrystic quartz monzonite porphyry	Jmqmp	7-15% 0.2-10 mm resorbed quartz, 25-35% 1-5 mm plagioclase, trace-5% 5-20 mm orthoclase, and 1-5% 0.5 mm biotite in an aplitic groundmass of 0.2 mm quartz and alkali feldspar.	Large plug (stock?) below RBM pit	Not differentiated from quartz-feldspar porphyry in previous studies
Quartz monzodiorite	Jqmd	Equigranular rock composed of ~0.2 mm interlocking quartz, feldspar, and biotite. Original mineralogy unknown due to pervasive argillization.	Dikes and sills, commonly with brecciated margins	Quartz feldspar mafic porphyry (Wright, 2006), possible biotite-rich feldspar porphyry (Hitchborn et al., 1996)
Diorite porphyry	Jdp	Trace-10% 1-2 mm plagioclase, 5-7% 0.5-2 mm hornblende, 3% 0.5 mm biotite, trace-5% 1-5 mm quartz***, and trace 10-20 mm orthoclase*** in a felted groundmass of 0.01-0.1 mm subaligned feldspar, hornblende, and quartz.	Thin (<2 m) dikes	Basaltic andesite (Wright, 2006)
Magmatic-hydrothermal breccia	Jbx	30-60% subrounded to subangular fragments of intruded rock cemented by quartz, kaolinite, and pyrite ± marcasite.	NW striking steeply NE dipping lenses	Hydrothermal breccia (Thompson, 2004)
Mafic dikes	Jl	Quartz-deficient rock (<10% quartz). Protolith unknown.	Thin dikes	May be mafic dikes (Hitchborn et al., 1996), ultramafic dikes/lamprophyre (Nutt et al., 2000), and/or lamprophyre (Wright, 2006; Nutt and Hofstra, 2007)

* Plagioclase feldspar impossible to differentiate from potassium feldspar due to alteration

** Hornblende only identified in a few samples but is likely more abundant and masked by alteration

*** Likely xenocrysts

Table 3. Table of the mineralogy and geometry of intrusive phases identified in this study. Names for similar rock types used in previous studies elsewhere in the district are linked with the names assigned in this study where possible based on previous rock descriptions.

Quartz monzonite porphyry (Jqmp)

The oldest intrusive phase in the RBM pit is a plug of quartz monzonite porphyry, termed quartz-feldspar porphyry (QFP) by mine geologists. The primary mineralogy consists of 5-15% 0.2-4 mm partially resorbed quartz phenocrysts, 10-30% 0.5-3 mm feldspar phenocrysts, and 1-5% ~0.5 mm biotite phenocrysts in a groundmass of 0.01-0.1 mm quartz and feldspar (Fig. 6). Sparse (0.5-3%) 0.1-1 mm hornblende phenocrysts have been identified in some of the freshest samples, but are difficult to identify in most samples because of alteration.

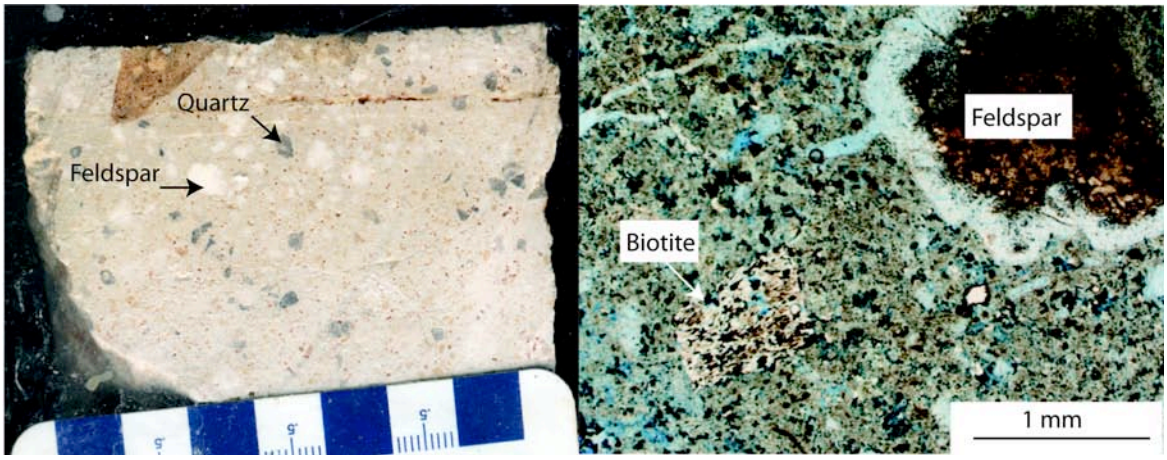

Figure 6. Hand sample and thin section of sericitically altered quartz monzonite porphyry from the RBM pit overprinted by supergene argillic alteration. A. Note rounded and fractured quartz phenocrysts and white feldspar sites which are identifiable in hand sample, distinguishing this from other lithologies. B. Plane polarized light (PPL) photomicrograph of a thin section from the same sample. Note biotite book altered to sericite (white) + kaolinite (brown) + pyrite (opaque and partially oxidized to brown limonite). Also note feldspar phenocryst, which is completely altered to kaolinite. White to light blue color is epoxy showing through as a result of polishing.

The quartz monzonite porphyry plug crops out on the west side of the RBM pit, and is greater than 300 m in diameter. The contact between the plug and sedimentary rocks is faulted throughout much of the deposit. The plug branches out into dikes in the upper benches, indicating the fault contact may be a weak shear zone with minimal offset

that developed along the original intrusive contact due to the rheologic contrast between the intrusion and the country rocks. A series of 1-30 meter-wide, northeast-striking, 20-30° southeast-dipping sills of quartz monzonite porphyry crop out along the northeast highwall. In some places swarms of high-angle meter-wide dikes intrude the Chainman Shale in the lower benches and become sills in the intermediate to upper benches of the RBM pit.

A swarm of 1 to 10 meter-wide north to northwest-striking quartz monzonite porphyry dikes cut the Chainman Shale on the southeast side of the pit. Inspection of intrusive contacts indicate quartz monzonite porphyry dikes grade into heterolithic breccias made up of 1-25 cm subangular fragments of Chainman Shale and quartz monzonite porphyry in an equigranular to weakly porphyritic igneous matrix. These breccias grade outward into monolithic breccia consisting of fragments of intensely hornfelsed Chainman Shale, and further grade outward to a zone of intensely hornfelsed Chainman Shale. This type of brecciated gradational contact is characteristic of intrusion breccias which form along the margins of subvolcanic stocks (Harker, 1908; Sillitoe, 1985). Many quartz monzonite porphyry dikes in the pit have xenoliths of Chainman Shale concentrated along their contacts, but these generally make up <5% of the rock, and do not show the gradational features that are present in the dike swarm in the southeast highwall. The equigranular nature of the matrix in some of the intrusion breccias indicate they may be quartz monzodiorite (described below), but argillic alteration hinders identification of the protolith.

Two thin dikes of quartz monzonite porphyry exposed in the north highwall strike N35°E and N45°E, and dip 52° and 80° northwest, respectively, indicating a northeast-

trending structural control to intrusions in contrast to the dominant northwest-trending control. The contacts between the dikes and the intruded Chainman Shale are sharp. Except for their northeasterly orientation, these dikes are not petrographically distinct from the quartz monzonite porphyry intrusions mapped elsewhere in the RBM pit.

Megacrystic quartz monzonite porphyry (Jmqmp)

A porphyry phase with distinct potassium megacrysts, referred to in this study as megacrystic quartz monzonite porphyry, was intercepted in drill core as a large stock greater than 1 km in diameter that underlies and intrudes quartz monzonite porphyry. The primary phenocrysts consist of 25-35% plagioclase, 1-5 mm in length, 7-15% 0.2-10 mm partially resorbed quartz, 0-5% 5-20 mm potassium feldspar, and 1-5% 0.5 mm biotite in an aplitic groundmass of 0.2 mm quartz and alkali feldspar (Fig. 7).

Figure 7. Freshest sample of megacrystic quartz monzonite porphyry. Pink orthoclase (Kspar) megacryst (~1 cm in diameter) with inclusions of biotite (B) along with milky white plagioclase feldspar (P) phenocrysts and round grey quartz (qtz) phenocrysts. Note crowded nature of porphyry.

The megacryst content is highly variable in drill core; locally they are absent. The coarser nature of the groundmass and more crowded phenocryst content distinguishes megacrystic quartz monzonite porphyry from quartz monzonite porphyry.

Xenoliths of quartz monzonite porphyry in megacrystic quartz monzonite porphyry indicate the megacrystic phase postdates quartz monzonite porphyry dikes and sills (Fig. 8). The Bald Mountain stock, which is located 1.5 km east of RBM in the footwall of the Ruby fault, has similar potassium feldspar megacrysts, and is interpreted to be a cogenetic phase. Aplitic dikes, 5-50 cm thick, intrude the megacrystic phase along irregular, commonly gradational contacts, are interpreted to be cogenetic and were not broken out as a separate, mappable unit.

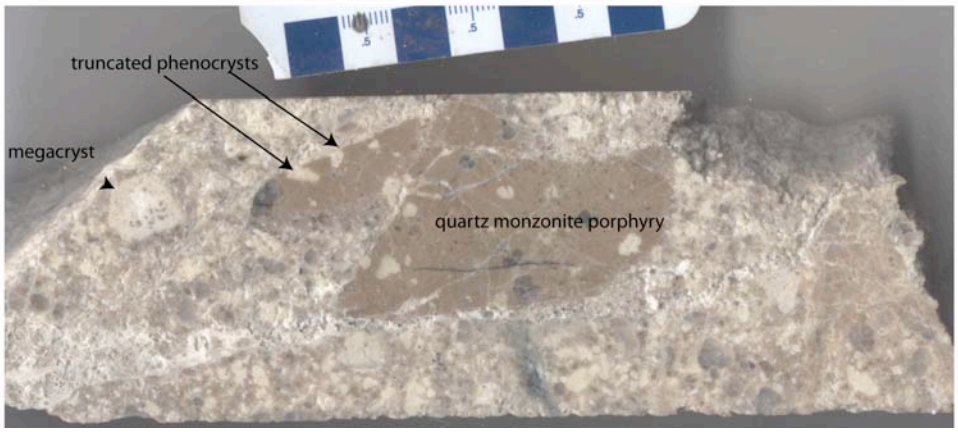

Figure 8. Core sample of quartz monzonite porphyry xenolith within megacrystic quartz monzonite porphyry.

Quartz monzodiorite (Jqmd)

North to northwest-striking, 5-15 meter-thick, quartz monzodiorite dikes, mapped by mine geologists as quartz-feldspar mafic porphyry (qfmp), cut the quartz monzonite porphyry plug in the RBM pit. Up to 30 meter-thick quartz monzodiorite dikes and sills intrude Paleozoic sedimentary rocks, quartz monzonite porphyry, and megacrystic quartz monzonite porphyry in drill core. The primary mineralogy of quartz monzodiorite is everywhere destroyed by argillization and silicification. Up to 30% quartz, which could

be largely hydrothermal in origin, is present as ~0.2 mm anhedral quartz crystals in a matrix of kaolinite. Similar dikes intercepted in drill holes south of the RBM pit contain up to 20% 0.2 mm euhedral biotite. Cubic sites with exsolution lamella of hematite and abundant rutile indicate the presence of primary magnetite-ilmenite intergrowths. Flow foliations are abundant, particularly along the outer edges of quartz monzodiorite dikes in the RBM pit and inferred based on alternating quartz-rich and quartz-deficient rock in partially silicified samples of drill core. At intrusive contacts, monzodiorite dikes locally truncate millimeter-wide barren quartz veins in quartz monzonite porphyry (Fig. 9). The quartz monzodiorite dike that crops out along the southwest highwall is surrounded by about 10 meters of crackle-breccia composed of 1-15 cm angular fragments of quartz monzonite porphyry in a matrix of silica, pyrite, hematite, and goethite (Fig. 10A). In core, many quartz monzodiorite dikes and sills have an outer zone of 1-10 feet of crackle breccia in the wallrock followed by an inner zone of 1 to 5 feet of intrusion breccia with clasts of wallrock in a matrix of quartz monzodiorite that grades into quartz monzodiorite dikes.

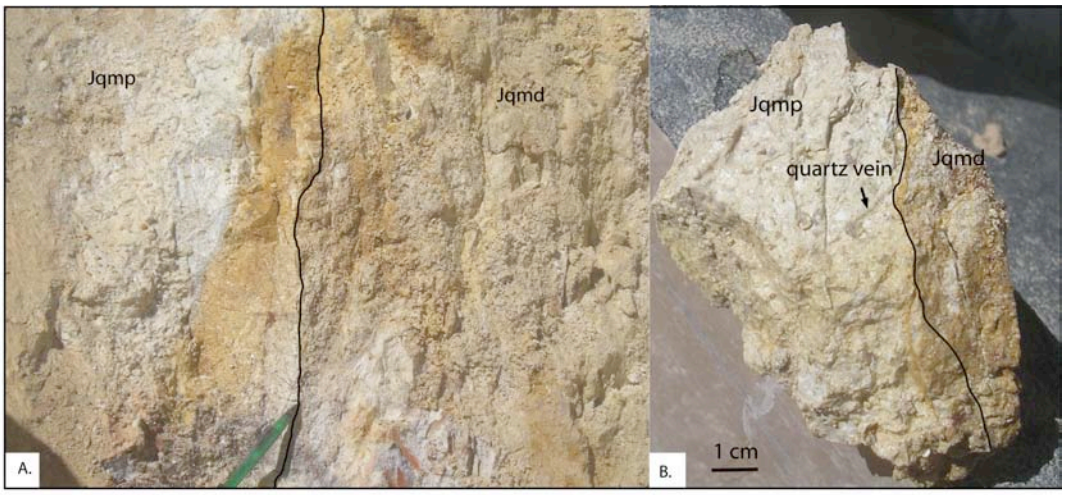

Figure 9.A. Quartz monzodiorite dike (Jqmd) truncating quartz veins in quartz-monzonite porphyry plug (Jqmp) along the southwest highwall of the RBM pit. B. Hand sample taken from location at pencil point in A.

Magmatic-hydrothermal breccia (Jbx)

Northwest-striking, steeply northeast-dipping lenses of magmatic-hydrothermal breccia cut quartz monzonite porphyry, megacrystic quartz monzonite porphyry, and quartz monzodiorite dikes in the RBM pit. Breccias are matrix-supported, composed of 30-60% subangular to subrounded fragments in an altered, finely milled matrix of quartz, kaolinite, and sulfides. Silicified rock and quartz veinlets are the most abundant fragment types in the breccia (Fig. 10B). Silicified rock fragments are cloudy in thin section due to abundant inclusions, including apatite and locally sparse sericite. Although the primary mineralogy is completely masked by alteration in all the samples that were studied, the protolith of the silicified fragments is interpreted to be primarily quartz monzodiorite based on a lack of identifiable relict phenocryst sites that are present in other intrusive phases, and a lack of rounded clastic quartz grains that are present in the Chainman Shale. Clasts of jigsaw and sucrosic quartz are locally present and are texturally similar

to veins identified cutting intrusions and truncated at clast margins. They are interpreted as quartz vein fragments. Local quartz monzonite porphyry and megacrystic quartz monzonite porphyry fragments are identified by the presence of rounded and partially resorbed quartz phenocrysts and relict feldspar phenocryst sites (Fig. 10C). Fragments of Paleozoic sedimentary units, recognized by relict bedding, are present in many of the breccias. Where identifiable, the fragments in breccias appear to be derived from the intruded sedimentary unit, with no indication of significant upward or downward transport. However, vertical transport is difficult to assess due to the intense degree of alteration of fragments, and a lack of clearly identifiable marker horizons in the stratigraphy.

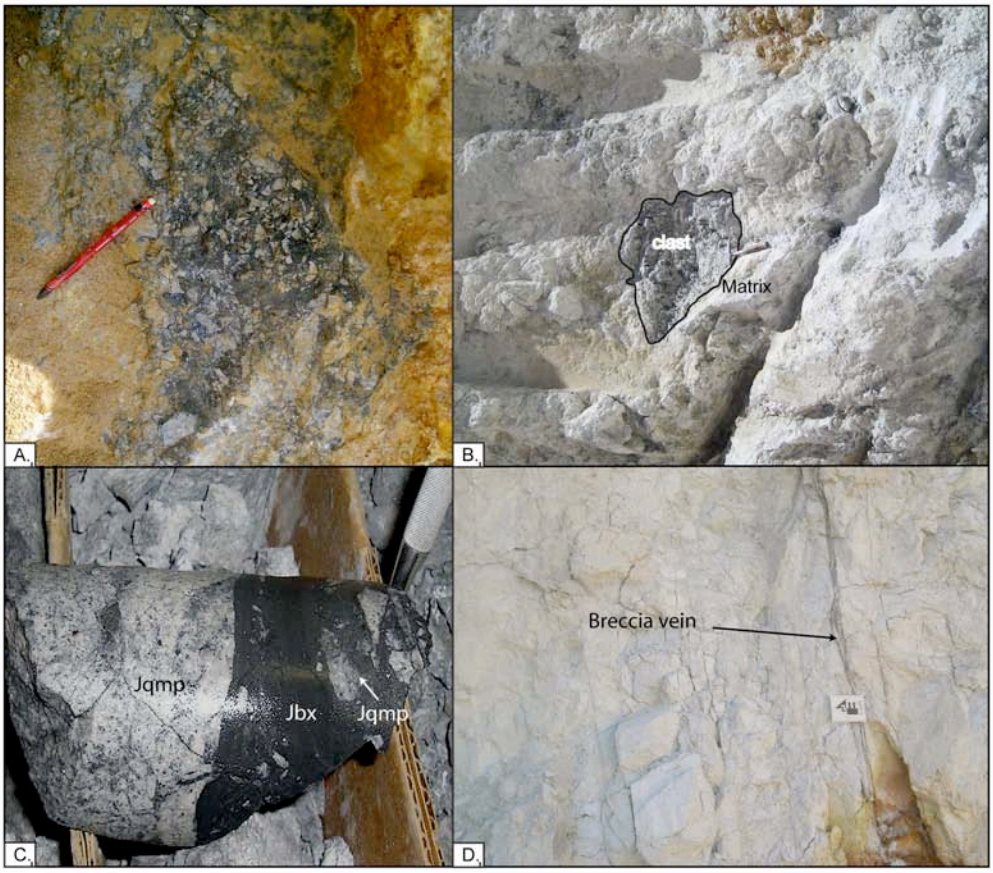

Figure 10. Breccias identified at RBM. A. Monolithic crackle breccia made up of cm-sized subangular fragments of quartz monzonite porphyry in a matrix of quartz and pyrite, partially oxidized to limonite. B. Magmatic-hydrothermal breccia made up of mm to m sized silicified fragments of unknown protolith in a matrix of quartz and kaolinite. One of the clasts is outlined for reference. C. HQ core sample of pyrite-kaolinite cemented breccia (Jbx) cutting quartz monzonite porphyry (Jqmp). Breccia is made up of subangular, subaligned fragments of quartz monzonite porphyry and cuts a quartz monzonite porphyry dike in drill hole RBD0601. D. Pyrite-kaolinite cemented breccia vein cutting quartz monzonite porphyry just north of the main breccia lens in the northeast corner of the RBM pit.

Two major lenses of magmatic-hydrothermal breccia are exposed in the RBM pit. Both strike north 40-60° west and dip 70° to the northeast. Breccia lenses branch outward and up the highwall from a central breccia vein in the core of the pit that was referred to by Hitchborn et al. (1996) as the RBM main vein. A second lens of breccia, referred to by Hitchborn et al. (1996) as the RBM west vein, crops out southwest of the

main breccia zone. Both breccia bodies may be branches of an underlying central breccia pipe located below the pit. In cross-section, a series of breccia veins are present both within the pit and south of the pit (Fig. 4). The breccia veins in the pit are higher-angle and most likely merge northeast of the cross-section shown in figure 4. The breccia veins intercepted at depth south of the pit are lower-angle and more laterally continuous than the steeply dipping main breccia zone in the pit. These low-angle breccia bodies south of the pit are concentrated along the contact between the Chainman Shale and the Lower Paleozoic carbonate units described above. The contact is a low-angle fault that has cut out >2500 feet of section (Ordovician Eureka Quartzite through Devonian-Mississippian Pilot Shale). It is intruded by quartz monzonite porphyry and locally quartz monzodiorite. Another large breccia body has been identified southwest of the RBM pit along the contact between the megacrystic quartz monzonite porphyry stock and the overlying Lower Paleozoic sedimentary units. The large lower breccia body, which is up to 400 feet thick and >1000 feet by >2000 feet in area southwest of the RBM pit, cannot be clearly linked to the breccia bodies that are mineralized in the RBM pit.

The contacts of breccia bodies in the pit and in core are irregular, marked by transitions to monolithic breccias consisting of fragments of the immediate country rocks, and, in places, marked by breccia veins cutting the country rock. Breccia veins are clast-supported, made up of centimeter-sized fragments of country rock in a matrix of kaolinite, quartz, and sulfides. These veins are 0.1 to 0.5 meters thick and concentrated within 5 meters of breccia contacts (Fig. 10D), but locally extend hundreds of meters into the country rock in the south highwall.

Mafic Dikes (Jl)

Thin (<2 m wide) mafic dike-like bodies (Jl), mapped as qfmp by mine geologists, cut breccias and megacrystic quartz monzonite porphyry in core. Mafic dikes are everywhere pervasively sulfidized and argillized, completely destroying the primary mineralogy (Fig. 11). The dikes have only minor quartz, which could be entirely hydrothermal in origin, and are best defined by their high Co and Ni concentrations (Table 4). Mafic dikes are present in thin zones within breccia bodies and appear to be steeply dipping bodies that cut the magmatic-hydrothermal breccias, although crosscutting relationships are unclear due to the intense alteration that results in broken core and poor recovery. These intrusions locally have clasts of magmatic-hydrothermal breccia, indicating they post-date formation of the magmatic-hydrothermal breccias.

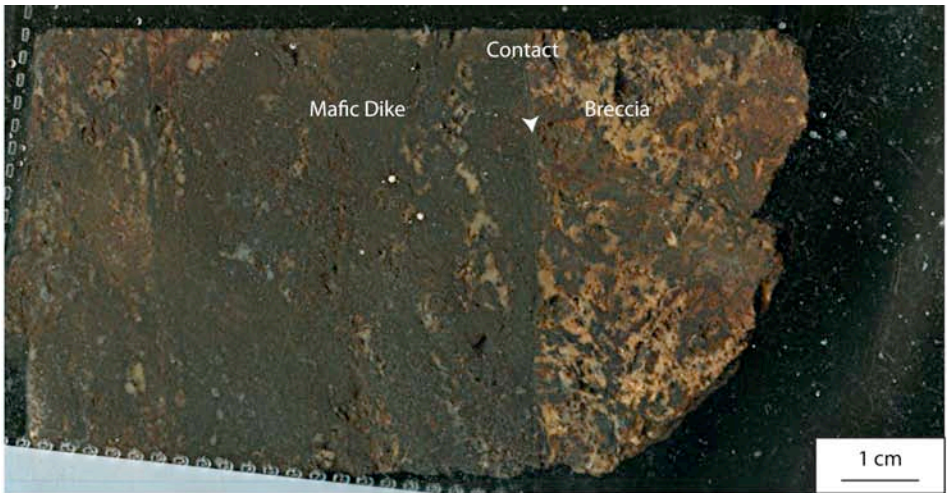

Figure 11. Mafic dike cutting magmatic-hydrothermal breccia in drill core. Mafic dike is completely altered to arsenopyrite + pyrite + kaolinite and breccia is altered to kaolinite + quartz + pyrite + limonite.

Diorite porphyry (Jdp)

A narrow (<1 m) east-west-striking, steeply north-dipping diorite porphyry dike, also mapped as qfmp by mine geologists, cuts the quartz monzonite porphyry plug on the west side of the RBM pit (Fig. 12). Diorite porphyry dikes are present in some core holes, where they cut and contain sparse rounded xenoliths of quartz-veined megacrystic quartz monzonite porphyry, and cut and brecciate quartz monzodiorite dikes.

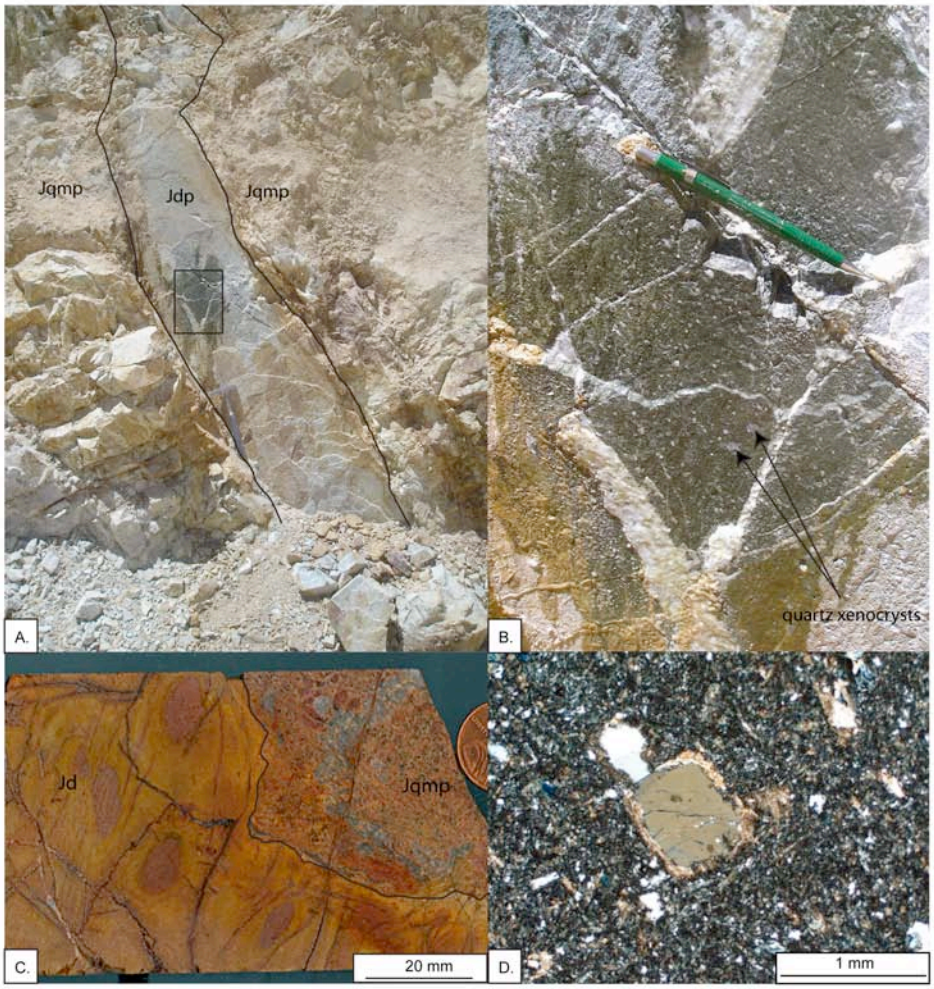

Figure 12. Diorite porphyry (Jdp) (A) dike cutting quartz monzonite porphyry plug (Jqmp) in the west highwall of the RBM pit with (B) close up of diorite porphyry dike (box from 12A) showing sparse quartz xenocrysts. C. Core sample of diorite porphyry (Jdp) with quartz-veined xenolith of quartz monzonite porphyry (Jqmp). D. Photomicrograph of quartz xenocryst (white and light brown) rimmed with calcite (high birefringence) in a felted matrix of hornblende that is altered to chlorite (blue-green to gray) and plagioclase that is altered to calcite (high birefringence)

Diorite porphyry dikes contain trace to 10% 1-2 mm plagioclase, 5-7% 0.5-2 mm hornblende, 3% ~0.5 mm biotite, and trace to 5% 1-5 mm rounded quartz xenocrysts with distinct overgrowths of calcite ± quartz with abundant unknown inclusions in a groundmass of 0.01-0.1 mm subaligned feldspar laths, hornblende needles, and quartz (Fig. 12). Trace amounts of 1-2 cm potassium feldspar megacrysts are present in some but not all mafic dikes. In hand sample, the low abundance of quartz xenocrysts and felted texture of the groundmass make this lithology distinct. Diorite porphyry dikes are similar to basaltic andesite dikes as defined by Barrick geologists (Wright, 2006). Although cross-cutting relationships have not been recognized in the RBM pit, the weak propylitic alteration of diorite porphyry dikes as opposed to all other phases indicates diorite porphyry is the latest phase of intrusion. This is supported by recent drilling southwest of the RBM deposit where weakly altered barren diorite porphyry cross-cuts strongly altered and mineralized quartz monzodiorite and magmatic-hydrothermal breccias.

Trace-element Geochemistry

Multi-element analyses of 257 assay intervals in core holes RBD0601, RBD0603, RBD1001, and RBD1002, drilled in and around the RBM pit, were combined with 50 multi-element assays collected from the RBM pit and keyed to logs and mapping. These assays were used to identify potentially primary geochemical signatures that could then distinguish between highly altered intrusive phases (Table 4). Igneous rocks are commonly characterized based on their silica, aluminum, and alkali concentrations (cf. Blatt and Tracy, 1995). Both hypogene and supergene alteration has added and removed

many elements to such a degree that they cannot be used to differentiate igneous phases. Cr, Co, and Ni, are relatively immobile during alteration, and were chosen as mafic indicator elements to define the geochemical fingerprint of the protolith lithologies.

Lithology	Geochemistry (Median Concentration) Co (ppm)	Cr (ppm)	Ni (ppm)	Number of Analyses
Lower Paleozoic Carbonate (Op)	6.95	14.5	9.3	6
Mississippian Chainman Shale (Mc)	10	113	85	42
Mississippian Diamond Peak Formation (Mdp)	No analyses available			0
Quartz monzonite porphyry (Jqmp)	5	18	15	57
Megacrystic quartz monzonite porphyry (Jmqmp)	5	17	11	89
Quartz monzodiorite (Jqmd)	17	22	39	46
Magmatic-hydrothermal Breccias (Jbx)	17	29	49	54
Mafic Dikes (Jl)	388	20	1150	12
Diorite porphyry (Jdp)	17	306	62	1

Table 1. Geochemistry of distinct lithologies based on multi-element assays compiled for logged core holes from in and around the RBM pit and multi-element assays for grab samples collected during mapping.

Although standard published Co, Cr, and Ni values for the intruded Paleozoic units were not found in a literature review, the Co, Cr, and Ni concentrations appear consistent with typical ranges for similar sedimentary rock types. The Lower Paleozoic carbonate unit has the lowest concentrations of Co, Cr, and Ni. No Co, Cr, or Ni would be present in clean limestones, and the low trace-element concentrations likely come from silty lenses interbedded with limestone. The Chainman Shale has high Cr and Ni concentrations, which appear consistent with the black shale that constitutes most of this formation regionally.

The intrusive phases identified in this study have Co, Cr, and Ni concentrations similar to published values for rocks of similar composition. Quartz monzonite porphyry and megacrystic quartz monzonite porphyry have very similar Co, Cr, and Ni concentrations, providing evidence that they are geochemically similar phases, and both

have compositions which are within the range of typical granitic rocks as defined by Govett (1983) and references therein. Quartz monzodiorite has elevated Co, Cr, and Ni concentrations compared to the monzonite porphyries, with Co and Ni concentrations that more closely resemble that of an andesite rather than a granite. This, along with the lack of silica and abundance of biotite in the freshest samples, indicates it is a slightly more mafic phase than the earlier porphyries, leading to its classification as a quartz monzodiorite.

Magmatic-hydrothermal breccias have Co, Cr, and Ni concentrations that most closely resemble the quartz monzodiorite phase. This, along with the spatial correlation between the two phases, and petrographic observations, suggests that the siliceous fragments that comprise the majority of the fragments in the breccia, are derived from the quartz monzodiorite. The breccias are elevated in Cr and Ni relative to quartz monzodiorite, possibly reflecting the heterolithic nature of breccias, and a mixed geochemical signature between quartz monzodiorite and Chainman Shale. Mafic dikes (Jl) are elevated in Ni and Co, but are not elevated in Cr. These may be a version of lamprophyres identified elsewhere in the district (Nutt and Hofstra, 2007), or indicative of differential mobility of Ni and Co versus Cr during hydrothermal alteration. The intense alteration, and rare occurrence of these units, prevents identification of the protolith.

The diorite porphyry dike identified in the RBM pit has a significantly higher Cr concentration than any of the other intrusive phases. Although this is based on only one sample, recent multielement assays from nearby drilling are consistent with diorite porphyry as being a high-Cr rock, with Cr concentrations generally falling within the

range of a basalt (Govett, 1983). The Co and Ni concentrations are lower than the range for a typical basalt, and are closer to an andesite, but still markedly elevated as compared with quartz monzonite porphyry and megacrystic quartz monzonite porphyry, indicating it is a significantly more mafic rock. This is consistent with field observations described above that suggest the diorite porphyry dikes were emplaced after mineralization. Recent drilling south of the RBM pit has identified diorite porphyry dikes which are not mineralized cutting monzodiorite dikes which contain >3.4 ppm Au.

Key Structures

A major northwest-trending fabric is present in the RBM pit based on alignment of quartz monzonite porphyry dikes, quartz monzodiorite dikes, and magmatic-hydrothermal breccia lenses. This fabric is subparallel with the regional Bida trend, which controls intrusions elsewhere in the district. A 0.5 to 5 meter thick clay-rich gouge zone crops out in the northeast corner of the RBM pit, and is defined by mine geologists as the RBM fault (Fig. 13). The fault strikes N40-50°W and is vertical to steeply dipping to the northeast, with the dip ranging up to 15° from bench to bench. Although no clear offset can be identified along this structure; its high angle and irregular dip suggest that it is likely a strike-slip fault. The RBM fault is intruded by a magmatic-hydrothermal breccia lens, suggesting it is pre-Jurassic in age. Gouge zones along the margins of the breccias indicate a small amount of post-intrusion reactivation, although the nature and magnitude of this offset is unclear, and the gouge zone cannot be traced across the floor of the pit and into the northwest highwall.

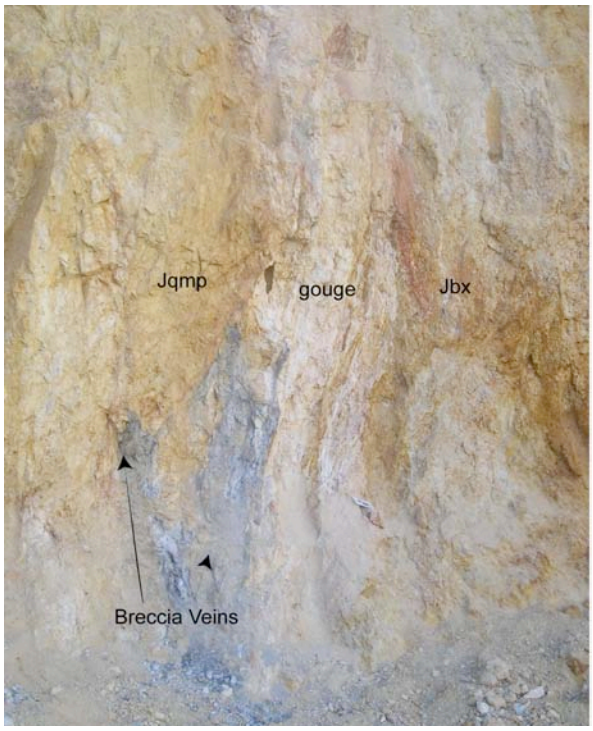

Figure 13. Main RBM Fault on the 6875' bench with a ~1' clay rich gouge zone. Quartz monzonite porphyry is cut by kaolinite-pyrite breccia veins in the hangingwall. The footwall is magmatic-hydrothermal breccia made up of mm- to cm-sized vuggy quartz fragments in a matrix of kaolinite + limonite + hematite.

One north-striking fault is present that appears to cut across the RBM pit. The fault in most places is defined by a strongly sheared zone that strikes north-south and dips ~75º to the east. The fault forms a contact between the quartz monzonite plug to the west in the footwall and the Chainman Shale in the hanging wall across most of the RBM pit. The fault is projected through the bottom of the RBM pit based on possible faulted contacts inferred from logging of blasthole cuttings. Offset along this structure is unclear, but is likely minimal based on the observations of dike-like offshoots of the quartz monzonite porphyry plug that cut the Chainman Shale in the footwall of the fault in the north highwall of the pit.

A series of east-west striking, steeply north-dipping normal faults offset the contact between the Chainman Shale and the Diamond Peak Formation, and truncate quartz monzonite porphyry sills in the northeast highwall of the pit. The faults have thin clay-rich gouge zones (up to 1 meter). Two main faults were identified, with an apparent normal offset of 30-75 meters on each fault, based on the offset of the Chainman-

Diamond Peak contact. The offset is difficult to quantify due to the gradational nature of the contact (Fig. 14). Other northeast striking fractures and faults were identified in detailed pit mapping, but it was not possible to trace them across the highwall, and they are interpreted as minor sympathetic structures. These faults do not appear to cut across the RBM fault, indicating either post-intrusion motion along the RBM fault or termination of northeast structures into the RBM fault. The faults are interpreted to offset the north-south-striking east-dipping fault described above; however, crosscutting relationships are inferred from blasthole cuttings.

Figure 14. North highwall of the RBM pit with approximate contact (black line) between the Chainman Shale (underlying) and the Diamond Peak (overlying) offset along two northeast striking normal faults (blue) that down-drop the contact to the northwest. Note the contact is gradational and the sedimentary units are intruded in places by quartz monzonite porphyry sills that are too small and irregular to point out.

Two north-south-striking faults that dip 70-80° west are present in the southwest wall of the RBM pit. The faults are marked by 0.2-0.5 m wide gouge zones with pods of tectonic breccia, but do not have considerable offset. These faults are sub-parallel and interpreted to be sympathetic to a Tertiary range-front fault, located about 60 meters west of the RBM pit, that drops the bedrock-colluvium contact about 120 meters (Fig. 15).

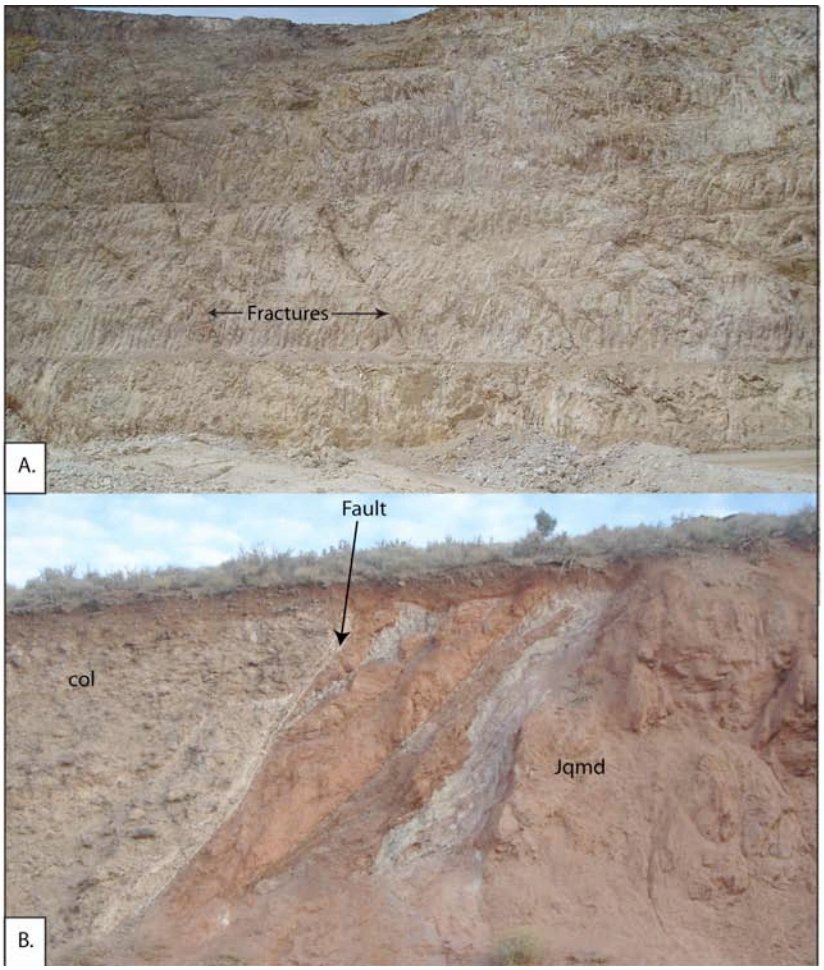

Figure 15.A. Southwest highwall of the RBM pit showing two north-striking faults cutting weakly hornfelsed Chainman Shale. Faults are traceable up the highwall but have minimal offset. They are likely sympathetic structures to the range-front fault located west of the pit. B. Photograph looking northwest at range-front fault exposed on the haul road south of the RBM pit with Tertiary colluvium (col) in the hangingwall and quartz-monzodiorite (Jqmd) in the footwall.

The projection of faults across the floor of the RBM pit is difficult due to the lack of clearly offset units. Offsets have been inferred in the pit floor for units that are identifiably offset in the highwall of the pit (eg. clearly offset quartz monzonite porphyry sills in the north highwall). Cross-cutting relationships between magmatic-hydrothermal breccias and north- and northeast- striking faults are not exposed in the highwalls of the RBM pit. Because gold mineralized zones are steeply dipping, blasthole spacing is wide, and offset along faults is small, offset of gold zones along these faults cannot be defined.

V. Mineralization and Associated Alteration at RBM

Mineralization and associated hydrothermal alteration at RBM can be divided into Early mineralization, Main-stage mineralization, and Late-stage mineralization (Table 5). Early mineralization, defined as mineralization prior to emplacement of magmatic-hydrothermal breccias, includes minor molybdenum and base metal mineralization, and sparse copper and gold mineralization associated with early potassic alteration in some igneous rocks, skarn and hornfels alteration in intruded sedimentary units, and sericitic alteration in many portions of the deposit. Main-stage mineralization, which is spatially and temporally associated with the magmatic-hydrothermal breccias, is characterized by silicification and advanced argillic alteration. Most of the gold as well as a significant amount of copper and arsenic are associated with Main-stage mineralization. Fine-grained arsenian marcasite that cuts breccias and rims fragments characterizes Late-stage mineralization, and is likely associated with further argillic alteration. Pyrite-carbonate veins cut breccias and appear to cut fine-grained marcasite mineralization, although no crosscutting relationships between marcasite-kaolinite veins and pyrite-carbonate veins have been identified. The multiple generations of alteration, including sericitic and advanced argillic alteration, and pervasive clay-rich supergene alteration, has almost completely overprinted early alteration assemblages throughout the deposit, making it very difficult to outline their original distribution.

	Alteration Minerals	Sulfides	Veins	Extent
Early Mineralization				
Potassic	Hornblende phenocrysts replaced by shreddy biotite, biotite books fresh or altered to epidote + actinolite, plagioclase feldspar phenocrysts partially replaced by orthoclase ± chlorite ± actinolite ± epidote, groundmass partially replaced by secondary orthoclase.	Molybdenite + pyrite ± arsenopyrite (V,D)	Abundant mm-cm wide quartz veins, some of which contain molybdenite.	Pervasive in west pit wall, and in deep drilling. Likely widespread throughout deposit but overprinted by later alteration assemblages.
Skarn	Prograde: Andraditic garnets, forsterite, vesuvianite, apatite Retrograde: chlorite + quartz + calcite + pyrite, serpentine + calcite	Molybdenite (D), pyrite ± chalcopyrite (D?)	None identified	Along the margins of dikes intruding carbonate units
Hornfels	Prograde: Diopside + orthoclase + oligoclase + sphene Retrograde: Calcite ± oligoclase	Arsenopyrite + pyrite + arsenian pyrite + chalcopyrite + gersdorfite + tetrahedrite + electrum (V), sphalerite (D)	Irregular orthoclase + oligoclase + quartz veinlets, some with gradational margins into hornfels Oligoclase + calcite veinlets following and replacing prograde assemblage	Along the southeast highwall of the pit and overlying the large megacrystic quartz monzonite porphyry stock
Sericitic	Feldspars are altered to sericite ± carbonate (possible overprint), all biotite books altered to sericite+ pyrite, groundmass flooded by quartz and sericite	Arsenopyrite + pyrite + sphalerite + galena + bladed marcasite (V), chalcopyrite + bladed marcasite(M, D)	Sericite ± sucrosic quartz veins	Most common in deep zones in quartz monzonite porphyry and megacrystic quartz monzonite porphyry, may be more widely distributed but is overprinted by other phases
Main-stage Mineralization	Pervasive alteration to quartz, kaolinite, dickite, rutile (Advanced Argillic)	Arsenopyrite + pyrite ± marcasite, chalcopyrite, native Au (M,D)	None Identified	Pervasive throughout magmatic-hydrothermal breccia and in adjacent wallrocks.
Late-stage Mineralization	Kaolinite in poorly defined veins cutting breccias and in structures (Advanced Argillic)	Arsenian marcasite ± pyrite (V,D)	Irregular marcasite + kaolinite veins	Isolated to structures and isolated zones of breccias.
Carbonate-Pyrite	Possibly related to groundmass of igneous rocks flooded by ankerite, feldspars partially to completely replaced by carbonate.	Euhedral brassy pyrite (V)	Ferroan carbonate veins	Widespread throughout the deposit
Supergene	Dominantly kaolinite, alunite, chalcedonic silica ± nontronite ± illite ± montmorillonite	Chalcocite (V,D)	Limonite and alunite veinlets	Pervasive throughout oxidized portions of the deposit and along faults and fractures in sulfide-bearing rock

Table 5. Table of alteration assemblages and associated veins and sulfide mineralization. Sulfides are further differentiated into occurrences in veins (V) disseminated (D) and massive (M).

Early Mineralization.

Potassic Alteration. Early potassic alteration of quartz monzonite porphyry occurs on the west side of the RBM pit, in megacrystic quartz monzonite porphyry below the center of the pit (as logged at the bottom of core hole RBD0601), and in the bottom of several holes drilled southwest of the RBM pit. In porphyries, the potassic alteration is characterized by partial replacement of the groundmass by micron-sized orthoclase. Plagioclase phenocrysts are partially replaced by orthoclase, and hornblende phenocrysts, where present, are replaced by fine-grained aggregates of shreddy-textured, secondary biotite. Because primary hornblende phenocrysts are very scarce in quartz monzonite porphyry, and secondary orthoclase is very fine grained, potassic alteration cannot be easily mapped in the field.

An Explorium GR-256 gamma ray spectrometer was used to identify the amount of radiation released by potassium, thorium, and uranium in the highwall of the northern portion of the 6875 ft elevation bench (Fig. 16). Readings were used to map the variation in the potassium concentration of rocks exposed, and identify areas with high relative concentrations of potassium that could be the result of potassic alteration. Gamma ray readings were verified by, and augmented with assays of samples collected during pit mapping. The survey revealed the highest potassium concentrations generally occur within a 600-foot north-south zone on the west side of the pit. Samples from this zone were stained with sodium cobaltinitrite (Fig. 17), and analyzed using EDS on an SEM to verify that the high potassium readings using the gamma ray spectrometer correlated with potassic alteration as defined above. In addition, increasing potassium concentrations were detected with the spectrometer in quartz monzonite porphyry as the contact with the

main breccia lens in the eastern highwall of the pit was approached with potassium counts near the contact more than 3 times higher than those 100 feet into the quartz monzonite porphyry. The potassium concentrations decreased abruptly at the quartz monzonite porphyry-breccia contact, and remained low throughout the breccia body. Although staining with sodium cobaltinitrite did not define potassium feldspar in this area of the pit because feldspars were altered to kaolinite, this area was possibly also affected by potassic alteration. Staining of representative samples of drill core and pit exposures revealed zones of relict potassic alteration of the quartz monzonite porphyry in the west highwall of the pit and below the center of the pit. Recognition of relict potassic alteration and the high gamma ray readings along the margins of the breccia lens, indicate that potassic alteration was likely widespread before it was overprinted by subsequent alteration events, namely sericitic alteration and advanced argillic alteration associated with Main-stage mineralization and subsequent supergene oxidation. Other than potassic alteration envelopes on 0.5-2 mm quartz-molybdenite veinlets reported by Nutt and Hofstra (2007) in the Top deposit, widespread potassic alteration has not been previously documented at Bald Mountain.

The potassically altered quartz monzonite porphyry on the west side of the pit is cut by east-west striking, steeply north-dipping sheeted white quartz veins that are about 1-10 cm thick. Selective sampling of these quartz veins yielded an assay of 0.0789 ppm gold, 136 ppm copper, 133 ppm molybdenum, and 124 ppm zinc. In addition, irregular and anastomosing 0.1-1 cm sucrosic quartz veins are ubiquitous in relict potassic alteration zones throughout the pit. Locally within potassically altered quartz monzonite porphyry, pods of actinolite + epidote replace orthoclase and mafic phenocrysts, and

chlorite replaces relict plagioclase phenocrysts (Fig. 17c). Sparse, discontinuous, ~0.2 mm-wide sucrosic quartz-epidote-allanite-pyrite veins with irregular vein margins are also present.

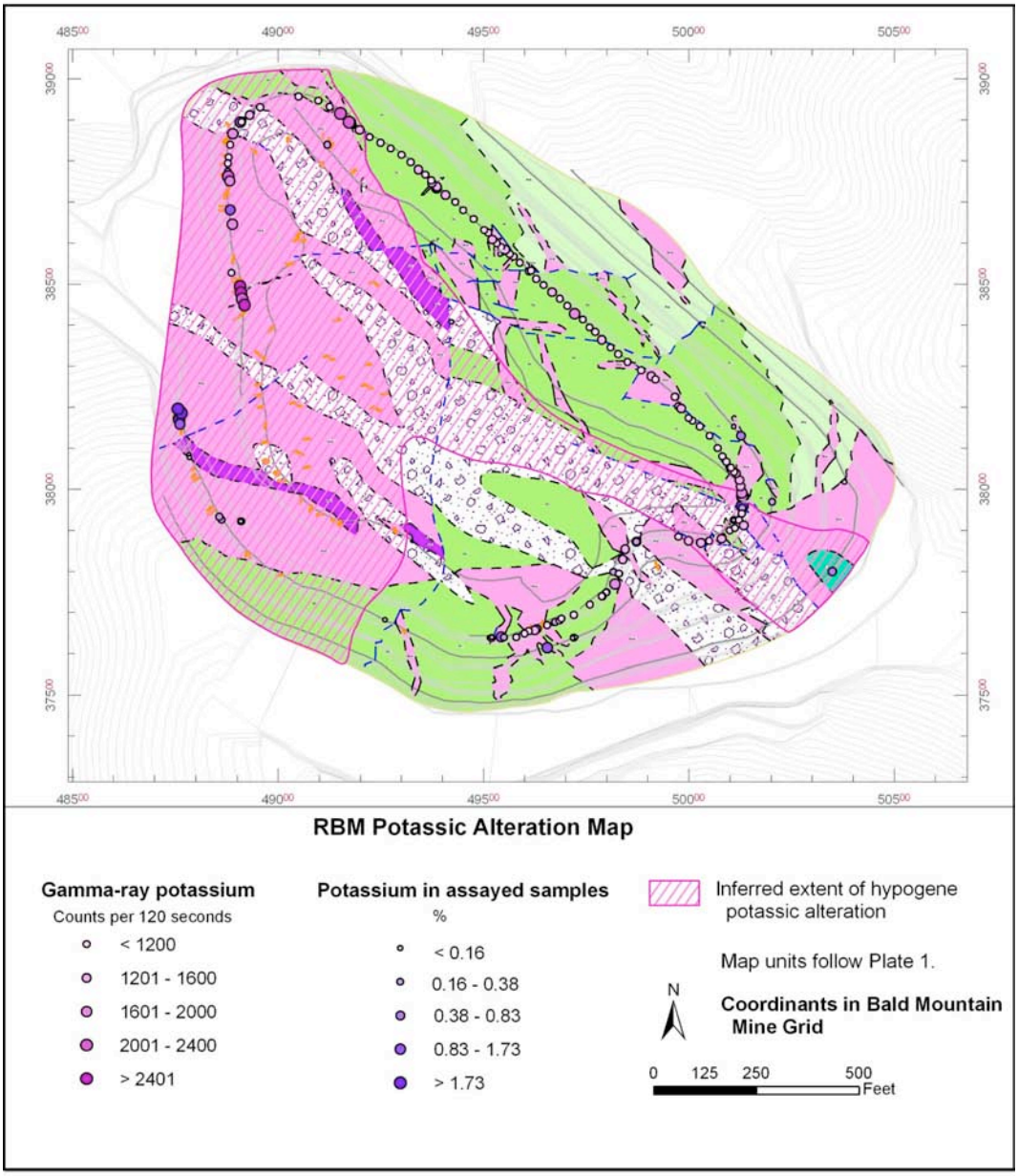

Figure 16. Map of inferred hypogene potassic alteration. The extent of hypogene alteration is based primarily on: 1. a gamma-ray spectrometer survey which reveals high concentrations in the west high wall of the pit, 2. assays on samples collected during pit mapping which show high potassium concentrations in the southwestern corner of the pit, 3. a garnet-bearing skarn pod which is indicative of high temperature alteration and likely associated with hypogene potassic alteration and 4. the extent of quartz veins that are likely associated with potassic alteration (shown on Plate 1).

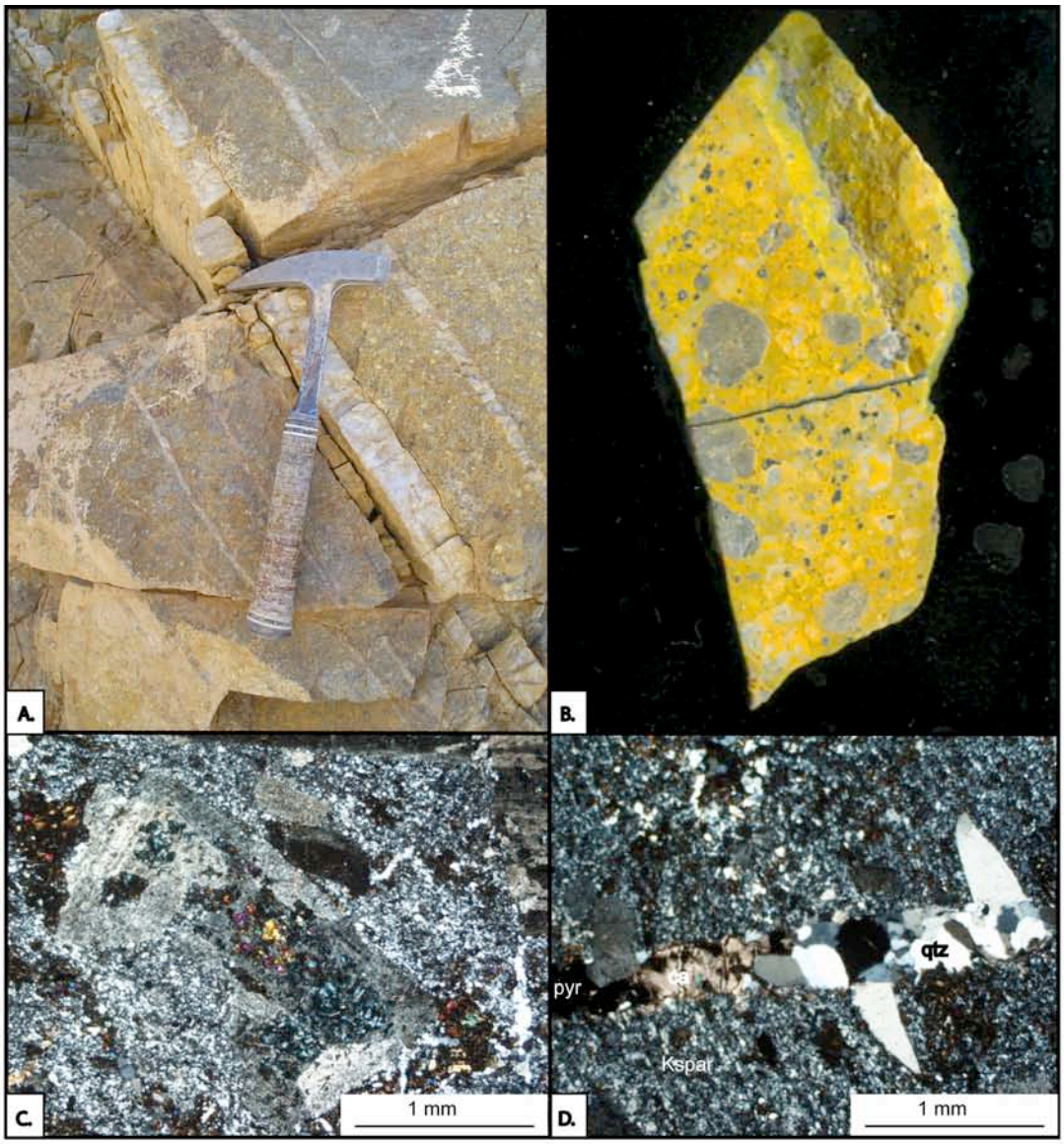

Figure 17.A. Potassically altered quartz monzonite porphyry cut by 5-10 cm east-west striking quartz veins dipping ~60°N. A selective sample on quartz vein assayed 0.0789 ppm Au, 0.87 ppm Ag, 136 ppm Cu, 133 ppm Mo, and 124 ppm Zn. B. Thin-section billet etched with HF and stained with sodium cobaltinitrite resulting in potassium feldspar staining yellow. C. Photomicrograph of plagioclase phenocryst partially replaced by fine-grained potassium feldspar, with the core partially replaced by epidote (high birefringence) and chlorite (blue-green). Supergene argillic alteration has partially altered plagioclase feldspar to clay (cross-polarized light (XPL)). D. Photomicrograph of quartz (qtz)-calcite (ca) -pyrite (pyr) vein cutting potassium feldspar (Kspar) flooded groundmass of quartz monzonite porphyry (XPL).

Skarn/Hornfels. Garnet-bearing calcic skarn, magnesian skarn, and oligoclase-diospide-sphene hornfels are locally present in intruded sedimentary units, and are likely temporally related to potassic alteration in intrusive rocks. Metasomatic garnet skarn crops out as an isolated pod in the northeastern highwall above the 7100 foot level of the pit within a >200 foot wide northwest striking dike of quartz monzonite porphyry. Prograde skarn mineralogy of this pod includes (~0.5 mm) andraditic garnet and apatite. A retrograde mineral assemblage of quartz, chlorite, calcite, and pyrite (mostly oxidized to limonite) occurs interstitial to garnet and apatite (Fig. 18). Supergene chalcocite was locally observed. A grab sample from the garnet skarn pod contained 1,090 ppm molybdenum, 1,960 ppm lead, 288 ppm copper, 228 ppm zinc, 100 ppm bismuth, 56.4 ppm tellurium, 15.3 ppm tin, and 0.055 ppm gold. Although not previously identified at RBM, small bodies of garnet skarn were reported by Hitchborn et al. (1996) along the margins of the Bald Mountain stock, within 1 meter of the intrusive contact. The protolith of the garnet skarn pod in the RBM pit could not be determined with certainty, however, it is likely a block of limestone country rock. Although mostly oxidized, pyrite and trace supergene chalcocite locally occur in the skarn.

Magnesian skarn locally occurs in core holes drilled below and south of the present RBM pit and likely represents dolomitic lithologies in the lower Paleozoic carbonate units. The mineralogy of this zone consists of pods of coarse-grained phlogopite, tremolite, and vesuvianite with lesser forsterite, that is partially replaced and veined by retrograde quartz, chlorite, serpentine and calcite (Fig. 19). Where quartz monzonite porphyry and megacrystic quartz monzonite porphyry dikes cut country rocks

altered to magnesian skarn assemblages, they locally contain epidote + tremolite ± serpentine veins.

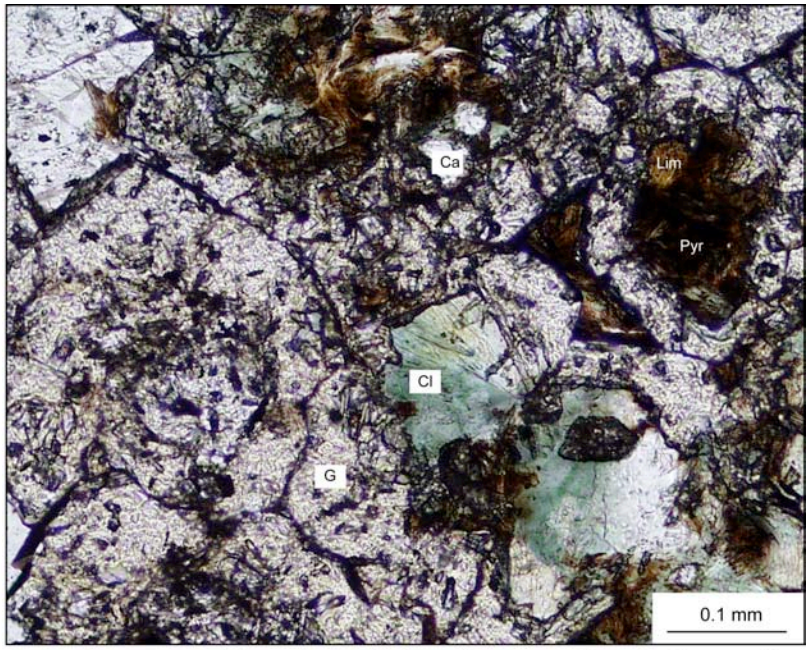

Figure 18. Photomicrograph of garnetite skarn block in east corner of RBM pit with garnets (G) and interstitial chlorite (Cl), calcite (Ca) and pyrite (Pyr) partially oxidized to limonite (Lim) (plane polarized light (PPL)).

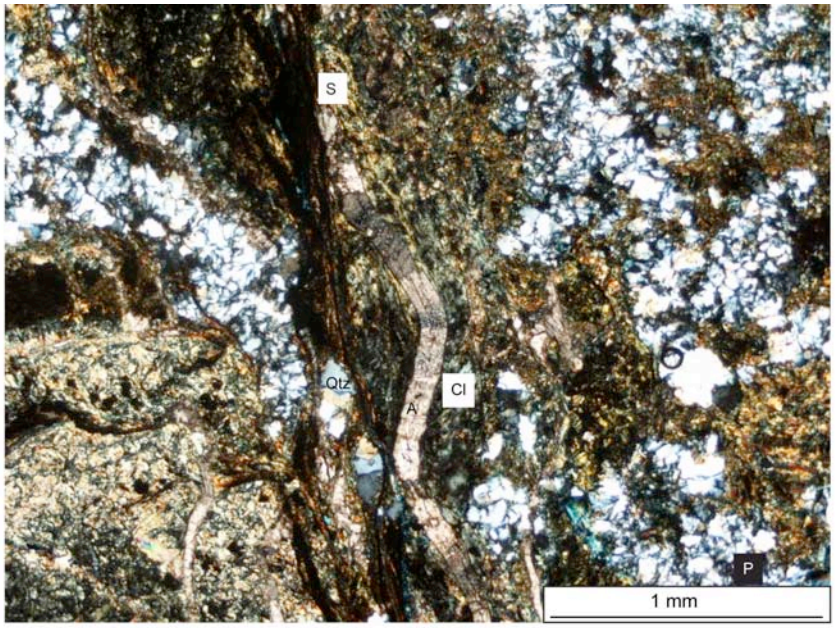

Figure 19. Skarn sample from ~900' below the RBM pit made up of pods of phlogopite (P) + chlorite (Cl), and pods of quartz (Qtz) + serpentine (S) veined by late ankerite (A) (Sample RBD0601-910.5, PPL, mineralogy verified with EDS).

Chainman Shale is moderately to strongly hornfelsed in the southeastern highwall of the RBM pit and in drill core proximal to megacrystic quartz monzonite porphyry. Although most samples of hornfels are overprinted by clay-rich alteration, the best preserved hornfels are composed of 5-50 μm-sized oligoclase + orthoclase + diopside + sphene with trace apatite. This mineral association could be analagous to the albite-epidote hornfels facies and transitional facies described by Hitchborn et al. (1996) and Blake (1964) around the Bald Mountain stock. Hornfels is commonly cut by irregular, branching, 0.1-2 mm wide quartz-oligoclase-orthoclase veins with irregular and commonly gradational vein margins. Orthoclase locally replaces oligoclase. The veins contain sparse 0.05-0.5 mm euhedral to subhedral arsenopyrite, in places overgrown by intergrowths of arsenian pyrite and pyrite. Trace chalcopyrite, tetrahedrite, gersdorffite (NiAsS), and electrum were identified in one vein using the SEM (Fig. 20). Locally, very fine-grained disseminated sphalerite, (2-20 μm) is present in hornfels. Veins and patches of calcite cross-cut and replace quartz-orthoclase-oligoclase veins and are locally associated with sulfides.

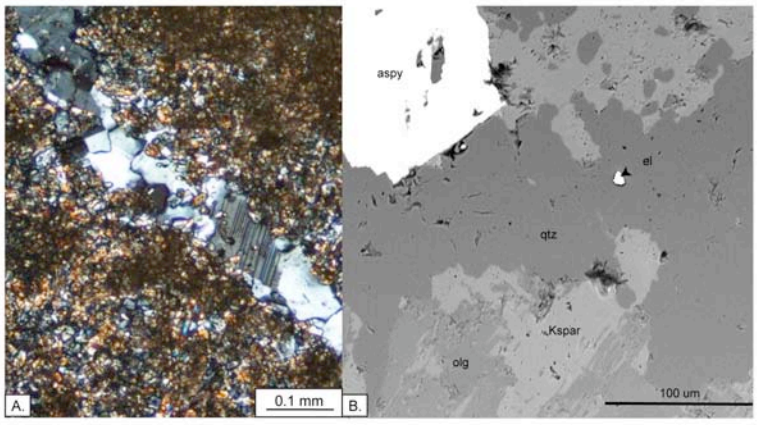

Figure 20.A. Photomicrograph of quartz-orthoclase-oligoclase vein cutting oligoclase-diopside-sphene hornfels (XPL). B. Backscattered electron microscope image of quartz (qtz) - orthoclase (Kspar) - oligoclase (olg) vein with arsenopyrite (aspy) and electrum (el) cutting hornfelsed Chainman Shale below the RBM pit (Sample RBD0601-440).

Sericitic Alteration. Sericitic alteration was likely originally widespread throughout the RBM deposit, but it has been overprinted by advanced argillic alteration in most places, making it very difficult to define its original extent. Weak sericitic alteration, defined by partial replacement of feldspars and biotite by sericite along cleavage planes, is spatially associated with sparse mm-sized barren sucrosic quartz veins and sparse, thin (~0.05 mm wide), anastomosing veins of sericite. This weak alteration is only preserved in a few deep samples of quartz monzonite porphyry and megacrystic quartz monzonite porphyry. Strong sericitic alteration is characterized by complete replacement of feldspars by sericite, replacement of biotite by sericite + pyrite ± leucoxene, and replacement of the groundmass of porphyries by sericite + quartz ± pyrite. Hitchborn et al. (1996) show a wide sericitic alteration zone enveloping the RBM main vein; however, thin sections from well outboard of the sericitic zone depicted by Hitchborn et al. (1996) indicate that sericitic alteration is considerably more widespread, and not directly spatially associated with the main breccia bodies.

Sucrosic quartz veins with sparse 0.2-1 mm molybdenite books and trace <10μm pyrite commonly occur in sericitically altered megacrystic quartz monzonite porphyry (Fig. 21). The veins are 1-100 mm thick, irregular, and anastomosing with sharp vein walls. Nutt and Hofstra (2007) described possibly similar quartz veins that contain chalcopyrite and pyrite with relict sericite along vein margins as the earliest stage of mineralization in RBM. Disseminated euhedral 0.1-0.5 mm pyrite and arsenopyrite, and sparse ~0.5 mm molybdenite books are also associated with this mineralization stage, and are locally spatially associated with the veins. Molybdenite + pyrite ± chalcopyrite mineralization in quartz monzonite porphyry clasts and in quartz veins truncated at clast-

matrix contacts in magmatic-hydrothermal breccias indicate this mineralization occurred before emplacement of breccias and Main-stage mineralization described below (Fig. 22).

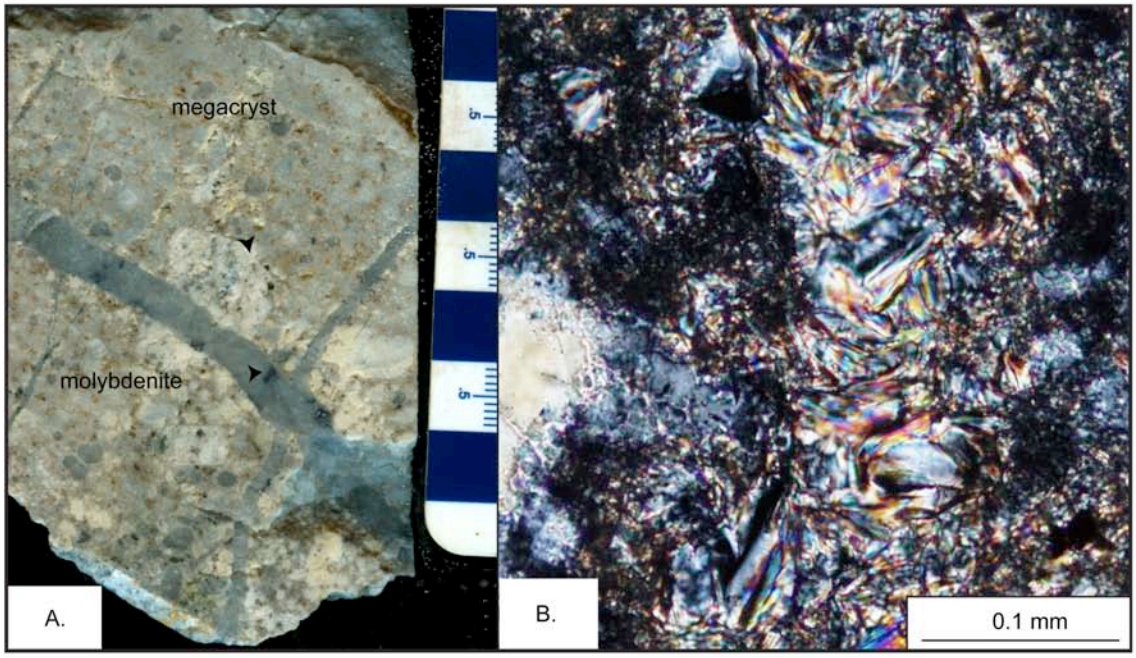

Figure 21.A. Hand sample of sericitically altered megacrystic quartz monzonite porphyry veined by quartz-molybdenite veins. Sericitic alteration (white) replaces all phenocrysts, and is most pervasive along veins (cm-scale). B. Sericite in a vein and pervasively replacing the groundmass of quartz monzonite porphyry (XPL).

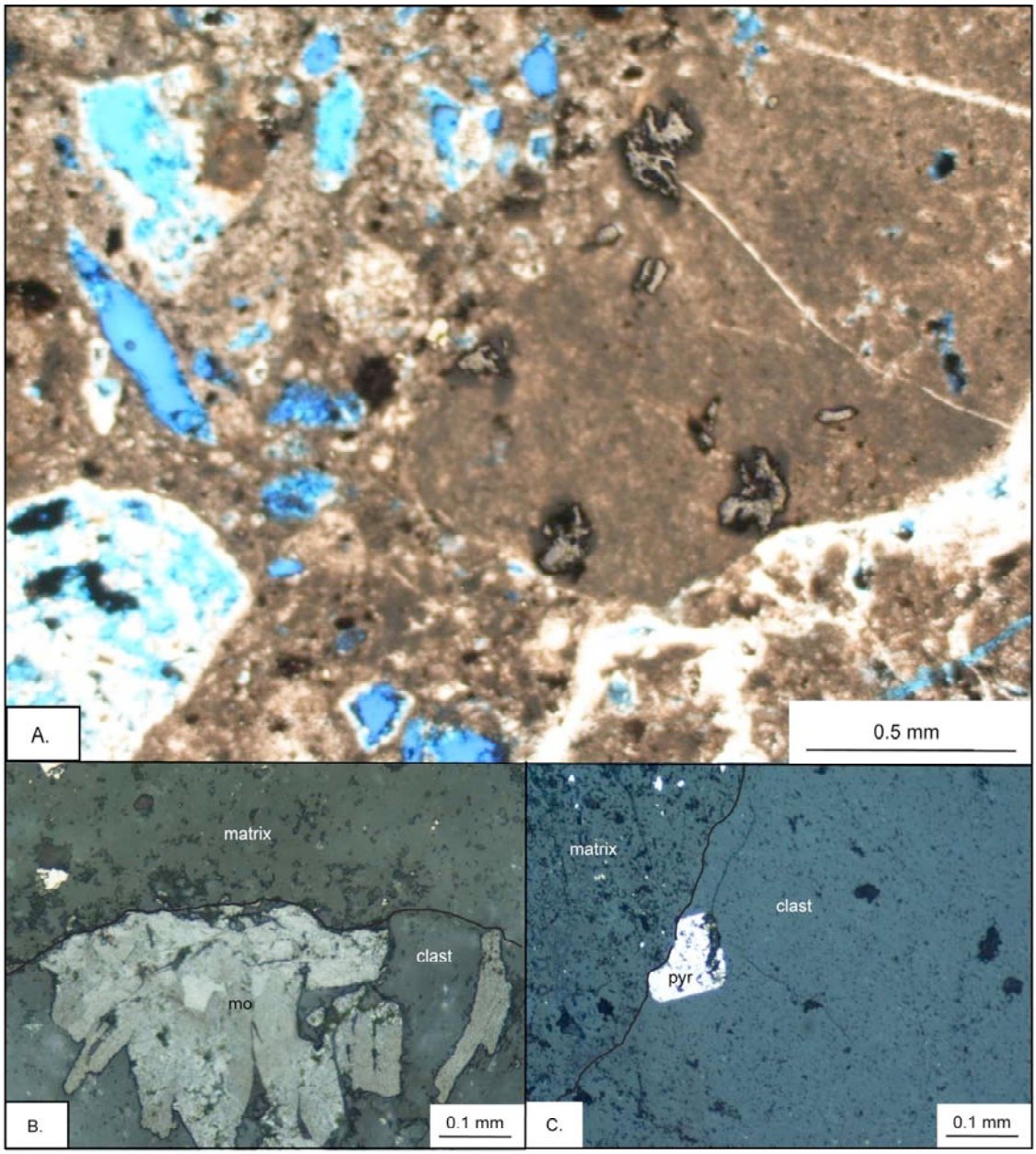

Figure 22.A. Photomicrograph of molybdenite mineralization in argillized fragment within partially oxidized vuggy magmatic-hydrothermal breccia (PPL + reflected light (RL)). B. Molybdenite (mo) books truncated along clast margin (RL). C. Euhedral pyrite (pyr) crystal truncated at clast margin (RL).

South of the RBM deposit, drilling has intercepted a zone of abundant sucrosic quartz ± molybdenite veins in quartz monzonite porphyry, megacrystic quartz monzonite porphyry, and quartz monzodiorite overlying a large megacrystic quartz monzonite

porphyry stock. These quartz veins are similar to the sucrosic quartz veins identified in sericitically ± argillically altered rocks in and around the RBM pit. In one sample from a hole drilled south of the RBM pit, molybdenite mineralization was identified in a ~1 mm vein of quartz + orthoclase cutting weakly argillized quartz monzodiorite which still retained some fresh biotite suggesting molybdenite mineralization is associated with potassic alteration rather than sericitic alteration. In another sample from this zone, a quartz-tremolite vein was observed that cross-cut an irregular molybdenite veinlet in weakly sericitized quartz monzodiorite, further supporting molybdenite mineralization is early, and likely closer in time to potassic alteration rather than sericitic alteration. Although none of the observed quartz-molybdenite veins from the RBM deposit contain orthoclase, are hosted within potassically altered rocks, or exhibit cross-cutting relationships with other vein types, the molybdenite mineralization throughout the RBM area is likely overprinted by sericitic alteration and subsequent alteration types. In addition, the high molybdenite assays in sheeted quartz veins in potassically altered rock, and in the garnet skarn pod are in agreement with molybdenite mineralization as part of an early, high-temperature alteration event.

Where dikes and breccias cut the lower Paleozoic carbonate units in drill core below the pit, 1-10 mm irregular pods of euhedral arsenopyrite, anhedral sphalerite, and euhedral to anhedral brassy pyrite, overprinted by late anhedral pyrite, bladed marcasite, and galena, locally occur in rocks of unknown protolith. These rocks have been replaced by sericite + quartz ± ankerite that is overprinted by kaolinite (Fig. 23). The sulfides are intergrown with sericite, and are, therefore, likely temporally associated with sericitic alteration. Sparse rounded fragments of galena and sphalerite in the matrix of breccias as

well as sericitically altered quartz monzonite fragments in breccias otherwise devoid of sericite suggest sericitic alteration and associated mineralization pre-dated emplacement of magmatic-hydrothermal breccias. Hitchborn et al. (1996) identified a zone of base metal mineralization at the bottom of the RBM pit, and described microbreccias containing angular to subrounded fragments of quartz, galena, and sphalerite with chalcopyrite disease that were cemented by quartz. These observations are consistent with base metal sulfide mineralization predating emplacement of the breccias.

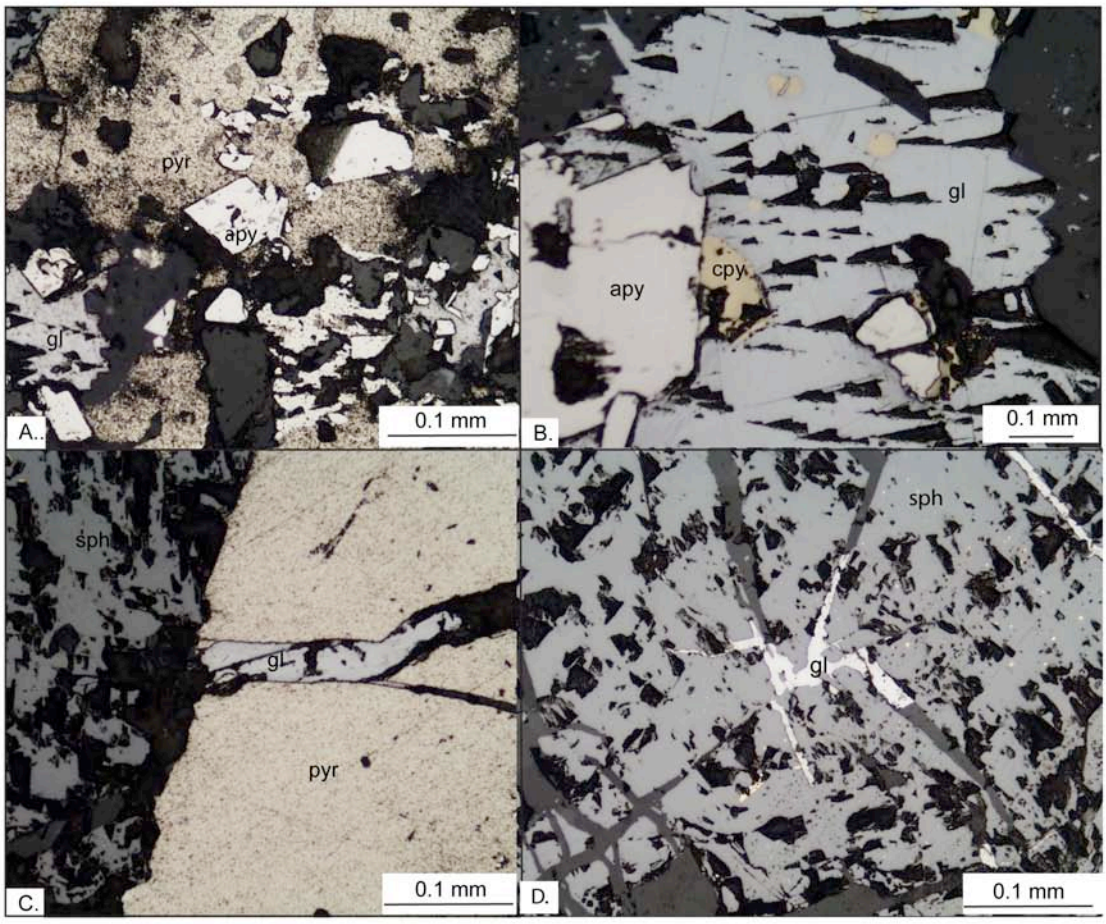

Figure 23. Reflected light photomicrographs of base-metal mineralization related to sericitic alteration defining a paragenesis of early arsenopyrite (apy) mineralization followed by massive anhedral pyrite (pyr) ± chalcopyrite (cpy) ± spalerite (sph) mineralization, which is in turn veined by galena (gl). A. Early arsenopyrite included in pyrite. B. Galena with inclusions of chalcopyrite embays arsenopyrite. C. Massive anhedral pyrite is cut by galena. D. Sphalerite with chalcopyrite disease is cut by galena. Reflected light photomicrographs.

Main-stage Mineralization

Early mineralization is overprinted by intense silicification and subsequent advanced argillic alteration documenting a shift from Early porphyry-style mineralization to Main-stage breccia-hosted mineralization. The final stage of pre-breccia alteration is intense silicification focused along and within quartz monzodiorite dikes and spatially associated with magmatic-hydrothermal breccias. Silicification of the Chainman Shale adjacent to magmatic-hydrothermal breccias is manifested in outcrop as tan brittle fine-grained rock that is leached and partially to completely replaced by fine-grained silica. Diamond Peak sandstones conspicuously crop out near the rim of the RBM pit, and have been mapped as jasperoids by some mine geologists. Silicification of quartz-rich sandstone, however, requires minimal silica metasomatism and may be the result of low-temperature recrystallization unrelated to Main-stage mineralization. Jasperoid and silica boxworks are abundant in the lower Paleozoic carbonate that underlies the Chainman Shale, and are the result of hydrothermal replacement of carbonates by silica, as well as supergene oxidation of sulfides and leaching of carbonates in oxidized portions of the deposit (Fig. 24). In quartz monzodiorite, silicification is characterized by cloudy, inclusion-rich interlocking quartz, which preferentially replaced flowbands, resulting in mm- to cm-sized irregular quartz-rich and quartz-poor bands. Intensely silicified quartz monzodiorite porphyry in some places is made up of >95% quartz making it difficult to differentiate from jasperoid. Trace chromite is present (identified utilizing EDS on the SEM) and verifies that some silica-rich rocks are igneous as opposed to sedimentary in origin, and are most likely quartz monzodiorite. Quartz monzonite porphyry proximal to

quartz monzodiorite dikes in the RBM deposit are brecciated and healed by quartz + pyrite, forming crackle-breccias that further supports a spatial, and likely temporal relationship between silicification and quartz monzodiorite intrusions. Subhedral to anhedral apatite is present in silicified clasts of unknown protolith in breccias. Silicification is associated with abundant branching and anastomosing mm- to cm-wide sucrosic quartz ± pyrite veins and with brassy pyrite disseminated throughout silicified rock (Fig. 25). South of the RBM deposit, drilling has intercepted magmatic-hydrothermal breccias in which both the clasts and the matrix are intensely silicified, as well as magmatic-hydrothermal breccias with intensely silicified clasts in a pervasively argillized matrix. This indicates that there were multiple generations of silicification which both pre-dated and post-dated brecciation. This study has not been successful at differentiating between silicification events other than where they affected breccias.

Figure 24. Hand sample of oxidized and leached gossan with sparse relict pods of pyrite encapsulated in quartz (scale in cm).

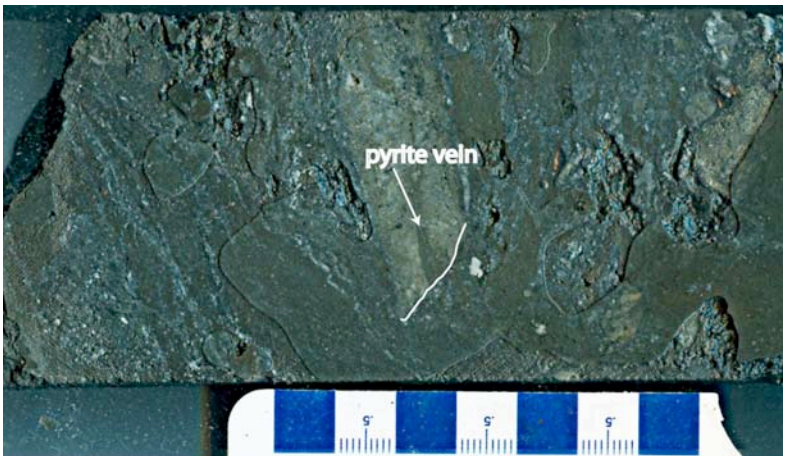

Figure 25. Photograph of fluidized breccia with angular silicified fragment cut by brassy pyrite veins that are locally truncated at clast margins (Sample RBMC3-329, scale in cm).

Advanced argillic alteration is closely associated spatially with magmatic-hydrothermal breccias and is characterized by pervasive replacement of the matrices of breccias by kaolinite + quartz + rutile + sulfides, and local dickite (as determined by reflectance spectroscopy). Advanced argillic alteration is also pervasive in quartz monzodiorite dikes, which are locally replaced by up to 70% kaolinite, as well as quartz and marcasite. Breccia fragments consist of sericitically altered porphyries, silicified quartz monzodiorite, quartz veins, quartz-molybdenite veins, and quartz-pyrite veins. Pyrite and marcasite make up greater than 90% of the sulfides in the breccia and are mostly anhedral and massive. A significant portion of main-stage pyrite is replaced by marcasite. Residual pyrite cores and cubic crystal habits indicate much of the marcasite was originally pyrite. Minor arsenopyrite and Pb-Bi-Te sulfides (as determined by EDS using the SEM) also occur in the breccia matrix, mostly as inclusions in anhedral pyrite (Fig. 26). Arsenopyrite, which contains inclusions of galena and sphalerite, is the predominant sulfide in some high-grade breccia samples, making up ~45% of some intensely mineralized samples. Arsenopyrite appears to be in the matrices of these

samples, but the pervasive nature of sulfide mineralization makes differentiation of clasts and matrix difficult. Local arsenopyrite inclusions in pyrite indicate arsenopyrite crystallized early in breccia matrix mineralization, followed by anhedral brassy pyrite. Late chalcopyrite locally replaces the matrix of breccias, making up >20% of some samples. The chalcopyrite commonly contains inclusions of euhedral pyrite, tennantite, bladed marcasite, and galena.

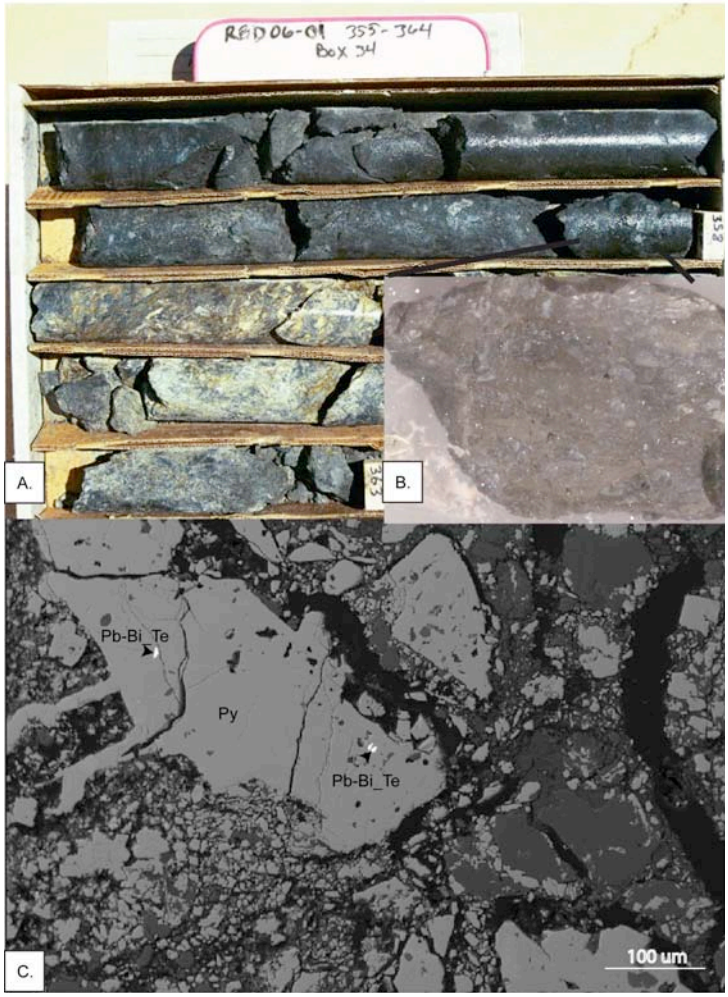

Figure 26. A. Photograph of sulfidized magmatic-hydrothermal breccia in drill core and (B) photograph of hand sample from core interval showing strongly silicified clasts in a matrix of pyrite and kaolinite. C. Backscattered electron image of high-grade magmatic-hydrothermal breccia with anhedral pyrite mineralization in the matrix with inclusions of Pb-Bi-Te sulfide analyzed using WDS.

Late Mineralization

Post-breccia mineralization is characterized by fine-grained marcasite and pyrite. Marcasite crystals are typically <10 μm in size and are disseminated throughout the matrices of breccias, commonly forming large (~50 μm) pods of anhedral crystals, as well as <1-8 μm-wide veinlets and rims on pyrite, chalcopyrite, and breccia fragments (Fig. 27). Sparse, relict <10 μm euhedral arsenian pyrite cubes are present but most have been pseudomorphically replaced by marcasite. Late marcasite is restricted to breccias and breccia veins proximal to breccias. Irregular and discontinuous ~0.01 mm arsenian marcasite ± kaolinite veinlets cut both clasts and the matrices of magmatic-hydrothermal breccias, and replace mm-sized anhedral pyrite grains in the matrices of breccias.

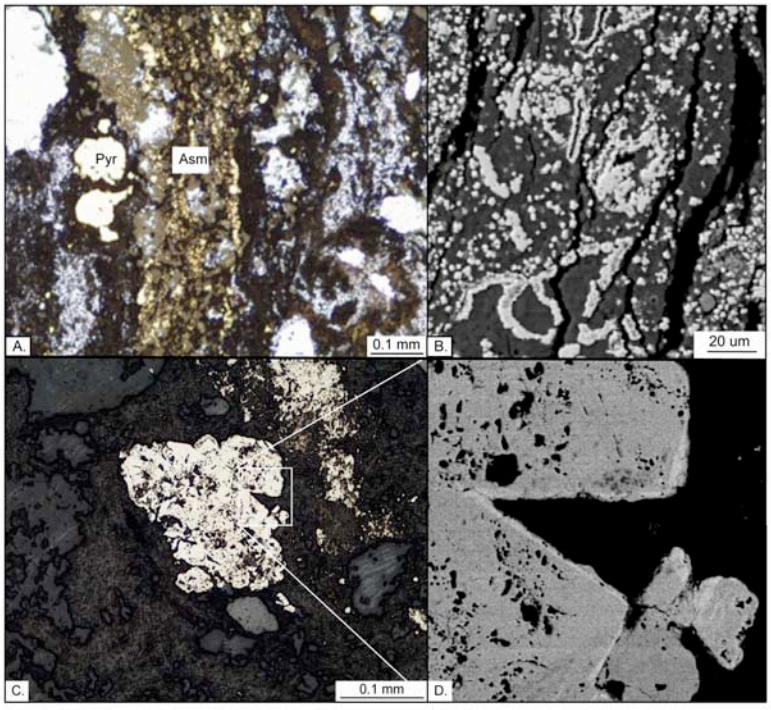

Figure 27.A. Photomicrograph of late As-rich marcasite (Asm) cutting pyrite (Pyr) mineralized argillized breccia (RL + PPL). B. Backscattered electron microscope image of botryoidal late arsenian marcasite and arsenian marcasite rimming kaolinite and quartz. C. Reflected light photomicrograph of pyrite pod rimmed with late arsenian marcasite and (D) close-up backscattered electron image of same pyrite in C showing the contrast between As-rich rim (brighter) and As-poor core.

Nutt and Hofstra (2007) interpreted kaolinite-bearing alteration and marcasite mineralization in the RBM deposit as supergene in origin based on the polytype of kaolinite (1A) and δD and $\delta^{18}O$ isotope values that plot near the supergene kaolinite line. All of their samples from the RBM deposit were within 10 feet of partially oxidized rock. Their samples are not considered representative of the kaolinite-bearing advanced argillic alteration assemblage described here. The advanced argillic alteration in this study is interpreted as hypogene based on intergrowths of pyrite, marcasite, and arsenopyrite with kaolinite for several hundred feet below the zone of oxidation. For example, at least 350 feet of rock showing kaolinite-sulfide intergrowths, with no visual evidence of oxidation, was intercepted in core hole RBD0601, which was drilled from the bottom of the RBM pit (Fig. 28). Hitchborn et al. (1996) identified kaolinite-bearing alteration in RBM, as well as in the Top, RAT, and No. 1 pits as being a late hypogene alteration event superimposed on earlier sericitic alteration. They also identified late pyrite in-filling brecciated base-metal sulfides, a paragenesis consistent with the observations in this study.

Late-stage carbonatization is present as ankerite + pyrite veins cutting other mineral assemblages throughout the deposit. Veins associated with carbonatization are mm to cm-wide sinuous veins of ankerite (EDS analyses indicated the carbonate contained Fe+Mg+Ca, consistent with it being ankerite) with 0.5-2 mm euhedral to subhedral brassy pyrite that cut quartz monzonite porphyries, quartz monzodiorite dikes, breccias, and intruded sedimentary units (Fig. 29). Carbonate alteration in intrusive rocks is characterized by flooding of the groundmass by ankerite. In intrusive rocks, carbonate alteration is overprinted by kaolinite in some places, indicating it may be paragenetically

earlier than late-stage argillic alteration, and not temporally related with ankerite ± pyrite veins which cut, and appear to postdate, kaolinite related to late-stage advanced argillic alteration. Barite is present as 0.2 to 1 mm anhedral crystals filling voids in breccias, and as 0.1 mm irregular and discontinuous veins. The relative timing between barite mineralization and carbonate-pyrite alteration is unknown.

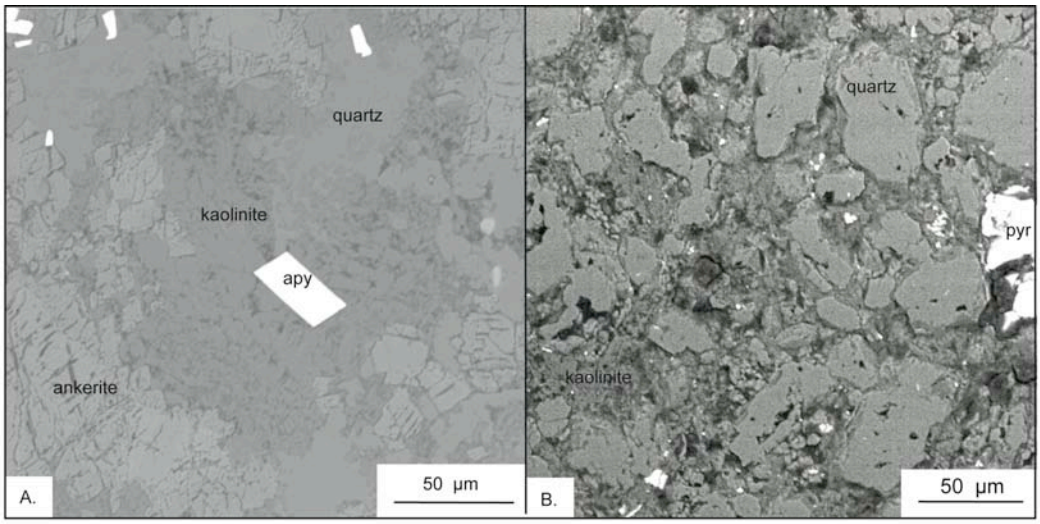

Figure 28. Backscattered electron image of (A) euhedral arsenopyrite crystal surrounded by hypogene kaolinite in a breccia made up of fragments of megacrystic quartz monzonite porphyry replaced by ankerite in a matrix of quartz and kaolinite. B. An intensely milled magmatic-hydrothermal breccia with subrounded to subangular quartz fragments within a matrix of kaolinite and pyrite below the RBM pit 150 feet below the oxide-sulfide boundary.

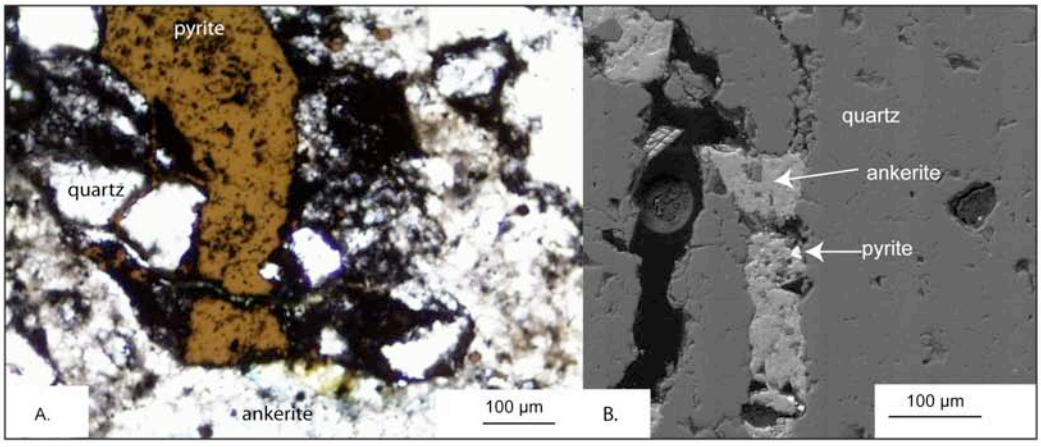

Figure 29. Post-breccia Fe-Mg-Ca-carbonate vein (identified using EDS) cutting a pyrite vein that cuts a brecciated quartz vein in sample RBD0601-360 of a magmatic-hydrothermal breccia. B. Backscattered electron image of late-stage Fe-Mg-Ca carbonate vein with sparse subhedral to euhedral pyrite crystals cutting a silicified fragment in a magmatic-hydrothermal breccia.

Propylitic alteration is confined to diorite porphyry dikes, and is the latest phase of hypogene alteration at RBM. It is characterized by partial to complete replacement of plagioclase feldspar by calcite, and complete replacement of mafic minerals by chlorite. Sparse (~1%) disseminated pyrite may represent sulfidized iron-titanium oxides. A propylitically altered dike in the RBM pit truncates ankerite-pyrite veins in quartz monzonite porphyry in the west highwall of the RBM pit.

Supergene Alteration

Clay-rich alteration is pervasive throughout the oxidized portions of the RBM deposit, and is most likely supergene in origin. Supergene alteration is characterized by the replacement of feldspars by kaolinite, complete to partial replacement of biotite and hornblende by kaolinite + leucoxene ± Fe-oxides, and partial replacement of the groundmass by kaolinite and quartz. Alunite is present in oxidized and sulfide-bearing samples as μm-sized botryoidal crystals in mm-wide veins with sharp margins, and in vugs in gossanous rock along with limonite and opaline silica (Fig. 30). Alunite veins in sulfide material cut pyrite veins and are interpreted as supergene in origin. ASD analyses identified nontronite and montmorillonite along with kaolinite in some oxidized samples. In drill core supergene chalcocite occurs as discontinuous pods, rimming and veining pyrite, arsenopyrite, tennantite, and chalcopyrite (Fig. 31). Chrysocolla ± chalcocite ± malachite are locally disseminated in the sulfide-bearing breccias in the northeastern corner of the pit and along fractures and faults in the bottommost exposures along the southeast highwall of the pit. Goethite and lesser hematite are pervasive in the oxidized

portion of the pit, masking lithologic and alteration contacts. In hematite-rich zones from core, chrysocolla is present, with lesser cuprite and trace native copper.

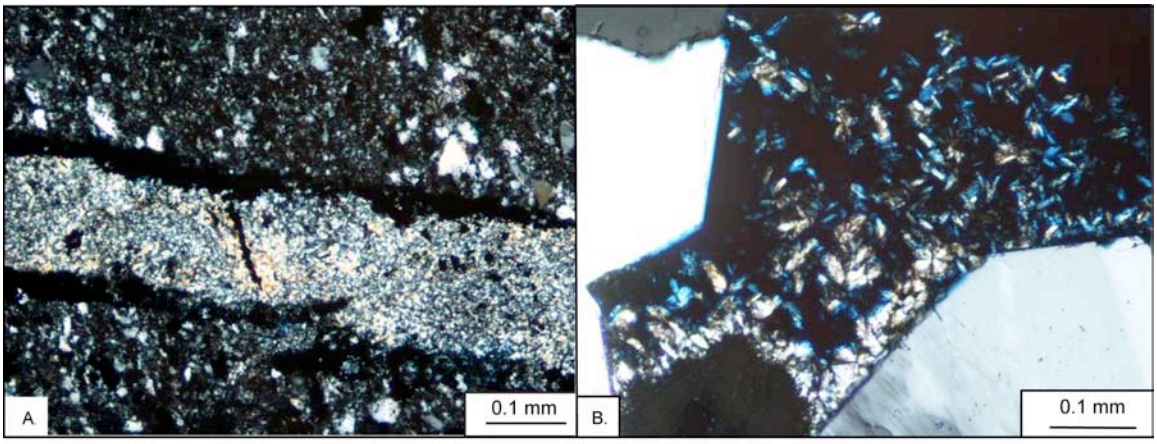

Figure 30. Botryoidal supergene alunite vein (yellow) cutting and running along pyrite vein (black) in sulfidized Mc (XPL). B. Photomicrograph of vugs lined with bladed supergene alunite (XPL)

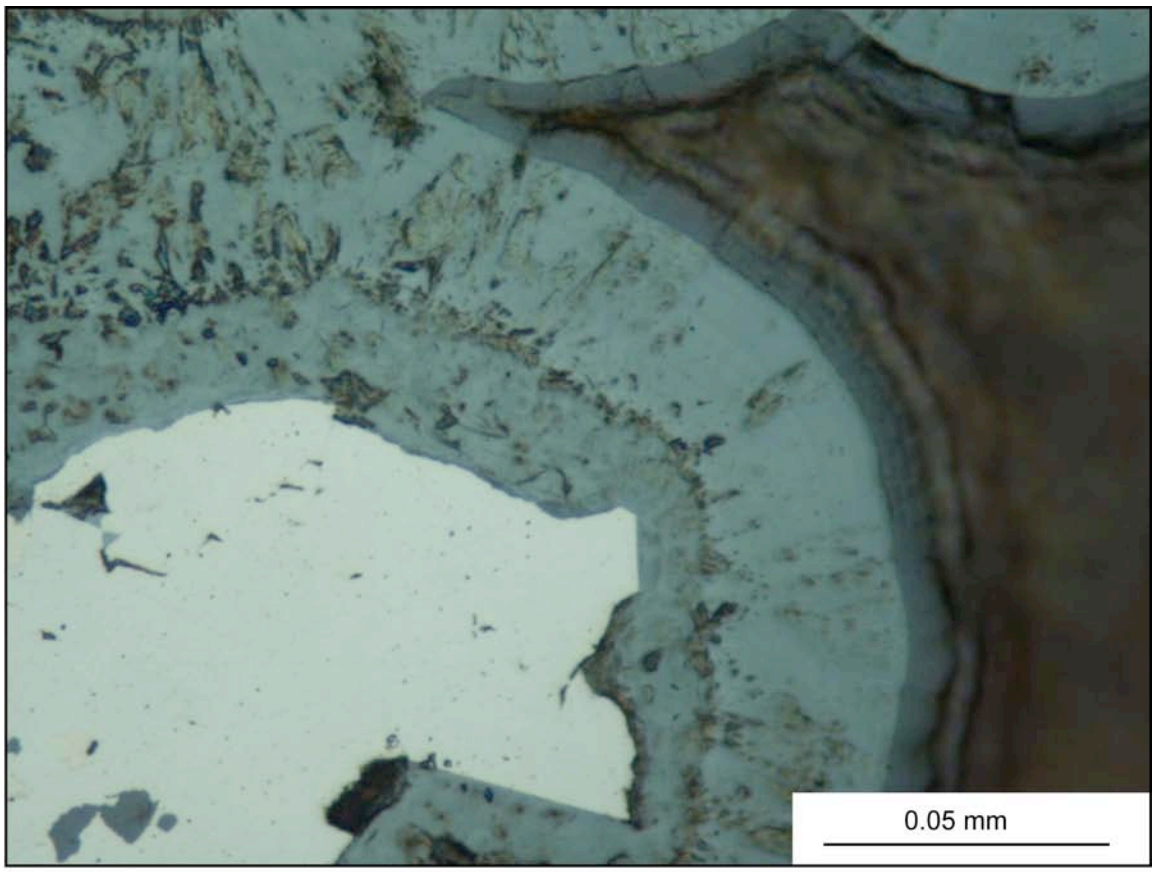

Figure 31. Reflected light photomicrograph of chalcocite (light blue) overgrowths on arsenopyrite (light yellow) in weakly developed enrichment blanket from south of the RBM pit (sample RB06-60-1220).

Gold Occurrences

Gold was deposited during multiple phases of alteration and mineralization in the RBM deposit. Four grains of electrum (5-20μm, identified based on the presence of both gold and silver peak in EDS spectra) have been identified in mineralization and alteration stages that are part of Early mineralization. Two grains were observed in sericitically altered fragments in breccia, one grain was found in a silicified equigranular monzodiorite dike, and a grain was observed in a quartz-oligoclase-orthoclase vein with arsenopyrite cutting hornfels in Chainman Shale (Fig. 32). Ten grains of native gold were identified (2-15 μm in diameter) intergrown with kaolinite and in pyrite in the matrices of sulfide-bearing hydrothermal breccias, characteristic of Main-stage mineralization (Fig. 33).

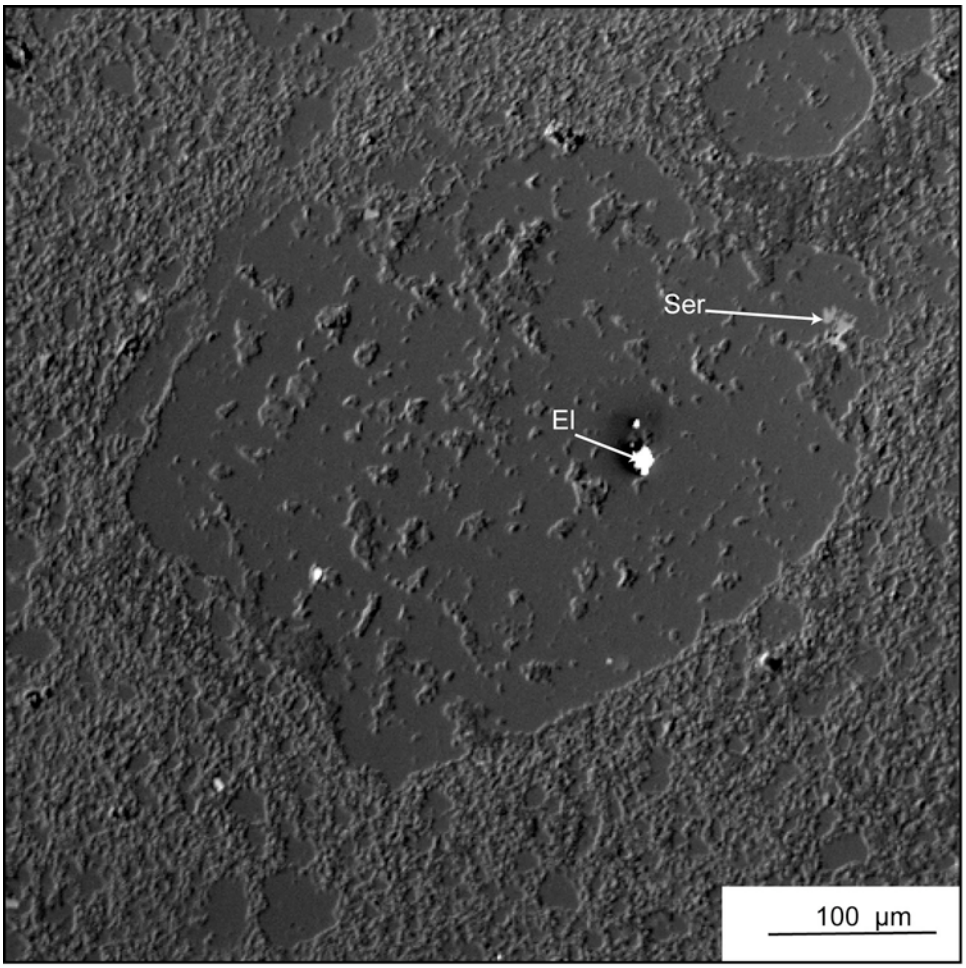

Figure 32. SEM image of a silicified fragment mineralized with electrum (El) identified using EDS which identified both gold and silver peaks. Fragment also has sparse sericite (Ser). The matrix is made up of kaolinite and quartz.

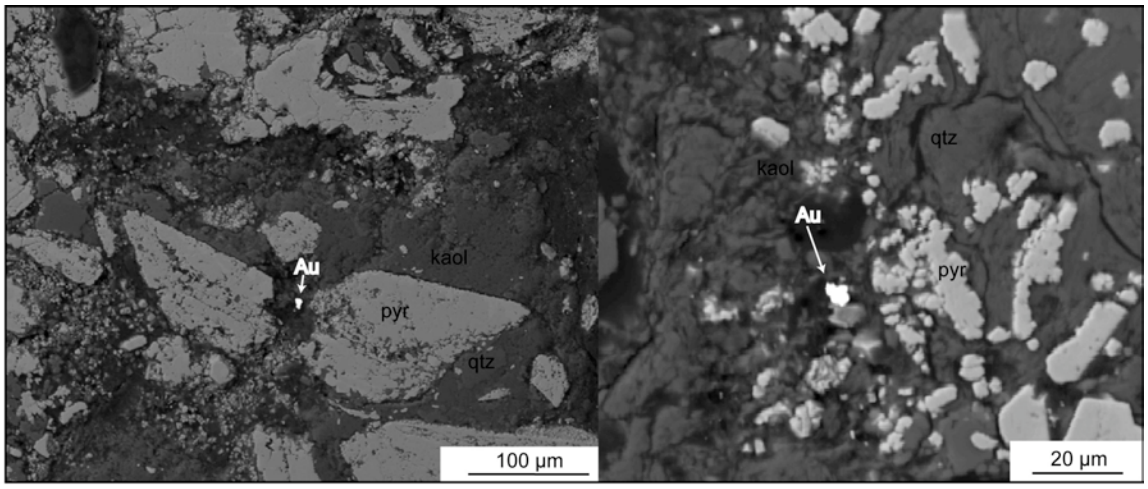

Figure 33. Backscattered electrom images of free gold in quartz-kaolinite-pyrite altered matricies of magmatic-hydrothermal breccia from below the RBM pit. These occurrences are thought to be representative of Main-stage gold mineralization.

***Trace Elements**: Microprobe analyses*

Four thin sections from drill holes below and proximal to the RBM pit were analyzed with the electron microprobe at the University of Nevada, Las Vegas using wavelength dispersive spectroscopy (WDS) to identify gold and determine the trace element contents of various sulfide phases associated with the mineralization stages described above. Each spot was analyzed for Ag, As, Au, Bi, Ca, Cu, Fe, Hg, Pb, S, Sb, Si, Sn, Te, Tl, W, and Zn (See Appendix 1 for methodology and data). Samples RBMC4-240 and RBMC2-223, which are from five foot intervals that assayed 28.97 and 22.08 ppm gold respectively, are both from breccias that contain Main-stage pyrite and Late-stage pyrite + marcasite. Sample RBD0601-872.5 is from a magmatic-hydrothermal breccia that contains Early pyrite inclusions in Main-stage chalcopyrite that is rimmed by Late-stage marcasite, and is from a five-foot interval that assayed 3.84 ppm gold. Sample RBD1001-1373 is of megacrystic quartz monzonite porphyry from a five-foot interval that contained 0.0103 ppm gold. The porphyry is cut by quartz-molybdenite veins and

contains disseminated arsenopyrite. Although sample RBD1001-1373 was very low grade, it was selected because it was the sample available for microprobe analyses that best represents early mineralization.

Forty-nine spots were analyzed in this study. Thirty-four of the spots analyzed were on iron-sulfides, mostly late fine-grained marcasite rims, because they are texturally similar to gold-bearing arsenian iron sulfides in Carlin-type deposits (cf. Cline et al., 2005). Of the 34 spots in pyrite and marcasite that were analyzed, only 20 had analytical totals above 96%. Most of the low totals likely resulted from the fine-grained (~5μm) nature of the iron sulfides being analyzed and irregular surfaces on the thin section. The term elevated, as used below, refers to any element that had recorded concentrations above detection limit (See Appendix 1). Average concentrations reported in the text are the average of all analyses with elevated values, and do not include analyses with concentrations below detection limits.

One early euhedral pyrite inclusion in chalcopyrite in the matrix of a Main-stage breccia was analyzed. The pyrite spot contained elevated copper (530 ppm) and tungsten (220 ppm), and slightly elevated silver. Nine spot analyses on pyrite in the matrices of Main-stage breccias were analyzed. Spots analyzed in this group were from large (generally greater than 50μm) anhedral pyrite crystals, some of which contained inclusions of bismuth-bearing sulfides. Five of the nine spots analyzed in this group had elevated arsenic, with the overall average arsenic concentration being 1,910 ppm.

Twenty-one spots on Late-stage pyrite and marcasite were analyzed. These were further subdivided into clusters of fine-grained euhedral pyrite and anhedral marcasite in the matrix of breccias, and marcasite rimming silicates (atoll) and sulfides (rims) and

cutting and replacing earlier sulfides (late veining). The core silicates rimmed by atoll pyrite are most likely quartz but are less than 5μm making identification of mineralogy difficult. Fine-grained pyrite and marcasite spots had elevated copper (6 of 9 analyses above detection limit, averaging 930 ppm), arsenic (8 of 9 analyses above detection limit, averaging 4,280 ppm), and antimony (7 of 9 analyses above detection limit, averaging 570 ppm). In addition, 5 of 7 anhedal marcasite clusters analyzed had elevated zinc (averaging 130 ppm), 3 of which also had elevated bismuth (averaging 360 ppm). Spots analyzed on late marcasite rims and veins had highly variable trace-element compositions. The variation may be due in part to the fine grain size of these phases resulting in poor totals and contamination from adjacent minerals. In one example, a late marcasite vein cutting chalcopyrite contained 3,810 ppm Cu, approximately three times higher than any of the other analyses of late marcasite. Alternatively, this phase may represent marcasite replacement of earlier sulfides, and may therefore inherit the geochemical signature of the sulfides being replaced. The only element that was consistently elevated in late marcasite compared to other phases analyzed was tin. Seven of 12 spots were elevated, averaging 140 ppm.

Eleven spots were analyzed on other sulfide phases including 6 on bismuth-bearing sulfides, and one on each tennantite, chalcopyrite, and arsenopyrite (Table 3 of Appendix 1). All six of the bismuth-bearing minerals analyzed were small 1-10 μm inclusions within euhedral to anhedral pyrite. Of the six analyses on bismuth-bearing minerals, only one had a total >96%, and all contained variable abundances of iron and sulfur. The iron present in these analyses may be the result of mixed signals from surrounding pyrite, and the true composition of this phase was not identified. The

average normalized composition for this phase was 4.5% Fe, 5.5% Pb, 53% Bi, 29% Te, and 8% S. All of the spots analyzed also had elevated silver with an average concentration of 1,250 ppm. The arsenopyrite characteristic of Early mineralizaton had a spot analysis that contained elevated copper (averaging 300 ppm), tungsten (averaging 360 ppm), and tellurium (averaging 80 ppm). The one analysis run on tennantite indicated 35.5% Cu, 20.1% Sb, 4.0% As, and 25.3% S along with 8.0% Zn, 0.042% Sn, 0.021% Hg, and 0.044% Ag. No tennantite standards were run; therefore, these data may have some peak overlap problems that are not accounted for. Two analyses were run on chalcopyrite. These analyses were run using a different method than the rest of the analyses (described in Appendix 1) and may also have some peak overlap problems.

No gold was detected in any of the pyrite, marcasite, or arsenopyrite spots analyzed in this study. Gold above detection limit was only identified in one breccia-healing chalcopyrite spot, at a concentration of 80 ppm. This spot was analyzed using a different technique from the rest of the spots analyzed, and may have problems related to peak overlaps. Nevertheless, it is likely that gold was introduced along with chalcopyrite during Main-stage mineralization. It is also possible that gold occurs in the stages of pyrite and marcasite. The detection limit for gold in the the pyrite and marcasite spots ranged from 27 to 80 ppm, averaging 47 ppm. Therefore, gold could be present at low concentrations ($\leq$~40 ppm) in one or more stages of pyrite or marcasite. However, the presence of native gold in the high-grade sulfide samples suggests that at least some, if not most, of the gold at RBM occurs as free gold. Analyses of 2 of the free gold grains in the high-grade sulfide samples did not detect any silver.

***Trace Elements**: Statistics and Zoning*

A trace element assay data set was compiled for statistical evaluation to define elemental associations in the deposit. The assays are of intervals from 33 drill holes drilled within 3,000 feet of the RBM pit. The intervals range from 2.5 to 10 feet. Fire assays for gold were used, whereas ICPMS analyses, using a nearly complete four-acid digestion, were used for the other elements. Assay were from both oxidized and sulfide-bearing rock, and, because of the variable mobility of elements in the supergene environment, depict both hypogene and supergene elemental associations. In addition, assays are not separated by lithology, so variations in host-rock composition further obscure the hypogene signature. Despite the inherent discrepancies within the data set, Spearman correlations and factor analyses show similar elemental associations, which, when combined with multielement assays on logged core holes and grab samples from the RBM pit and microprobe analyses, are representative of distinct geochemical characteristics of lithologies, alteration assemblages, and mineralization suites.

Factor analysis, using SYSTAT, a commercially available software package, was carried out on the data set to determine elemental associations. Traditional R-mode factor analysis was completed using varimax rotation and a minimum eigen value of 1.00. Varimax rotation was used because it maximizes the variance that each factor represents (Abdi, 2003). The log of all data values for each element was taken before completing the factor analysis, because most elements showed log-normal distributions, and factor analysis is based on normal populations. The calculated factors and the loadings for each element are shown in Table 6. Spearman rank correlation coefficients

were also calculated using SYSTAT, to compare with groupings defined by factor analyses (Appendix 2). The Spearman method of generating correlation matrices was used because it does not rely on a linear relationship between two variables. For example, outliers can strongly influence values of traditional linear Pearson correlation coefficients, but their influence will be reduced by the rank-order Spearman correlations. Elemental groupings defined by factor analyses are consistent with elemental associations defined by Spearman correlation coefficients, and together define the geochemical variations associated with the primary compositions of lithologies, alteration, and mineralization.

Element	Factor 1	Factor 2	Factor 3	Factor 4	Factor 5	Factor 6	Factor 7	Factor 8	Factor 9
LOG Ag	-0.198514	0.455299	-0.165974	-0.013215	-0.040267	0.558432	0.06333	0.139869	0.393775
LOG Al	0.926835	-0.064562	0.191676	0.074419	0.076859	0.048783	-0.110896	0.025523	0.006923
LOG As	0.029313	0.336644	-0.454547	-0.004591	0.064465	0.22448	0.19796	0.504218	0.015381
LOG Au	-0.068413	0.636344	-0.032484	0.424622	0.137135	0.053013	0.000227	0.211521	0.04629
LOG Ba	0.365854	-0.262655	0.269399	-0.112323	-0.070473	0.116548	0.373755	-0.171738	0.162692
LOG Be	0.638209	0.001313	0.454085	-0.144575	0.245291	0.103562	-0.141151	-0.171446	0.064096
LOG Bi	-0.193272	0.754222	0.034849	-0.034449	-0.085364	-0.125426	-0.005442	0.013195	0.392414
LOG Ca	-0.401664	0.380916	0.541713	-0.133577	0.249692	-0.162499	-0.031081	-0.340054	-0.031561
LOG Cd	-0.093924	0.093195	-0.104669	0.150415	0.396944	0.675224	-0.049518	0.059263	0.140852
LOG Ce	0.894256	0.074263	0.087756	-0.050646	0.044679	0.018287	0.007785	0.098384	-0.130821
LOG Co	0.04732	0.142122	0.128539	0.102327	0.869519	0.064131	-0.132785	0.117445	0.102468
LOG Cr	0.480668	-0.161527	-0.187401	0.250142	0.075152	-0.193395	0.548625	0.262711	-0.005838
LOG Cs	0.359485	0.222078	0.705578	-0.053792	0.25801	-0.052974	-0.10248	0.156517	0.138756
LOG Cu	-0.084671	0.413912	-0.058801	0.088135	0.230395	0.131424	0.174467	-0.049265	0.638248
LOG Fe	0.254781	0.403849	0.002585	0.021117	0.432341	0.050925	0.250618	0.34735	-0.412979
LOG Ga	0.948014	-0.025608	0.161149	0.093502	-0.006818	0.045974	-0.025766	0.102133	-0.031463
LOG Ge	0.572413	0.115138	0.145527	0.113721	0.179009	0.053252	0.364	0.213268	-0.196088
LOG Hf	0.866125	0.12213	-0.153966	0.067619	0.004465	-0.030016	0.169389	0.016945	0.028139
LOG In	0.116044	0.790145	-0.052888	0.183674	0.120387	0.210776	-0.101067	-0.008525	-0.089794
LOG K	0.357494	-0.164143	0.812088	-0.156932	-0.036532	0.030308	0.007794	0.245223	0.116919
LOG La	0.843245	0.038892	0.073296	-0.042635	0.044186	-0.047482	0.166394	0.1492	-0.13812
LOG Li	0.435912	0.249855	-0.098014	-0.102624	0.152446	-0.3148	-0.388218	0.096865	0.361177
LOG Mg	-0.380378	0.132707	0.645072	-0.133933	0.206376	-0.065338	0.098297	-0.232084	-0.088643
LOG Mn	-0.278749	0.422	0.38553	-0.164416	0.515557	0.039342	-0.320336	-0.201088	-0.086925
LOG Mo	0.206072	0.151864	-0.16774	0.675684	-0.060245	0.122564	0.061221	-0.012816	0.062305
LOG Na	0.247213	0.052999	0.751918	0.075876	-0.094525	0.030298	0.009841	-0.057365	-0.128961
LOG Nb	0.925296	-0.050494	0.179676	0.171119	-0.044641	0.018558	-0.021186	0.059791	-0.024609
LOG Ni	0.306353	-0.095485	-0.076233	0.174753	0.803415	-0.016719	0.163365	0.057045	0.032763
LOG P	0.545719	0.096213	-0.005321	0.114291	0.229415	-0.213867	0.355689	-0.091916	0.050729
LOG Pb	0.115398	0.137917	-0.0571	0.072899	0.06791	0.825484	-0.089349	0.060932	-0.101997
LOG Rb	0.378201	-0.143008	0.769861	-0.205766	-0.038414	-0.033995	0.04386	0.302182	0.153364
LOG Re	0.187642	0.089708	0.099737	0.734316	0.301243	0.01201	0.046552	0.106184	0.042694
LOG S	0.240399	0.014616	-0.031033	0.532921	0.144561	0.045232	0.188284	0.372298	-0.327978
LOG Sb	-0.116705	0.237533	-0.707053	-0.111884	-0.022428	0.162527	0.196419	0.297602	0.159743
LOG Se	0.096468	-0.142823	-0.035894	0.066695	-0.089463	-0.070912	0.750404	0.07923	0.054764
LOG Sn	0.147724	0.826369	0.042649	0.10583	0.14146	0.20836	-0.208509	-0.040423	0.01944
LOG Sr	0.0389	-0.061199	0.362094	0.103849	-0.216298	-0.220354	0.233195	0.355706	-0.155156
LOG Ta	0.91812	-0.031999	0.201099	0.155847	-0.052738	0.078927	-0.122323	0.026693	-0.017939
LOG Te	0.10192	0.29764	-0.107077	0.43841	-0.178785	0.098366	0.380322	0.333458	-0.072387
LOG Th	0.939342	-0.011257	0.161035	0.037032	-0.021056	0.091237	-0.125174	0.008323	-0.018523
LOG Ti	0.91613	-0.056458	0.05502	0.120691	-0.029761	-0.095437	0.154847	0.121951	-0.020956
LOG Tl	0.273355	0.049768	0.033104	0.228382	0.126364	0.094289	0.036629	0.744999	0.005387
LOG U	0.688138	-0.070669	-0.06234	0.343761	0.171842	0.005992	0.272681	0.090804	0.103889
LOG V	0.62604	-0.22211	-0.073	0.23521	-0.032952	-0.205555	0.495766	0.239119	-0.067545
LOG W	0.135487	0.570179	-0.527746	-0.211307	-0.030106	0.033036	-0.13213	0.071345	0.09335
LOG Y	0.648798	-0.083074	0.181084	0.199711	0.392222	-0.042958	0.312317	0.050582	0.032837
LOG Zn	-0.023094	0.187432	0.007745	-0.017991	0.773206	0.427842	-0.14358	-0.091829	-0.039643
LOG Zr	0.807833	0.098194	-0.176526	0.006546	0.021972	-0.101208	0.273741	0.052628	0.033281
% Varience	25.798	8.919	10.492	5.162	7.325	4.717	5.708	4.651	3.062

Table 6. Factor analyses of the multi-element drill hole database. Factor loadings >0.5 are highlighted in dark yellow and factor loadings >0.4 are highlighted in light yellow. Factor 2, which accounts for 8.919 % of the variance in the data set best represents Main-stage mineralization. Factors 1 and 3 reflect original lithologies and alteration. Factor 4 represents Early mineralization. Factor 5 represents mafic igneous lithologies. Factor 6 may be a skarn mineralization signature. Factor 7 is likely a black shale signature. Factors 8 and 9 may also be mineralization signatures, with Factor 8 possibly representing Late mineralization, and Factor 9 representing supergene enrichment.

Two factors identified in factor analyses have high loadings for gold. Factor 2, which accounts for 8.9% of the variance in the data set has high loadings for Au (0.64), Sn (0.83), Bi (0.75), In (0.79), and W (0.57). Elements with somewhat lower loadings for Factor 2 include Ag (0.46), Mn (0.42), Cu (0.41), and Fe (0.40). Factor 4, which accounts for 5.16% of the variance in the data set, has high loadings for Re (0.73), Mo (0.68), S (0.53), and somewhat lower loadings for Te (0.43), and Au (0.42). The Spearman correlation table also shows an association of Au with Sn (0.551), In (0.570), and Bi (0.458), as well as Te (0.514) and Re (0.450), and, to a lesser degree, As (0.326), Mo (0.317), and Co (0.340). Factor 4 represents Early mineralization, in which molybdenite is the most abundant sulfide present in quartz veins with low, but elevated, gold grades. Factor 2 represents Main-stage mineralization, where gold is associated with Bi-Te-sulfides, pyrite, and lesser chalcopyrite. Te has a loading value of 0.43 in Factor 4, and 0.30 in factor 2, suggesting it was introduced during both Early and Main-stage mineralization. The relatively weak Spearman correlation coefficient of As with Au is supported by a relative low load of 0.34 for As in factor 2, which is most likely the result of Main-stage arsenopyrite as opposed to arsenian marcasite.

Three factors in the factor analysis account for variations in lithology within the deposit. Factor 1, which accounts for 25.7% of the variance in the data set, is representative of elemental variations in different lithologies, showing a particularly strong granitoid signature with high loadings for incompatible elements including Th, Ta, and Nb. Factor 5, accounting for 7.32% of the variance in the data set, has high loadings for Co (0.87), Ni (0.80), Zn (0.77), and lower loadings for Mn (0.52) and Fe (0.43). This signature is the same as the geochemical signature identified in the mafic dikes (Jl)

described above. In contrast, factor 7, accounting for 5.7 % of the variance in the data set, has high loadings for Se (0.75), Cr (0.55), and V (0.50), a black shale suite that is likely related to the Chainman Shale.

Factor 3, accounting for 10.49% of the variance in the data set, likely represents areas of RBM unaffected by Main and Late-stage advanced argillic alteration and supergene alteration. The highest loadings for this factor are K (0.81), Rb (0.77), Na (0.75), Cs (0.71), Mg (0.65), and Ca (0.54), all of which are cations easily leached from host rocks during advanced argillic alteration and supergene alteration. In addition, strong negative loadings for the elements Sb (-0.71), W (-0.53), and As (-0.45) are correlative with high concentrations of As and Sb in late-stage arsenian marcasite mineralization associated with advanced argillic alteration.

Factors 6, 8, and 9 may also be representative of some type of mineralization, although the associations are less obvious. Factor 6, accounting for 4.72% of the variance in the data set, has high loadings for Pb (0.83), Cd (0.68), Ag (0.56), and Zn (0.43). These elements have the highest concentrations in the skarn pod identified in the RBM pit and skarns intercepted in Lower Paleozoic carbonates below, and south of, the RBM pit. Factor 8, accounting for 4.65% of the variance in the data set, has high loadings for Tl and As. Although As is present in late marcasite, no Tl has been identified in late marcasite or any other phase, and the geologic significance of factor 8 is unclear. Factor 9, accounting for only 3.06% of the variance, has a high loading for Cu (0.64) and lower loading for Ag (0.39). This factor may represent supergene enrichment; however, the lowest loadings for factor 9 are Fe (-0.41) and S (-0.33), which suggest a leached cap rather than supergene enrichment.

VI. Summary of Development of the Intrusive Center and Associated Mineralization in Time and Space

Despite the masking of geologic features and relationships by several stages of strong hypogene and supergene alteration, a framework for how the intrusive center at RBM and associated hydrothermal mineralization and alteration developed in time and space can be constructed (Fig. 34). The earliest stages of magmatism and mineralization in the RBM deposit are characteristic of a weak porphyry system, characterized by emplacement of quartz monzonite intrusions and associated potassic alteration, sericitic alteration, quartz veins, and deposition of minor amounts of molybdenite, chalcopyrite, pyrite, arsenopyrite and gold. Intrusion of slightly later quartz monzodiorite dikes and associated silicification appears to mark the beginning of a transition to lower temperatures, a more brittle regime, and more channelized hydrothermal fluid flow. The later system culminated in the emplacement of magmatic-hydrothermal breccias, advanced argillic alteration, and Main-stage gold mineralization, which overprinted the porphyry-style mineralization. Late arsenian marcasite ± pyrite associated with continued advanced argillic alteration, and subsequent carbonatization likely indicate the collapse of the hydrothermal system. Diorite porphyry intrusions with associated propylitic alteration represent a final pulse of magmatism that largely post-dates gold mineralization.

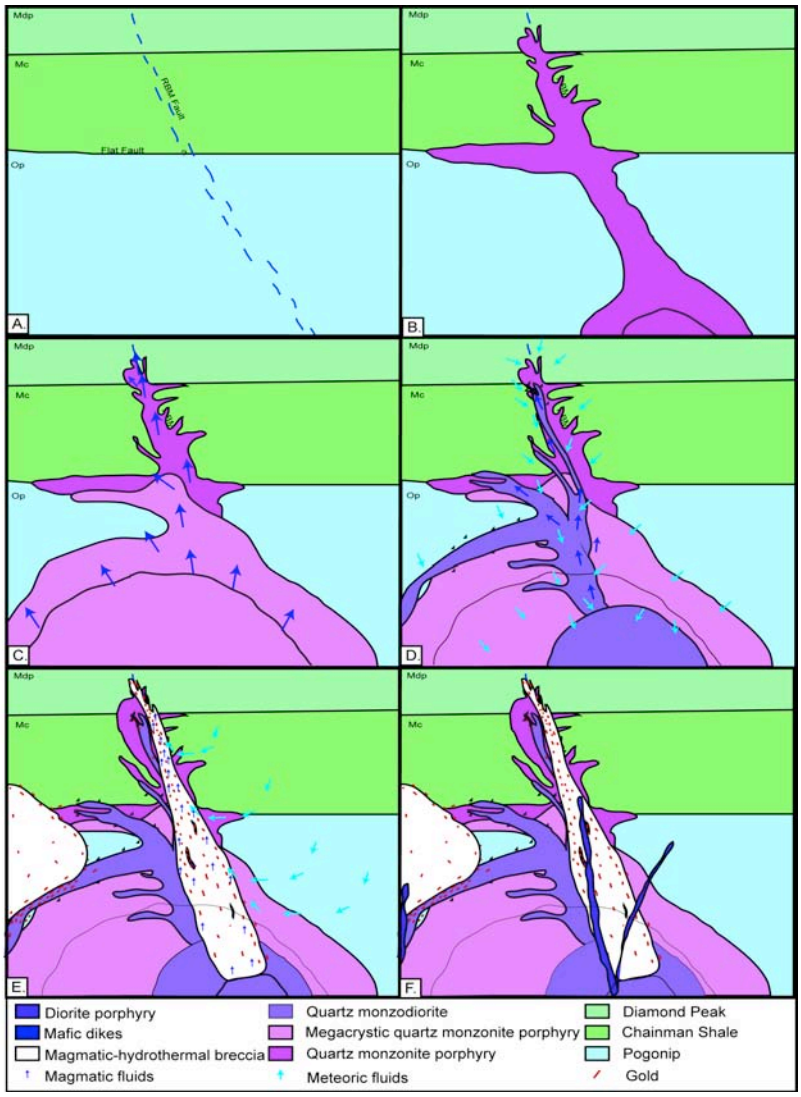

Figure 34. Interpretive northeast cross-section through the RBM deposit, looking northwest. Black bold line indicates location of solid-liquid contact, with light black lines showing the contact in the previous section. A. Pre-intrusion section showing ground preparation along the RBM fault and flat fault. The relationship between these two structures is unknown. B. Intrusion of dikes and sills of quartz monzonite porphyry C. Intrusion of the large megacrystic quartz monzonite porphyry stock (Jmqmp) D. Intrusions of quartz monzodiorite (Jqmd) along the RBM fault and along the upper margins of the megacrystic quartz monzonite porphyry stock during the waning stages of Early mineralization. Upwelling magmatic fluids are localized along dikes and cool during ascent and mixing with meteoric water. Underlying magma chamber retreats. E. Emplacement of magmatic-hydrothermal breccias (Jbx) along the RBM fault and around the flat fault, coincident with intrusion of primitive magmas into the magma chamber as indicated by mafic dikes (Jl) within breccia bodies. Coincident and subsequent acidic magmatic volatiles mix with meteoric water and result in advanced argillic alteration. Gold mineralization was related to these fluids, and was focused along the high-angle breccia body intruding the RBM fault, along the low-angle quartz monzodiorite sills at the base of the breccia body, and to a lesser extent along the upper margins of the breccia body. F. Intrusion of diorite porphyry dikes (Jd) along the margins of the breccia body cutting the argillized breccia body and all earlier phases.

The early porphyry system is representative of a weakly developed porphyry Cu-Mo system associated with quartz monzonite intrusions as classified by Seedorff et al. (2005). The RBM system was associated with emplacement of quartz monzonite porphyry dikes and sills. The dominant northwest strike of quartz monzonite porphyry dikes indicate a structural fabric similar to that which controlled the Bald Mountain stock and associated dikes along the northwest oriented Bida trend elsewhere in the district. The two northeast-striking dikes in the northeast highwall may indicate a secondary structural fabric that is subparallel to the Dynasty fault, providing further evidence that the Dynasty fault and other northeast striking faults also controlled emplacement of Jurassic intrusions. Fine-grained potassium feldspar replacing plagioclase phenocrysts and the groundmass of quartz monzonite and megacrystic quartz monzonite porphyries is similar to early high temperature alteration documented in typical porphyry systems (cf. Seedorff et al., 2005). High gamma ray spectrometer readings in the quartz monzonite porphyry plug in the west side of the pit, and within quartz monzonite porphyry approaching the main RBM breccia lens on the east side of the pit, indicate these fluids were focused along the west side of the pit, but extended outward along the RBM fault.

Sucrosic quartz ± molybdenite veins identified in this study, as well as milky quartz + pyrite + chalcopyrite veins identified by Nutt and Hofstra (2007) are related to this porphyry system. Nutt and Hofstra (2007) interpreted the milky quartz veins to be coeval with sericitic alteration. Although evidence definitively linking quartz veins to either potassic or sericitic alteration was not identified, the spatial association of sucrosic quartz veins with potassic alteration in the RBM pit, and the quartz-orthoclase-molybdenite mineral assemblage identified in drill holes south of the RBM deposit,

suggest quartz veining was associated with potassic alteration. These early quartz-orthoclase-molybdenite and quartz-molybdenite veins are texturally similar to A and B veins, respectively, as defined by Gustafson and Hunt (1975) and are typically associated with potassic alteration in porphyry deposits (Dilles and Einaudi, 1992; Muntean and Einaudi, 2000). In contrast, arsenopyrite, sphalerite, brassy pyrite, marcasite, and galena mineralization intergrown with sericite represents a later phase of mineralization associated with the porphyry system, resulting from a decrease in temperature of hydrothermal fluids from potassium feldspar stable to muscovite stable conditions (from >~550°C to ~300ºC) based on detailed studies of porphyry systems (cf. Seedorf et al., 2005).

Emplacement of quartz monzodiorite dikes documents the beginning of the transition from Early to Main-stage mineralization. The abundance of biotite, slightly elevated Cr content, and local occurrence of trace chromite in quartz monzodiorite dikes indicate they are slightly more mafic than the early porphyry intrusion, and may be representative of recharge of the underlying magma chamber at depth by more primitive magma. The observation of sucrosic quartz veins in quartz monzonite porphyry that are truncated by intrusive contacts with quartz monzodiorite dikes, along with the presence of sucrosic quartz veins cutting quartz monzodiorite dikes, indicates quartz monzodiorite dikes were emplaced during the late-stages of the early porphyry system. The presence of crackle-breccias outboard of quartz monzodiorite dikes signifies a shift in conditions from a ductile to brittle regime resulting from the cooling of the porphyry system. Intense silicification within, and along the margins of quartz monzodiorite dikes also supports cooling of the system.

Intrusion of quartz monzodiorite dikes and subsequent silicification was followed by formation of magmatic-hydrothermal breccia lenses and associated advanced argillic alteration. Magmatic-hydrothermal breccias, based on the classification scheme of Sillitoe (1985), most likely resulted from the rapid release of fluids and volatiles from the cupola of an underlying magma chamber as described by Burnham (1985). Some of the key characteristics that have been used to classify the breccia at RBM as magmatic-hydrothermal include its intimate spatial and temporal relationship with intrusions, especially the quartz monzodiorite and mafic dikes, its location in the upper portions of a porphyry stock, lack of an identifiable igneous matrix in breccias, and lack of significant upward or downward transport of fragments. The spatial association between quartz monzodiorite dikes, silicification, and magmatic-hydrothermal breccias indicates that the same favorable northwest-trending structural fabric intruded by quartz monzodiorite dikes was utilized during rapid fluid release, expansion and brecciation. Ascending acidic aqueous magmatic volatiles were responsible for brecciation, pervasive leaching of the country rocks, and advanced argillic alteration. Intensely altered and sulfidized mafic dikes are isolated to, and appear to cross-cut breccias, which further supports replenishment of the underlying magma chamber, resulting in violent exsolution of magmatic volatiles and formation of the Main-stage breccias and mineralization.

Main-stage mineralization is associated with advanced argillic alteration that occurred during and after emplacement of magmatic-hydrothermal breccias. Ore-bearing fluids took advantage of the increased permeability resulting from brecciation, precipitating pyrite ± marcasite and locally chalcopyrite, arsenopyrite, Bi-minerals, and native gold in the matrices of breccias. Nutt and Hofstra (2007) claimed most of the gold

at RBM was introduced during "a second stage of mineralization" which includes "native gold, disseminated anhedral to cubic pyrite, sphalerite, molybdenite, chalcopyrite, Bi sulfide minerals, tetrahedrite, arsenopyrite, galena, and trace amounts of pyrrhotite, bornite, and stannite" that was associated with "sericite and dickite alteration and silicification of sedimentary host rocks." The presence of breccias with sericitically altered, silicified, and quartz + molybdenite ± euhedral pyrite mineralized clasts in a matrix that is pervasively argillized and mineralized with pyrite, marcasite, and locally chalcopyrite, Bi-bearing minerals and native gold indicate Nutt and Hofstra's "stage two" mineralization is a composite of Early and Main-stage mineralization as defined in this study. In addition, factor analysis distinguishes two geochemical signatures – the Early mineralization event (Factor 4 including Mo, Te, and to a lesser extent, Au, Table 6), and the Main-stage mineralization event (Factor 2 including Au, Sn, Bi, W, and, to a lesser extent, Ag, Mn, Cu, Fe, and Te, Table 6). Although no Sn-bearing minerals were identified in this study, stannite, identified by Nutt and Hofstra (2007), was likely deposited during Main-stage mineralization and responsible for the correlation between Sn and Au. The petrographic observations of native gold grains intergrown with kaolinite in the matrix of sulfide-bearing breccias, as well as the high degree of variance accounted for by factor 2, the high loading value for gold within factor 2, and the high Spearman correlation coefficients of gold with Sn and Bi indicate that the majority of gold was introduced during Main-stage as opposed to Early mineralization. This interpretation is further supported by pit mapping and core logging, which shows a clear spatial association between breccia lenses and high gold grades (Plate 1).

Late-stage mineralization is characterized by the presence of kaolinite with fine-grained and botryoidal pyrite and marcasite rimming and cutting earlier sulfides and clasts in breccias. Nutt and Hofstra (2007) identify this stage of mineralization and note that it superficially resembles sooty pyrite in Carlin-type deposits, but interpret it instead to have formed as a result of destruction of earlier formed base-metal sulfides during the collapse of the hydrothermal system or during supergene alteration based on microprobe analyses and stable isotope analyses of kaolinite. Microprobe analyses from this study, as well from Nutt and Hofstra's study, identify the late-stage pyrite and marcasite as having higher arsenic and antimony concentrations than other phases. Some of the late-stage marcasite identified in this study, described as late rims and veins, show highly variable trace-element compositions which are consistent with Nutt and Hofstra's interpretation that it formed from the destruction of earlier formed sulfides. The volumetrically more abundant Late-stage marcasite and pyrite, described here as fine-grained marcasite and pyrite, show a more consistent trace element composition and is unlikely to have formed from destruction of earlier base-metal sulfides. In addition, the high Spearman correlation coefficients between As and Sb suggest that these two elements were deposited together in late-stage marcasite and pyrite. The geochemical signature identified in Factor 3, with strong positive loadings for leachable cations, and strong negative loading for As and Sb, indicate that Late-stage mineralization is associated with further advanced argillic alteration. The absence of any gold above detection limit (~47 ppm) in late pyrite and marcasite, weak Spearman correlation coefficients between Au and As and/or Sb, low loadings for As and Sb in Factor 4 (Early mineralization) and Factor 2 (Main-stage mineralization) support the interpretation made

by Nutt and Hofstra (2007) that no gold was introduced during the late phase mineralization. Hitchborn et al. (1996) suggest that fine-grained intragranular pyrite infilling brecciated base metal sulfides probably deposited most of the gold at RBM. This interpretation likely groups Main-stage gold related mineralization with Late-stage mineralization as defined in this study, and, therefore, misrepresents the relationship of gold with late fine-grained pyrite and marcasite.

Late-stage barite and ankerite-pyrite veins along with propylitic alteration in diorite porphyry dikes documents the final gasp of the underlying magma chamber. Although diorite porphyry dikes are rare, they cut quartz veins and are consistently propylitically altered, where other intrusions are affected by potassic, sericitic, silicic, or advanced argillic alteration. Considering that these dikes have a high iron content, they would react readily with sulfur in hydrothermal fluids through sulfidation resulting in abundant iron-sulfides, a decrease in the total sulfide content of the hydrothermal fluids, and the precipitation of gold. The lack of pyrite and gold in the diorite porphyry dikes indicate that they were not involved in sulfidation reactions, and are most likely post-mineral. The transition from early quartz monzonite porphyry to quartz monzodiorite and late diorite porphyry intrusions documents a transition from early felsic to later mafic magmatism which most likely signifies multiple recharge events of a large magma chamber at depth by more primitive magmas.

VII. Radiogenic Dating and Thermochronology

Four radiogenic/thermochronologic techniques were utilized to constrain the age and thermal evolution of intrusive and hydrothermal activity at RBM. Four U/Pb dates on zircons define the emplacement age of intrusions. The cooling history and low-temperature hydrothermal history was constrained from a single $^{40}Ar/^{39}Ar$ date on phlogopite, 12 (U-Th)/He dates on zircons from 5 samples, and two (U-Th)/He dates on apatite crystals from one sample, which, as described below, constrains the cooling history of the rocks from ~345°C, through 150-200ºC, down to 60ºC. These data were compiled with previously published apatite fission track data and modeled with the HeFTy software (Ketcham, 2005; Ketcham, 2008), an inverse modeling package that constrains thermal histories of datasets.

Dating Methodology

Heavy Mineral Separations

Mineral separations for U/Pb and (U-Th/He) dating were completed at the University of Arizona, Tucson. U/Pb analyses were completed under the supervision of George Gehrels and the Arizona LaserChron staff, and (U-Th)/He analyses were completed under the supervision of Pete Reiners and his staff. Six samples were run through a crushing and a heavy mineral separation circuit. Heavy mineral separates were run through a Franz magnetic separator to remove any magnetic minerals. Samples with abundant pyrite were broken into two fractions, one for (U-Th)/He analyses and one for U/Pb analyses that was reacted with nitric acid to dissolve pyrite. Zircons and apatites

were picked by hand from the remaining heavy mineral separates, using a binocular microscope.

U/Pb

The premise of this dating technique is that U and Th decay to produce ^{208}Pb, ^{207}Pb, and ^{206}Pb, and that each process takes place at a constant rate which is defined as the half life or time it takes for half of the parent isotope to decay to its respective daughter isotope. In order to calculate the age of a zircon crystal, the concentration of radiogenic isotopes is compared to the original concentration of parent isotopes. Although it is impossible to measure the original concentration of parent isotopes in a crystal directly, the concentration of non-radiogenic ^{204}Pb measured in a crystal can be used in a ratio to radiogenic isotopes to define the age of the zircon crystal. Zircon is the most widely used mineral in U/Pb dating because it is retentive with respect to U, Th, and Pb, is widely distributed in rocks, and incorporates a large amount of U and Th relative to Pb in its crystal structure (Faure, 1986).

Approximately 30 zircon grains were collected from samples with abundant zircons (RBMAD5 and RBMAD7) and fewer were collected from samples with sparse zircons (RBMAD1 and RBMAD2). Zircons were mounted in epoxy around 5 shards of zircon from a Sri Lanka standard with a known isotope dilution – thermal ionization mass spectrometry (ID-TIMS) age of 563.5 ± 3.2 Ma (2-σ). The mount was polished to expose a cross-section through zircon crystals. Samples and standards where analyzed at the University of Arizona LaserChron Center's Laser Ablation MultiCollector - Inductively Coupled Plasma Mass Spectrometer (ICPMS). Without using cathodoluminesence, the

outer margins of zircon crystals were ablated with a 10 μm diameter laser beam to minimize a mixed signal generated from ablating partial rims as well as inherited cores. Multiple cores, identified optically as the center of large zircon crystals which, when ablated, resulted in old ages compared to other spots within the same crystal, define an inheritance age of ~1.8 byr.

Isotopic ratios were analyzed using Agecalc provided by George Gehrels. Agecalc is an off-line Excel spreadsheet equipped with VBA macros that is fully automated to import data from Isoprobe files, perform all necessary corrections, and calculate ages, uncertainties, and error correlations (Gehrels, in review). The data are standardized to the age of the Sri Lanka zircon standards and all analyses from each individual sample are compiled into concordia plots. Where concordant ages are not defined, an age is assigned based on the lower intercept of the discordia. The statistical error for each analysis was added quadratically to the systematic error of the processes, generating a final age for each sample.

(U-Th)/He

The (U-Th)/He dating system is based on analyses of ^{4}He ejected from U, Th, and Sm during alpha decay. ^{238}U, ^{235}U, ^{232}Th, and ^{147}Sm all undergo alpha decay to produce ^{4}He along with daughter isotopes. By summing the number of alpha particles ejected in each system during one half-life, and multiplying the number of alpha particles ejected by the half-life of the isotope, the total ^{4}He produced by radioactive decay is calculated. The total ^{4}He in a crystal is measured by heating the crystal with a laser to degas ^{4}He from the crystal. The degassed ^{4}He is then spiked with ^{3}He and the ratio of ^{4}He to ^{3}He is measured

with an ICPMS. The remaining crystal is dissolved, spiked, and analyzed with an ICPMS to define the abundance of parent isotopes (U, Th, and Sm). Combining the concentration of U, Th, Sm, and He with each systems decay constant, a He age can be defined using equation 1.

$$[^4He] = \sum_{J=1}^{4} \frac{P_j}{\lambda_j} e^{\lambda j t} - 1$$

$p_1 = 8\,\lambda_1[^{238}U]$ $\quad \lambda_1 = 1.55125 \times 10^{-10} a^{-1}$

$p_2 = 7\,\lambda_2[^{235}U]$ $\quad \lambda_2 = 9.8485 \times 10^{-10} a^{-1}$

$p_3 = 6\,\lambda_3[^{232}Th]$ $\quad \lambda_3 = 4.9475 \times 10^{-11} a^{-1}$

$p_4 = 1\,\lambda_4[^{147}Sm]$ $\quad \lambda_4 = 6.539 \times 10^{-11} a^{-1}$

Equation 1 (Dunai, 2005)

Unlike the Pb that has been formed from uranium decay, which remains in the location it was formed, ^{4}He can leak out of the expanded crystal lattice of a hot crystal. When a crystal cools below the temperature at which ^{4}He can no longer leak out of the crystal (defined as the closure temperature of a mineral), ^{4}He begins to accumulate. Subsequent heating events, independent of the original cooling event that formed the crystal being analyzed, can expand the crystal lattice of that mineral, which could allow some or all of the previously accumulated ^{4}He to escape, resulting in a partial or complete reset of the geochronometer. Different minerals require different amounts of heat to expand their crystal lattices, and therefore have different closure temperatures. To identify the closure temperature of zircons, Reiners et al. (2004) analyzed whole zircon crystals as well as interior chips of gem-quality zircons with a wide range of ages and U concentrations to quantify the closure temperature as a function of the diffusion rate of

^{4}He in the crystal and the activation energy of ^{4}He in the mineral. Zircons with large diameters, and those that are heated for a short period of time, or cool through the closure temperature rapidly, have the highest closure temperatures. Zircons analyzed by Reiners et al. (2004) had activation energies that ranged from 163 to 173 Kj/mol, and average diffusion rates of $0.46^{+0.87}_{-0.30}$ cm^2/sec. These values result in a closure temperature of 171-196°C for a cooling rate of 10°C/m.y and zircons with an effective grain radius of 60 μm (Reiners et al., 2004). Similar step-heating experiments on apatites define a closure temperature of 50-75° (Fig. 35).

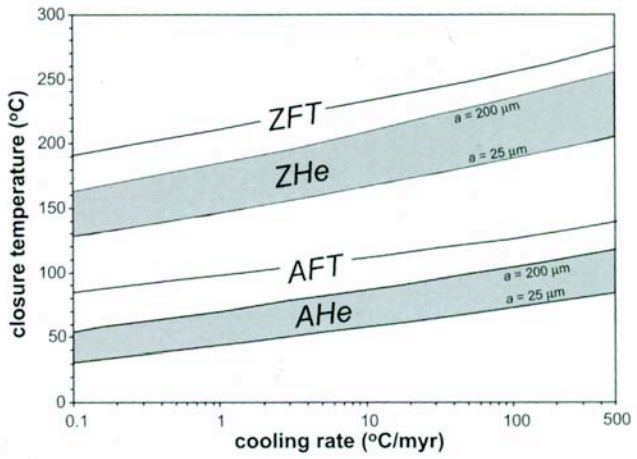

Figure 35. Plot of cooling rate vs. closure temperature for low-temperature geochronometers from Reiners (2005). Zircons analyzed in this study had effective radii (a) between 25.5 and 50.25 μm, with an average radius of 40 μm.

During alpha decay, ^{4}He released can travel up to 20 μm from the parent isotope. Because the ^{4}He may travel in any direction, ~50% of the He released from the outer margin of a zircon crystal may be lost to the surrounding rock, while none of the He released from the core of a thick zircon crystal (>20 μm radius) will be lost to the surrounding rock. To compensate for lost ^{4}He, an alpha ejection correction is used which calculates the amount of ^{4}He that was likely lost to the surrounding rock based on the size

and geometry of the analyzed crystal. In order to minimize the effect of alpha ejection, complete unbroken crystals with radii >30 μm were preferentially chosen from each separate. In samples without ideal crystals, slightly thinner and/or broken crystals were run. In apatite crystals, transmitted and cross-polarized light was also used to identify and discard any crystals that had mineral inclusions in order to prevent contamination of the (U-Th)/He age. Each crystal was photographed, and its thickness and height were measured. Zircon crystals were then placed in niobium tubes, whereas apatite crystals were placed in palladium tubes. Tubes that contained crystals to be analyzed, as well as niobium tubes with zircons from the Fish Canyon Tuff and palladium tubes with Durango apatites for standards, and blank niobium and palladium tubes for line conditions, were heated with a laser beam, which degassed the He from each of the crystals. The degassed ^{4}He was then measured in a mass spectrometer. Zircons and apatites were then dissolved by Pete Reiners' staff and run through an ICPMS to determine the concentrations of U, Th, and Sm. The concentrations of U, Th, Sm, and He were then combined with the geometry of each crystal by Pete Reiners to define an age for each apatite and zircon.

Ar/Ar

$^{40}Ar/^{39}Ar$ dating is based on the decay of ^{40}K to ^{40}Ar through electron capture and by positron emission. Instead of directly measuring the K concentration of the sample analyzed, the method quantifies the amount of K in the sample by irradiating an unknown, along with samples of known age, in a nuclear reactor to produce ^{39}Ar from ^{39}K. Because the ratio of $^{40}K/^{39}K$ is consistent in nature, the ^{39}Ar indirectly represents the ^{40}K in the sample (McDougall and Harrison, 1999). The ratio of $^{40}Ar/^{39}Ar$ is then

measured directly in the unknown sample, and combined with the neutron flux of samples with known ages, to define the age of the unknown sample. The method is preferred over traditional K/Ar dating because it only requires measurement of the isotopic ratio of $^{40}Ar/^{39}Ar$ and can therefore be used to directly date incremental amounts of Ar released from a sample as it is heated. In this study, the sample was analyzed using the step-heating method where it was heated to, then held at, 12 different temperatures, resulting in 12 dates. In samples that have experienced no thermal events since crystallization, the 12 dates should all be near identical. Alternatively, in samples that have experienced heating events after crystallization, younger ages may result from early heating steps, which represent Ar that was degassed from cleavage plains and the outer portions of crystals. Late heating steps may represent Ar released from near the core of crystals that was not released by heating events, and will therefore result in older ages. The temperature required to release Ar from a crystal is dependent on the grain size of the crystal and the composition of the crystal being analyzed. A blocking temperature of ~345°C for phlogopite is assumed in this study (described below).

One phlogopite separate was prepared for $^{40}Ar/^{39}Ar$ dating. Phlogopite from sample RBD0601_947 was analyzed under a scanning electron microscope to verify purity of the phlogopite phase, prior to hand-picking clear inclusion-free mica plates under a binocular microscope. The phlogopite separate was prepared for analysis by the Nevada Isotope Geochronology Lab at the University of Nevada, Las Vegas under the supervision of Terry Spell. The sample was irradiated at the Oregon State University Radiation Center, and then analyzed at the University of Nevada, Las Vegas using a 12-

step furnace step heat in a double vacuum resistance furnace similar to the Staudacher et al. (1978) design.

Descriptions of Dated Samples

RBMAD1. Sample of quartz monzodiorite dike that cuts the main quartz monzonite porphyry plug on the southwest side of the RBM pit. The dike is composed of ~30% ~0.2 mm anhedral quartz and ~65% kaolinite. The sample is oxidized, but previously contained ~5% pyrite, based on the presence of ~1 mm cubic leached cavities. Locally, hematite exsolution lamellae occur with rutile and likely represent primary Fe-Ti oxides. The dike cuts thin (<1mm) quartz veins in the quartz monzonite porphyry plug indicating the intrusion post-dates a quartz-veining event. The sample is within 20 feet of a breccia body with blasthole assays >0.34 ppm Au. The sample yielded few zircons. Five zircons were used for U/Pb dating, and 2 zircons were used for (U-Th)/He dating.

RBMAD2. Sample of a narrow (<1 m) diorite porphyry dike that cuts the main quartz monzonite porphyry plug on the west side of the RBM pit. The dike contains ~5% plagioclase (~1-2 mm) and 7% hornblende (~0.5-2 mm) phenocrysts in a groundmass of feldspar and hornblende with a grain size of ~0.2 mm. The rock is strongly altered to chlorite + calcite, masking most of the primary mineralogy. Sparse (<1%) rounded quartz xenocrysts up to 5 mm in diameter with narrow calcite overgrowths occur as individual and composite crystals. Trace amounts of very fine-grained, disseminated pyrite are present. Quartz-limonite-ankerite veins that cut the adjacent quartz monzonite porphyry, assayed 0.034 ppm Au, and are truncated by the diorite porphyry dike, which

assayed 0.0069 ppm Au. The sample yielded only 14 zircons – all of which were used for U/Pb dating.

RBMAD3. Sample of a weakly brecciated quartz monzonite porphyry, collected about 3 m into the hanging wall of the major northwest-trending breccia body in the northwest corner of the pit. Relict primary mineralogy consists of ~8% resorbed quartz phenocrysts (0.2-1 mm), ~10 % feldspar phenocrysts (0.5-1 mm long), and ~3% biotite phenocrysts (~0.5 mm). Both the feldspar and biotite sites are almost completely altered to clay; the biotite sites also contain leucoxene. The groundmass is completely altered to fine-grained (<0.05 mm) quartz and kaolinite. The sample yielded abundant zircons and was dated using (U-Th)/He to constrain the age of Main-stage mineralization associated with the major breccia body.

RBMAD5. Sample of megacrystic quartz monzonite porphyry taken from the 1219-1238 foot interval of core hole RBD1001 drilled ~150 m south of the RBM pit. The sample consists of 10% weakly resorbed quartz phenocrysts (~1-3 mm), 15% tabular feldspars phenocrysts (~1-3 mm), 1-2 % biotite phenocrysts (~0.5 mm), and sparse (<1%) potassium feldspar megacrysts (~10-20 mm) in a fine-grained (~0.2 mm) groundmass of quartz and sericite. Feldspars phenocrysts are altered to sericite + kaolinite, whereas biotite phenocrysts are altered to sericite + pyrite + leucoxene. Quartz phenocrysts have irregular 0.1-0.5 mm overgrowths of secondary quartz with abundant ~10 μm inclusions of sericite and sparse inclusions of pyrite. Millimeter to centimeter-thick veins of very fine-grained pyrite ± marcasite cut the interval, which assayed 0.206 ppm Au, and occurs

10 feet below a 25-foot interval of breccia that averaged 1.27 ppm Au. The breccia interval also averaged 661 ppm Bi, 104 ppm W and 4,866 ppm As. The sample is considered representative of Main-stage breccia-healing mineralization and appears to be overprinted by Late-stage mineralization as indicated by high the As content and fine-grained pyrite ± marcasite. The sample yielded abundant zircons, which were dated using U/Pb and (U-Th)/He. The U/Pb dating was aimed to test whether megacrystic quartz monzonite porphyries from drill core were emplaced contemporaneously with the quartz monzonite porphyries that crop out in the RBM pit. The sample is considered to be weak mineralization that is proximal to Main-stage mineralized breccia, and, therefore, the (U-Th)/He dating was aimed to constrain the age of deep Main-stage gold mineralization.

RBMAD7 Sample of a pod of potassically altered quartz monzonite porphyry. The rock is composed of ~15% plagioclase phenocrysts (~2 mm), ~10% resorbed quartz phenocrysts (1-3 mm), and ~1-2% mafic phenocrysts set in a fine-grained groundmass (0.5-2 μm) of embayed quartz, secondary potassium feldspar, and sparse sericite. Plagioclase phenocrysts display relict twinning and are partially to completely replaced by fine-grained potassium feldspar, which is overprinted by carbonate + sericite ± chlorite ± epidote. The mafic phases are completely replaced by fine-grained epidote, which also occurs in veins and pods throughout the rock. Sparse, discontinuous, 0.1-0.5 mm quartz veins with serrated vein walls and accessory brassy pyrite and sparse pods of calcite and chlorite cut the dike. Pods of silicification, consisting of fine-grained quartz (~0.05 mm) occur proximal to the quartz veins. The sample yielded abundant zircons

and was dated using both U/Pb and (U-Th)/He. In addition, apatite was separated for (U-Th)/He dating to constrain the age of any low temperature alteration and potential isotopic resetting, which could then be used to constrain thermal modeling. The sample was not proximal to any major structures identified and, therefore, likely represents an early, disseminated, alteration age, which should not be reset by later fluids flowing along structures.

RBMAD10 Sample of cuttings from blasthole 139, which was drilled on the 6800 level of the RBM pit into a breccia body with strong quartz-kaolinite alteration that trends northwest along the northeast high wall. The sample is oxidized but contains abundant limonite and vugs lined with opaline silica, which suggest abundant original pyrite. The fire assay for this hole was 17.69 ppm Au. Given the high grade, this sample was considered to have the best chance of being reset if there was significant Tertiary-aged gold mineralization. The sample, however, yielded only a few zircons. The two best zircons were used for (U-Th)/He dating.

RBD0601_947 Sample of skarn collected from core drilled 947 feet beneath the RBM pit. The skarn is located 35 feet above a quartz monzonite porphyry dike. The skarn mineralogy is composed of phlogopite, actinolite, chlorite, and serpentine that is locally veined by calcite. Given the abundance of Mg-silicates, the protolith was most likely a dolomite. Phlogopite occurs as books up to 5 mm in length, concentrated in veins and pods within the skarn. The core interval assayed 0.048 ppm Au, and is 30 feet above a zone of that assayed 0.16 ppm Au, and 70 feet above an interval that averaged 0.32 ppm

Au. The sample was selected for $^{40}Ar/^{39}Ar$ dating because of the coarse nature of phlogopite, and should reflect either skarn alteration associated with intrusions or fluids associated with proximal low-grade gold mineralization if they are high temperature (above ~345ºC) and later than skarn formation.

Results

U/Pb

Three of the four U-Pb samples dated yielded concordant U-Pb ages, which ranged from 163.9 to 161.8 Ma (Fig. 36). The fouth age was discordant, but intersected the concorida at 163.5 Ma. All of the U-Pb ages had overlapping error bars indicating individual intrusive events cannot be differentiated (Table 7). The overlapping ages of intrusions suggest they represent different pulses from the same magma chamber at depth and were likely all emplaced in <3 million years. The presence of sparse potassium feldspar megacrysts in sample RBMAD5 similar to those found in the Bald Mountain stock near the Top deposit imply that the intrusions dated at RBM are related to the Bald Mountain stock and other quartz feldspar intrusions elsewhere in the district, which have also been dated as Jurassic in age. In addition, the occurrence of diorite porphyry dikes in and near the RBM deposit which are interpreted as post-mineral based on their field relationships and lack of alteration indicate that intrusions and Main-stage hydrothermal alteration and mineralization, as defined in this study, are older than the ~161 Ma U/Pb age for sample RBMAD2.

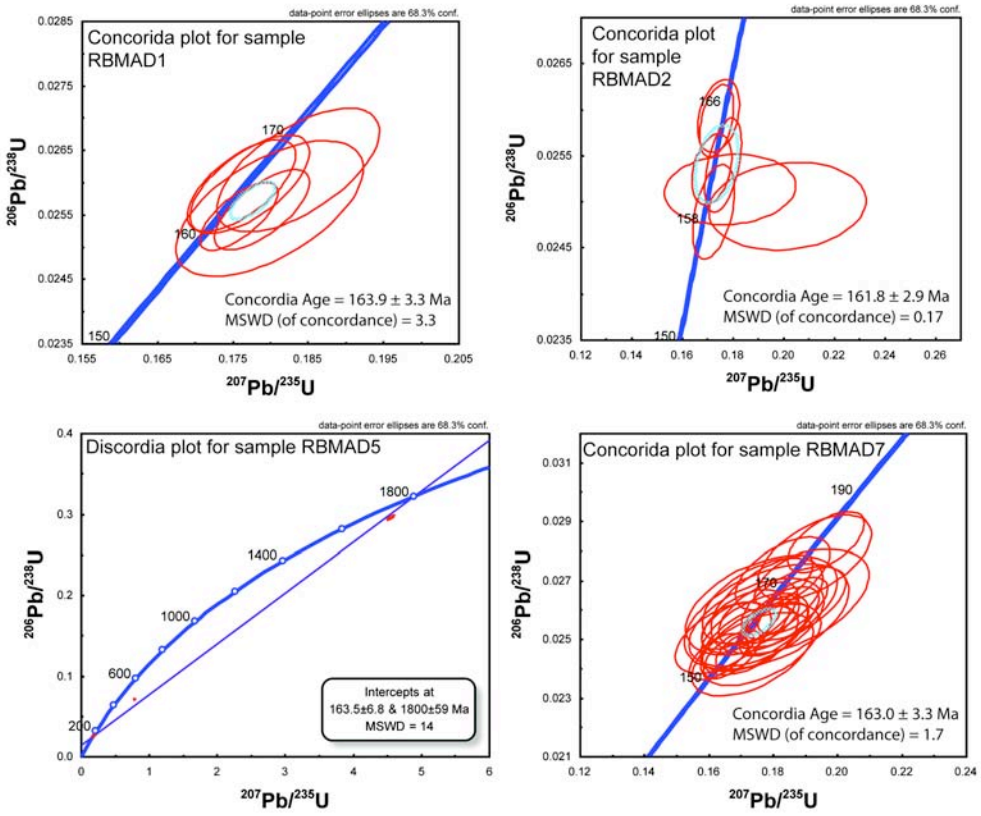

Figure 36. U/Pb LA-ICPMS dates for samples from this study. Samples RBMAD1, RBMAD2, and RBMAD7 produced concordant ages. Sample RBMAD5 did not produce a concordant age and the lower intercept of the discordia was used as the most likely age of emplacement for the intrusion dated. The upper intercept is likely an inheritance age.

The ages from this study are distinctly older than those reported in Mortensen et al. (2000) and Mortensen (2007) on similar intrusive rocks from the Bald Mountain mining district. Mortensen (2007) dated the megacrystic quartz monzonite porphyry from drill hole RBD1002 near the RBM pit at 158.5 ± 1.1 Ma using a weighted mean age from 15 TIMS analyses. The same rock type was dated in this study using a concorida plot from LA-ICPMS data, and yielded an age of 163.5 ± 6.8 Ma. Although these ages overlap, other crosscutting dikes, including RBMAD1, were dated at 163.9 ± 3.3, indicating a discrepancy in the two dating techniques. Gehrels et al. (in review) have

analyzed zircons, using both LA-ICPMS and ID-TIMS and found that LA-ICPMS analyses consistently yield average ages within 2%. The difference between the LA-ICPMS dates obtained in this study and the ID-TIMS ages obtained by Mortensen are within 2% when added to the 2-sigma standard deviations for each age. An exception is a thin basaltic andesite dike collected from 2km southeast of the RBM pit that Mortensen dated at 152.4 ± 1.4 Ma (Sample US1, Mortensen, 2007) that appears to be similar to post-mineral diorite porphyry dated in this study (sample RBMAD2). The relationship between the basaltic andesite sample that Mortensen dated and the diorite porphyry dated in this study is unclear. The data from this study verify that all intrusions dated at RBM are Jurassic and were emplaced at ~160 Ma.

Sample Number	BMMG_X	BMMG_Y	BMMG_Z	Lithology	Description	Alteration	Reason Sampled	U/Pb zircon	(U-Th)/He Zircon	(U-Th)/He Apatite	Zircon Recovery
RBM AD_1	49030	38007	6825	Jqmd	Fine-grained equigranular dike	Advanced Argillic	Distinct lithology cutting quartz veins	163.9 ± 3.3	1. 148.2 ± 6.76 2. 145.39 ± 5.64		Sparse
RBM AD_2	48910	38484	6875	Jdp	Sparsely porphyritic mafic dike	Propylitic	Distinct lithology cutting weakly mineralized calcite-limonite veins	161.8 ±2.9			Sparse
RBM AD_3	48964	38936	6875	Jqmp	Fine-grained quartz-feldspar porphyry	Advanced Argillic	Porphyry along a major NW oriented breccia body		1. 156.13 ± 7.22 2. 145.28 ± 5.60 3. 142.86 ± 5.78		Abundant
RBM AD_5	50098	37045	6136	Jmqmp	Quartz-feldspar porphyry with sparse potassium feldspar megacrysts	Sericitic	Megacristic porphyry in core hole RBD1001 1219-1238	163.5 ± 6.8	1. 140.25 ± 5.50 2. 90.92 ± 3.40		Present
RBM AD_7	49065	38586	6825	Jqmp	Fine-grained quartz-feldspar porphyry	Potassic	Potassically altered porphyry with primary texture preserved	163.0 ± 3.4	1. 160.11 ± 6.12 2. 157.82 ± 6.04 3. 141.57 ± 5.36	1. 18.56 ± 1.46 2. 19.96 ± 2.82	Abundant
RBM AD_10	49421	38408	6800	Jbx	Finely-milled breccia	Advanced Argillic	High grade blasthole sample with a fire assay of 17.69 ppm Au		1. 139.82 ± 5.32 2. 113.41 ± 4.16		Present

Table 7. Location and brief description of each rock sample dated in this study as well as the dating method and resulting ages. All ages are given with 2-σ errors. Coordinates given in Bald Mountain Mine Grid.

(U-Th)/He

(U-Th)/He dates show a wider range of ages than the U/Pb dates (Table 7). Possible reasons for this variation include slow cooling of samples, later thermal events that may have resulted in partial resetting of individual samples, and variation in crystal chemistry and morphology. Characteristics of samples and zircons, including size, shape, and composition, may help elucidate the reasons for variation, but cannot alone definitively identify the reason for the wide age range.

If the samples dated in this study were heated by intrusions and/or hydrothermal fluids for a long period of time to temperatures greater than ~180°C, and then cooled slowly over millions of years, then the (U-Th)/He age would reflect the time at which the sample cooled below ~180°C and not the peak of magmatic and/or hydrothermal activity. If gold mineralization occurred at temperatures well in excess of 180ºC at RBM, then the (U-Th)/He dates reflect minimum ages for mineralization, and the dates may be significantly younger than the gold mineralization. Alternatively, if the samples were heated by igneous or hydrothermal activity for a very short period of time, temperatures much higher than 180ºC would be required to release all of the He from crystals and completely reset the (U-Th)/He age of the crystals. If samples were heated above the closure temperature for too short of a period of time to release all of the radiogenic helium from the crystals, but long enough to release some of the radiogenic helium from the crystals, then the (U-Th)/He date would be partially reset. Partially reset dates would be younger than the actual age of rock formation but older than the actual age of the later thermal event.

Compositional and morphologic features of individual crystals can affect (U-Th)/He dates. For example, high U concentrations result in radiation damage of zircon crystals, which allows He to escape from the crystals and results in artificially young ages (Reiners et al., 2004). Also, zircons can be broken during emplacement (e.g. brecciation) or during mineral separation. Because it is impossible to verify when crystals were broken, the alpha ejection correction, which accounts for He that escapes from the outer edges of the crystal, assumes that crystals were broken during emplacement, and overcompensates for released He if the crystal was broken during mineral separation, resulting in artificially old ages (Reiners, 2005). While some of the variation in zircon ages in this study suite can be explained based on the characteristics described above, the variation between zircon ages for individual samples in many cases cannot be explained soley by radiation damage.

Zircons from sample RBMAD7, which was a sample chosen to date early disseminated potassic alteration, have a large age discrepancy between individual zircons, with an age of 142 Ma for zircon #3 being significantly younger than the 160 and 158 Ma ages for zircons #1 and #2, respectively. Zircon 3 has a narrow fracture parallel to the *c* axis and abundant inclusions that may result in the younger age. For this reason the interpreted alteration age for the sample is ~159 Ma based on an average of zircons 1 and 2. The U/Pb age for zircons from this sample is 163.0 ± 3.4 Ma, and indicates a possible short temporal gap between emplacement and closure of the (U-Th)/He system. Alternatively, the U/Pb and the (U-Th)/He dates on zircons 1 and 2 may represent the same or very close ages at ~160 Ma which lies within the error of all three ages, and could be the result of short duration cooling. Two apatite crystals from RBMAD7 yield

overlapping (U-Th)/He ages with a mean age of ~19 Ma, interpreted to represent the presence of a late low-temperate thermal event. The 19 Ma (U-Th)/He age for the apatite, and the two (U-Th)/He ages for zircons which overlap with the emplacement age for the rock, indicate that the thermal event that reset the apatite age did not heat the zircons from this sample to a high enough temperature for a long enough period of time to reset the zircon ages. Based on Reiners (2005), assuming a cooling rate of 200ºC/myr, the thermal event that reset the apatite was likely between 50 and 150ºC (Fig. 35).

The three (U-Th)/He ages from three separate zircon crystals from sample RBMAD3 do not overlap statistically. The ages are 156.13 ± 7.22 (RBMAD3z1), 145.28 ± 5.6 Ma (RBMAD3z2), and 142.86 ± 5.78 (RBMAD3z3). Zircon 1 has a broken termination, whereas zircons 2 and 3 are complete. If the zircon was broken during the mineral separation process, the alpha ejection correction based on the morphology of the crystal may overcompensate for He lost, and give an older age than the age of closure of the (U-Th)/He system. This may account for the age discrepancy. If the RBMAD3z1 age of 156.13 is discounted, the mean age for RBMAD3z2 and RBMAD3z3 is 144 Ma. The quartz monzonite porphyry dated in RBMAD3 is very similar to quartz monzonite porphyry sample RBMAD7, which was emplaced at 163.0 ± 3.4 Ma based on the U/Pb dates discussed above. Assuming RBMAD3 and RBMAD7 were emplaced contemporaneously, a ~19 Ma time gap between emplacement and closure of the (U-Th)/He system is indicated by (U-Th)/He dates for sample RBMAD3. Sample RBMAD3 is from argillized quartz monzonite porphyry from near the main breccia body and the RBM fault, whereas RBMAD7 is from potassically altered quartz monzonite porphyry much further away from the main breccia body and RBM fault. Breccia bodies and/or

the RBM fault itself likely facilitated structurally controlled hydrothermal fluid flow associated with Main and/or Late-stage alteration, affecting sample RBMAD3 more than RBMAD7. Therefore, the younger age for sample RBMAD3 may represent partial resetting by later hydrothermal fluids, which did not affect RBMAD7.

The two dated zircons from sample RBMAD1 have overlapping (U-Th)/He ages of 148.2 ± 6.76 and 145.39 ± 5.64 Ma. The emplacement age of quartz monzodiorite is 163.9 ± 3.3 Ma indicating a gap ranging from 5.24 to 27.45 million years between emplacement and closure of the (U-Th)/He system. Like sample RBMAD3, sample RBMAD1 is intensely argillized and proximal to ore indicating it was possibly exposed to later hydrothermal fluids that partially reset the (U-Th)/He dates.

Samples RBMAD5 and RBMAD10 had young and highly variable ages which do not statistically overlap. (U-Th)/He ages of 140.25 ± 5.5 and 90.92 ± 3.4 Ma were obtained from RBMAD5, and 139.82 ± 5.32 and 113.41 ± 4.16 Ma were obtained from RBMAD10. Both samples were strongly mineralized with sulfides as indicated by abundant pyrite in the mineral separate in RBMAD5, and abundant cubic iron oxide lined vugs in RBMAD10. Sample RBMAD10 was from a high-grade blasthole, while sample RBMAD5 was from a low-grade zone proximal to a gold-bearing breccia zone. Pyrite could not be removed from the heavy mineral separate in RBMAD5 (using nitric acid) without risking partially resetting the (U-Th)/He ages of zircons, resulting in a very low concentration of zircons. In contrast, oxidized sample RBMAD10 had very few zircons in the heavy mineral separate as a result of low zircon contents in the rock. These characteristics resulted in poor quality zircons selected for analyses, which were broken and had some internal fractures. If the crystal were broken during emplacement (e.g.

brecciation) He may have subsequently escaped along fractures through time, and resulted in the young ages. In addition, RBMAD10z2 has a high concentration of U (936 ppm). Reiners et al. (2004) report zircon crystals with high concentrations of U (>~1000 ppm) have a high probability of radiation damage. Radiation damage results in He escape and a younger age than the closure of the (U-Th)/He system. Although the U concentration is lower than the cut-off for radiation damage, its high U concentration relative to other samples, and distinctly younger age, suggest significant He loss occurred. Despite the variablity, both samples have one age that overlaps with zircons from other samples at ~145 Ma, and one age that is significantly younger than other samples.

Zircons analyzed for (U-Th)/He dating show a wide range in ages which, in many cases, show variation between zircons analyzed for a single sample that is outside of the error for the individual zircon (U-Th)/He ages (Fig. 37). Only 1 of the 5 samples dated had individual zircon (U-Th)/He ages which statistically overlapped with each other. While some characteristics of individual zircons can account for some of the variable ages, including broken crystals and radiation damage, there are likely other poorly understood characteristics not accounted for that result in ages whose geologic significance is unclear. Nevertheless, sample RBMAD7, which shows no evidence of being exposed to hydrothermal fluids responsible for either Main- or Late-stage argillic alteration, has (U-Th)/He ages which overlap with emplacement of intrusions and indicate a temporal association between potassic alteration and intrusions. Most of the dates that show evidence of exposure to hydrothermal fluids related to advanced argillic alteration range from 140-156 Ma. Six of 9 ages from this group have 2-sigma error bars

that overlap between 142 and 145 Ma, with 7 of 9 ages with 2-sigma error bars overlapping an average alteration age 145 ± 4 Ma. This group indicates either heating of samples by hydrothermal fluids at approximately 145 Ma, or heating of samples after 145 Ma that partially reset zircon (U-Th)/He ages but was not high enough temperature to completely reset (U-Th)/He ages to the age of the heating event. The presence of ~20 Ma (U-Th)/He apatite ages from sample RBMAD7 indicates that a 20 Ma or younger thermal event occurred at RBM.

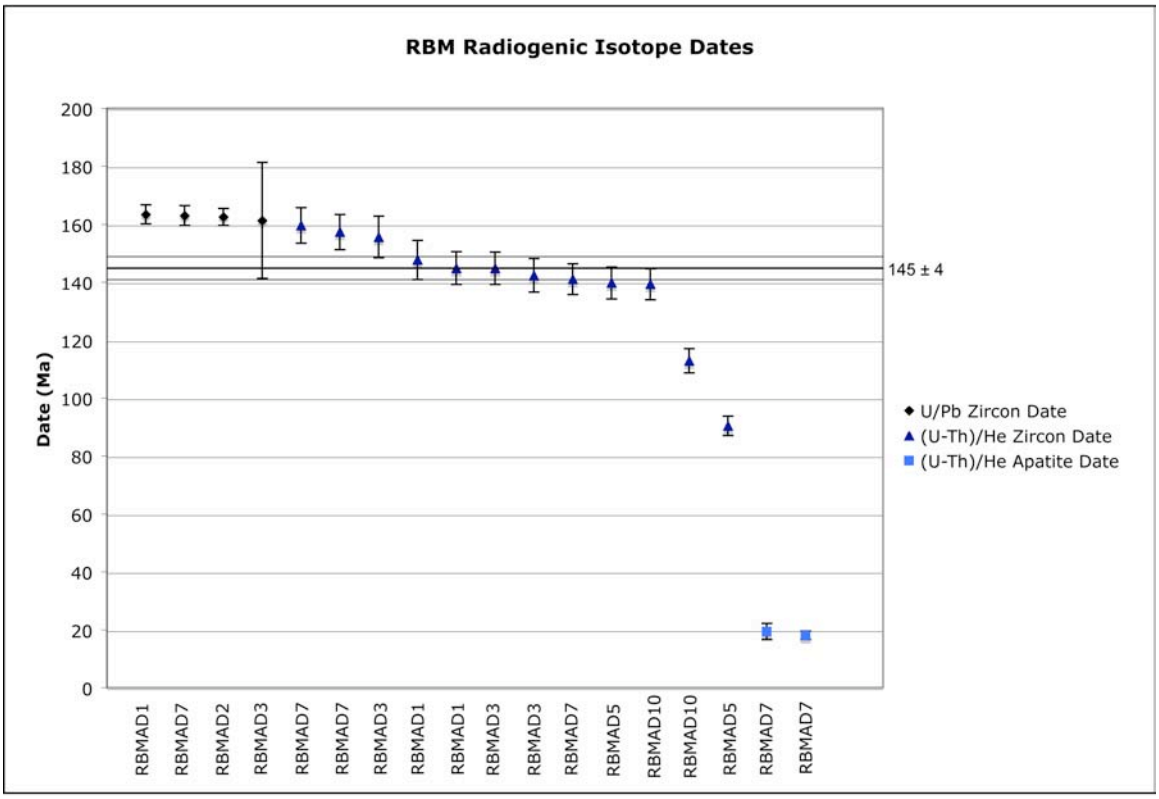

Figure 37. All zircon and apatite samples dated in this study from oldest to youngest with 2-σ error bars displayed. Note in some samples that individual dates lie outside of the 2-σ errors for other dates from the same sample. The 145 ± 4 Ma alteration age is outlined incorporating 7 of the 9 (U-Th)/He zircon ages.

Ar/Ar

The preferred age of the phlogopite and skarn formation is a weighted mean $^{40}Ar/^{39}Ar$ age of 163.3 ± 1.3 Ma based on the last five steps of the step-heating (weighted mean and error is calculated based on Taylor, 1982). These last five steps have overlapping 2-σ uncertainties and account for 34% of ^{39}Ar released (Fig. 38). This weighted mean age does not fit the criteria of a reliable plateau age, defined as a series of three or more steps releasing >50% of total ^{39}Ar released with overlapping $^{40}Ar/^{39}Ar$ ages using 2-σ uncertainties (Lanphere and Dalrymple, 1978). The series of 6 intermediate steps in the step-heating that do not statistically overlap and are older than emplacement of intrusions based on U/Pb analyses of the intrusive phases responsible for skarn formation (Table 7) likely because of excess argon.

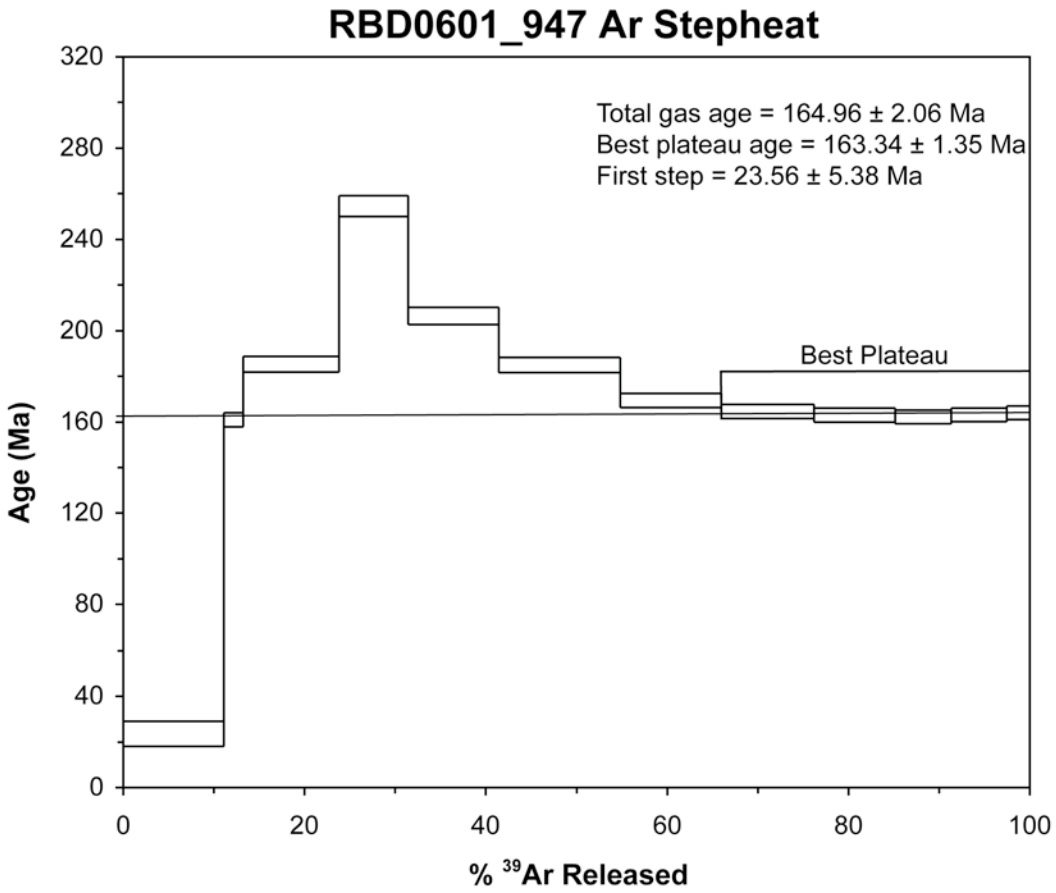

Figure 38. $^{40}Ar/^{39}Ar$ step-heat plot. No plateau age was defined. Best plateau age is defined based on a weighted mean of the last 5 steps which have overlapping 2-σ error values and account for 34% of total Ar released. This age is considered the best estimate for the age of skarn mineralization and is in agreement with the U/Pb emplacement age for the nearby intrusions. The first step released 11% of total Ar and is consistent with the (U-Th)/He apatite ages which suggest a low-temperature Miocene event.

The age of 163.3 ± 1.3 Ma is consistent with U/Pb ages on zircon and demonstrate skarn formation is closely tied in time and space with the emplacement of intrusions at RBM, suggesting the intrusive system cooled rapidly to below the closure temperature of $^{40}Ar/^{39}Ar$ for phlogopite. Given the rapid cooling rate (>100ºC/myr) for the sample as indicated by the indistinguishable $^{40}Ar/^{39}Ar$ and U/Pb ages and the low Fe content and coarse grain size of phlogopite, the closure temperature for Ar for this sample is likely around 345ºC (Harrison et al., 1985).

The lowest-temperature step yielded a $^{40}Ar/^{39}Ar$ age of 23.56 ± 5.38 Ma, which overlaps with the 19.96 ± 5.64 and 18.56 ± 2.92 Ma (U-Th)/He apatite ages from RBMAD7. This is consistent with a Miocene thermal event that resulted in partial loss of argon from cleavage planes and crystal surfaces.

Review of plausible thermal histories

All intrusive phases identified in this study were emplaced ~164 – 161 Ma based on U/Pb dating of zircons. Although these ages are slightly older than the ages obtains by Mortensen using ID-TIMS, the difference is most likely a result of discrepancies between dating techniques as opposed to an older intrusive suite. A MSWD $^{40}Ar/^{39}Ar$ age of 163.3 ± 1.3 Ma on phlogopite from skarn mineralization indicates that the Jurassic system cooled rapidly through closure temperature of the phlogopite (~345°C). Rapid cooling of the porphyry system is consistent with the shallow depth of emplacement (<~3km) as indicated by the fine groundmass identified in porphyries in the RBM pit, presence of finely-milled breccia dikes indicative of a brittle regime, and fluid inclusion characteristics identified by Nutt and Hofstra (2007).

Following emplacement of the porphyry system, and cooling to ~345°C, (U-Th)/He dates provide evidence for a younger thermal event than the emplacement age of the intrusions. Despite the variability of ages between individual analyzed zircons , the young (U-Th)/He dates could be the result of exhumation, a later hydrothermal event which partially reset (U-Th)/He dates, or, as mentioned above, poorly understoond characterisitics of the zircon crystals that are not accounted for. Seven of the 12 (U-Th)/He zircon dates statistically overlap between 142 and 145 Ma, which could be the

age at which the zircons were exhumed to a depth suitable to allow them to cool through their closure temperature. Assuming a minimum closure temperature of 150°C for the (U-Th)/He zircon system, and a high geothermal gradient of 30°C/km, the deposit would have to be emplaced at >5 km depth. This depth is unlikely considering the geologic characteristics of the porphyry system as described above. In addition, the ~159 Ma (U-Th)/He dates for sample RBMAD7 should be contemporaneous with other samples collected in the area if all (U-Th)/He dates indicate an uplift age. The older (U-Th)/He ages for RBMAD7 could be representative of a shallower depth of emplacement than other samples if they are separated by a fault with a large amount of offset, but there is no evidence for such a structure.

The 70 Ma spread in (U-Th)/He zircon ages may represent partial resetting by a later thermal event. There are no published studies that have shown consistent and complete resetting of (U-Th)/He zircons by hydrothermal systems. For example, Arehart and Donelick (2006) showed highly variable and inconsistent (U-Th)/He zircon dates, with (U-Th)/He zircon dates in some samples that were younger than the apatite fission track dates (AFT) for the same samples. The (U-Th)/He system has a higher closure temperature than the AFT system, indicating a problem with these data (Reiners, 2005). Hickey et al. (2007) found that mineralized samples from the Betze pit, another Carlin-type system, had apatite fission track dates that were reset but did not have (U-Th)/He zircon dates that were reset. Even samples from high-temperature potassic alteration zones related to porphyry-type copper deposits do not show complete and consistent resetting of zircon (U-Th)/He dates (McInnes et al., 2005). The data presented here are important in that they show variability of zircon dates from individual samples suggesting

a potential flaw in the (U-Th)/He dating technique. The inconsistency in dates obtained in this study indicate hydrothermal resetting in zircons is not well understood and requires further testing by dating many zircon grains from the same sample to better document the variation and develop testable hypotheses to explain the variation.

Despite the uncertainties in (U-Th)/He zircon dates, the (U-Th)/He apatite dates (~19-20 Ma), and the first step in the $^{40}Ar/^{39}Ar$ step-heating analysis (~23-24 Ma), strongly suggest a Miocene cooling event occurred in the Bald Mountain mining district that was likely related to a hydrothermal event. Given the constraints from the Reiners et al. (2004) experiments (Fig. 35), the partially reset and non-reset (U-Th)/He zircon dates from RBM suggest the event did not reach temperatures above ~170°C, not withstanding the incomplete understanding of hydrothermal resetting. In exhumation studies, rocks are heated to elevated temperatures for a much longer time period than hydrothermal systems in which structurally controlled hydrothermal fluids are present for a very short time. The duration of hydrothermal systems is very difficult to define. In porphyry deposits, U/Pb dating of multiple intrusions within intrusive complexes has identified the overall duration of magmatic activity associated with an intrusive complex is less than 5 myr (Campbell et al., 2006). The duration of hydrothermal fluid flow of individual porphyry's is generally much shorter, and not resolvable with modern dating techniques; however, best estimates indicate 100,000 to 300,000 years of hydrothermal activity (Marsh et al., 1997). Epithermal deposits also can form from short-duration events, lasting 50,000 to 100,000 years (approaching the limit of resolution of $^{40}Ar/^{39}Ar$ dating), based on dating of pre-mineralization rocks, mineralization, and post-mineralization rocks (Henry et al., 1997). Longer-duration hydrothermal systems have been identified

related to batholith-sized intrusion (Fournier, 1989), however these require multiple intrusive events that prolong the duration of hydrothermal activity (Marsh et al., 1997). Carlin-type deposits are likely short-duration events, although the duration is still not well understood and cannot be easily defined based on U/Pb or $^{40}Ar/^{39}Ar$ geochronology due to the general lack of associated intrusions and datable material. The best constraints available, based on AFT and (U-Th)/He dating, indicate that the overall duration of hydrothermal systems related to Carlin-type deposits is 10,000 to 1,000,000 yrs (Hickey et al., 2007).

Thermal Modeling

The dates obtained from this study complement AFT dates obtained by Schmauder (2005) from the north part of the Bald Mountain mining district. Of the 44 samples collected by Schmauder (2005), 29 were from areas of known mineralization, including three from the RBM deposit, and 15 were from areas away from known mineralization. AFT ages are derived from counting and measuring fission tracks, or damaged areas in a crystal that result from the release of charged particles during decay of trace amounts of ^{238}U incorporated in an apatite crystal (cf. Donelick et al., 2005). Damaged areas are annealed when the crystal is heated above the closing temperature of the AFT system (100-150ºC) and, similar to (U-Th)/He dating, may be partially annealed at lower temperatures (cf. Donelick et al., 2005). AFT ages published in Schmauder (2005) and Schmauder et al. (2005) were calculated using AFTsolve, a modeling program that can be used to derive the thermal history of a sample based on apatite fission tracks (Ketcham et al., 2000).

Schmauder et al. (2005) argued that AFT ages indicate a Miocene age Carlin-type mineralization at Bald Mountain. Schmauder et al. (2005) grouped 42 AFT dates into three groups: 61->120 Ma ages (19 samples), 34-51 Ma (6 samples), and 11-29 Ma (17 samples). Schmuader et al. (2005) identified a spatial correlation between the 11-29 Ma samples and the gold deposits at Bald Mountain. These young ages, as well as samples yielding 34-51 Ma ages, were clustered along the Bida trend. The older ages generally flank the younger ages, and are found distally from mineralization; although in some cases old ages are found <100 m from young ages. In the RBM deposit, three AFT samples resulted in ages of 33.8 ± 2.8, 60.0 ± 15.6, and 125.0 ± 9.4 Ma. Young ages were in close proximity to old ages, and were not separated by identified faults with major displacement, leading Schmauder et al. (2005) to conclude that the young ages resulted from hydrothermal heating rather than exhumation. The young ages in the district also correlate with light $\delta^{18}O$ values (<20‰) of whole rock carbonate., and together were interpreted by Schmauder et al. (2005) to represent Miocene hydrothermal fluid flow along the Bida trend that was responsible for Carlin-type mineralization in the district.

The HeFTy computer modeling program used in this study allows the user to simultaneously model (U-Th)/He zircon, (U-Th)/He apatite, and AFT data from a single sample to define its thermal history (Ketcham, 2005; Ketcham, 2008). The program randomly generates thermal profiles through a specified age range, and then checks the likelihood that the generated thermal profile would result in the data input for each thermochronometer. Only one input value can be used for each thermochronometer, and each input value is given a goodness of fit (GOF) value from 0 (impossible) to 1 (very

likely). The program then stores all acceptable thermal profiles (GOF of >0.05 for each input value) and good thermal profiles (GOF >0.5 for each input value), and returns them at the end of the modeling session. The program also displays the thermal profile that has the highest overall GOF value, along with the GOF for each input value in the selected thermal profile.

To compensate for the variation in ages between zircon crystals, average ages were used. For zircon (U-Th)/He inputs, an age of 145 Ma was used based on the mean of eight zircon crystals from samples RBMAD1, RBMAD3, RBMAD5, RBMAD7, and RBMAD10, all of which had overlapping ages when 2-sigma errors were considered. An error value of 4 Ma was used in order to overlap with the youngest and oldest zircon (U-Th)/He ages used in the mean calculation. The apatite (U-Th)/He dates were also averaged, and a value of 19.26 ± 3.52 Ma was used. Individual ages were also used in thermal modeling, but the resulting models were considered less relevant. Old (U-Th)/He ages >160 Ma may reflect cooling of the porphyry system and do not indicate subsequent thermal events. Alternatively, the young ages (e.g., 90.92 Ma and 113.41 Ma) are likely erroneous ages based on poor quality zircons. The older AFT ages (e.g., 125 Ma) published by Schmauder (2005) can be modeled by the same age event as the younger AFT ages (e.g., 34 Ma) but require that the event heated the samples that yielded the older ages to a lower temperature, or for a shorter duration, than the samples that yielded the younger ages. Therefore, the youngest AFT age obtained near RBM (34 Ma) was used to identify the maximum temperature reached by an Eocene and/or Miocene hydrothermal event. The raw AFT data were provided by Donnelick and Schmauder (2004), and was used in HeFTy modeling.

The program does not take into account the geologic framework of the samples, and is therefore biased toward gradual unidirectional cooling models as opposed to models that include multiple hydrothermal events. The best way for the model to account for a 145 Ma (U-Th)/He age for zircon, a 34 Ma AFT age, and a 20 Ma (U-Th)/He age for apatite is a roughly straight line that shows slow cooling through all of these points. This type of long-term cooling history could only result from deep burial and exhumation resulting in successive closure of the thermochronometers, an unlikely model based on the shallow nature of the RBM deposit and wide range of AFT and (U-Th)/He ages as described above. In order to better constrain the model to the geologic framework of a given area, age constraints can be set to require every thermal profile to pass through a user-specified temperature range within a certain age range. Following the modeling session, the user can also specify thermal profiles that may be more geologically reasonable, and the program will define a GOF for each input parameter. In this way each model can be customized to define the most geologically reasonable thermal profile.

Constraint Code	Geologic Reasoning	Age Range (Ma)	Temperature Range (ºC)
A.	Crystallization of porphyry system and rapid cooling to below phlogopite closure temperature	163	500
B.	Cooling of porphyry system to near-surface conditions (<3 km)	152-160	20-90
C.	Near-surface exposure	40-50	15-90
D.	Surface exposure as indicated by nearby tuffs	30-36	15-30
E.	Continued surface exposure	20-25	15-30
F.	Continued surface exposure	15-10	15-30
G.	Possibility of an Eocene and/or Miocene hydrothermal event	15-40	70-250
H.	Eocene hydrothermal event temporally related to Carlin-type mineralization elsewhere in Nevada	36-42	70-250
I.	Miocene hydrothermal event as indicated by cluster of AFT dates and (U-Th)/He apatite dates	17-23	70-250

Table 8. Time-temperature constraints used for HeFTy thermal modeling and the geologic evidence behind each constraint.

A series of nine age constraints were used to calculate thermal profiles for the RBM deposit (Table 8). Constraint A is based on the U/Pb emplacement ages for intrusive rocks dated in this study and the $^{40}Ar/^{39}Ar$ phlogopite age for skarn mineralization which indicate rapid cooling of the porphyry system. Constraint B represents cooling of the porphyry system to a background temperature at ~3 km depth which, based on a maximum geothermal gradient of ~30°C/km, results in a maximum temperature of 90°C. Constraint D is based on exhumation of the deposit to near-surface conditions in time for the eruption of the ~35 Ma crystal tuffs that were dated south of the RBM pit (Nutt and Hart, 2004). Constraints C, E, and F were used to force the model to cool to near-surface conditions between modeled thermal events in order to inhibit long

duration (>10 Ma) heating at elevated temperatures. Constraints G, H, and I were used in some, but not all models, to test for the potential of an Eocene and/or Miocene thermal event capable of producing the input ages for each model. HeFTy thermal modeling assumes all of the dates entered are from the same sample, and have been affected by the same temperature thermal events. Because the AFT dates were obtained from different samples than the (U-Th)/He dates, the thermal model erroneously assumes that all input parameters were heated to the same temperature for the same duration, thus adding uncertainty to the results.

Thermal profiles require a Miocene event in order to account for the Miocene (U-Th)/He apatite ages; however, they do not exclude an Eocene hydrothermal event. When constraint G is used to allow either an Eocene or a Miocene event, the resulting thermal profiles are geologically unreasonable (Fig. 39). They require a thermal event at ~38 Ma, which heats the rocks to ~170°C, then cools slowly to ~70°C at ~19 Ma. As mentioned above, thermochronology on Carlin-type, epithermal, and porphyry deposits indicates they are short-lived, and do not last for >10 Ma. When constraints D, E, F, H, and I are used to force cooling between a possible Eocene event and the Miocene event, a geologically reasonable model is defined (Fig. 40). While the thermal model still requires relatively long duration thermal events (8 myr Eocene event and ~10 myr Miocene event), a user manipulated thermal profile which depicts a ~3 myr Eocene event heating the sample to 180°C, followed by a Miocene thermal event heating the sample to 115°C for 4 myr results in an acceptable model which could produce ~145 Ma (U-Th)/He zircon ages, the 34 Ma AFT age from Schmauder (2005), and the 19 Ma (U-Th)/He apatite ages.

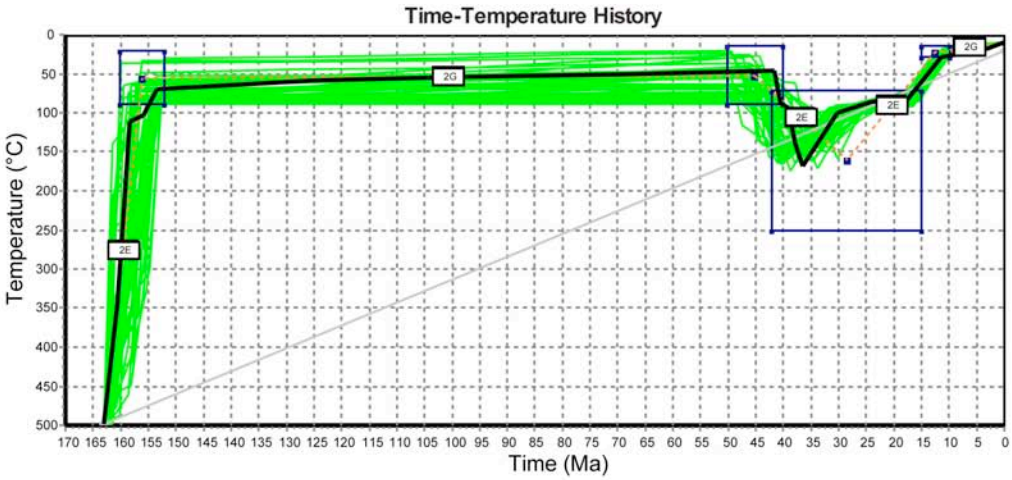

Figure 39. HeFTy model of a potential Eocene and/or Miocene event run with input parameters 145 ± 4 Ma (U-Th)/He zircon age, 34 Ma AFT, and 19.26 ± 3.52 Ma (U-Th)/He apatite age run for 200,000 iterations with constraints A, B, C, F, and G. The AFT age listed reflects the age published by Schmauder (2005). Labels 2E vs 2G identify gradual vs. episodic cooling. This model resulted in 45 acceptable models (green), the best of which had a 0.71 (U-Th)/He zircon GOF, a 0.14 (U-Th)/He apatite GOF, a 0.38 AFT age GOF, and a 0.14 AFT length GOF (outlined in black bold). All acceptable models remain at elevated temperatures for ~25 Ma, which is highly unlikely.

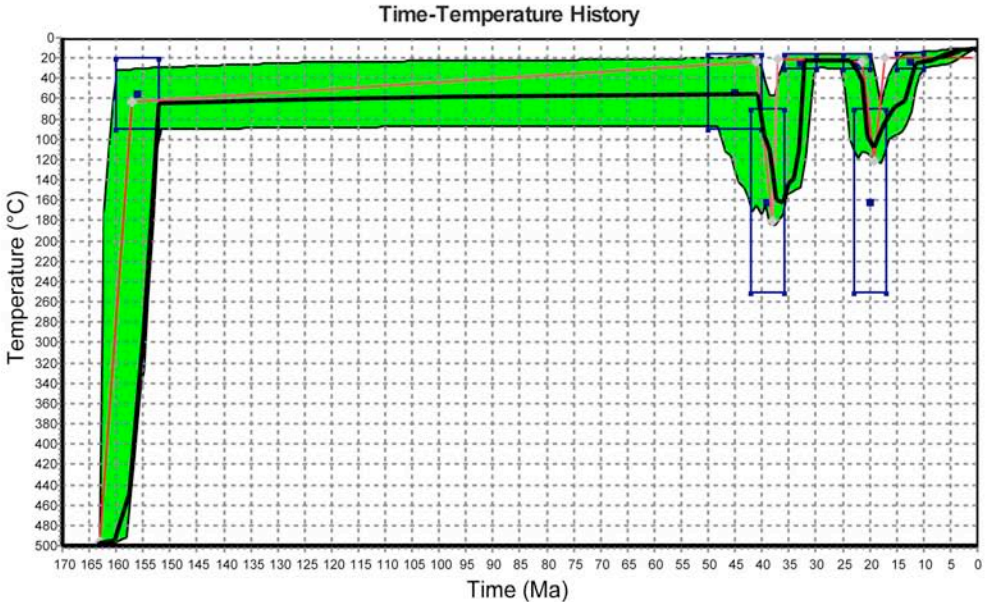

Figure 40. HeFTy model for an Eocene and a Miocene event with input parameters 145 ± 4 Ma (U-Th)/He zircon age, 19.26 +/- 3.52 (U-Th)/He apatite age, and 34 Ma AFT age from Schmauder (2005), run for 50,000 iterations using constraints A, B, C, D, E, F, H, and I resulting in 152 acceptable paths (green). The best fitting model in black bold has a (U-Th)/He zircon GOF of 0.26, A (U-Th)/He apatite GOF of 0.28, an AFT age GOF of 0.36, and an AFT length GOF of 0.22. Drawn in red is a manual manipulated model used to shorten the duration of the hydrothermal events. It has a (U-Th)/He zircon GOF of 0.93, a (U-Th)/He apatite GOF of 0.77, an AFT age GOF of 0.07, and an AFT length GOF of 0.08.

The ages can be also modeled as a single Miocene event using HeFTy: however, no acceptable model is calculated using all three (U-Th)/He zircon, AFT, and (U-Th)/He apatite ages in the same thermal profile. Plausible, acceptable models are calculated when constraints A, B, D, E, F, and I are used to model the 145 Ma (U-Th)/He zircon age and the 19 Ma (U-Th)/He apatite age separately from the 34 Ma AFT age and the 19 Ma (U-Th)/He apatite age. The thermal profile resulting from 145 Ma (U-Th)/He zircon and 19 Ma apatite ages provides abundant good models with heating events to ~ 180°C around 20 Ma (Fig. 41A). The thermal profile which incorporates only the 34 Ma AFT age and the 19 Ma (U-Th)/He apatite age is more tightly constrained, but does provide acceptable models heating to ~120ºC, ~22 Ma (Fig. 41B). When the acceptable thermal profiles for AFT and (U-Th)/He apatite ages are overlain on the (U-Th)/He apatite and (U-Th)/He zircon model, the (U-Th)/He apatite and (U-Th)/He zircon model requires heating ~50°C hotter than the AFT data indicate. It is likely that the AFT sample was not heated to as high of temperatures as the (U-Th)/He zircon samples that were collected adjacent to breccia zones and the RBM fault, which likely served as fluid conduits for Miocene hydrothermal fluids. Therefore, a Miocene event alone could produce the radiogenic ages presented in this and previous studies, provided that it was strongly structurally controlled, and was not a regional heating event.

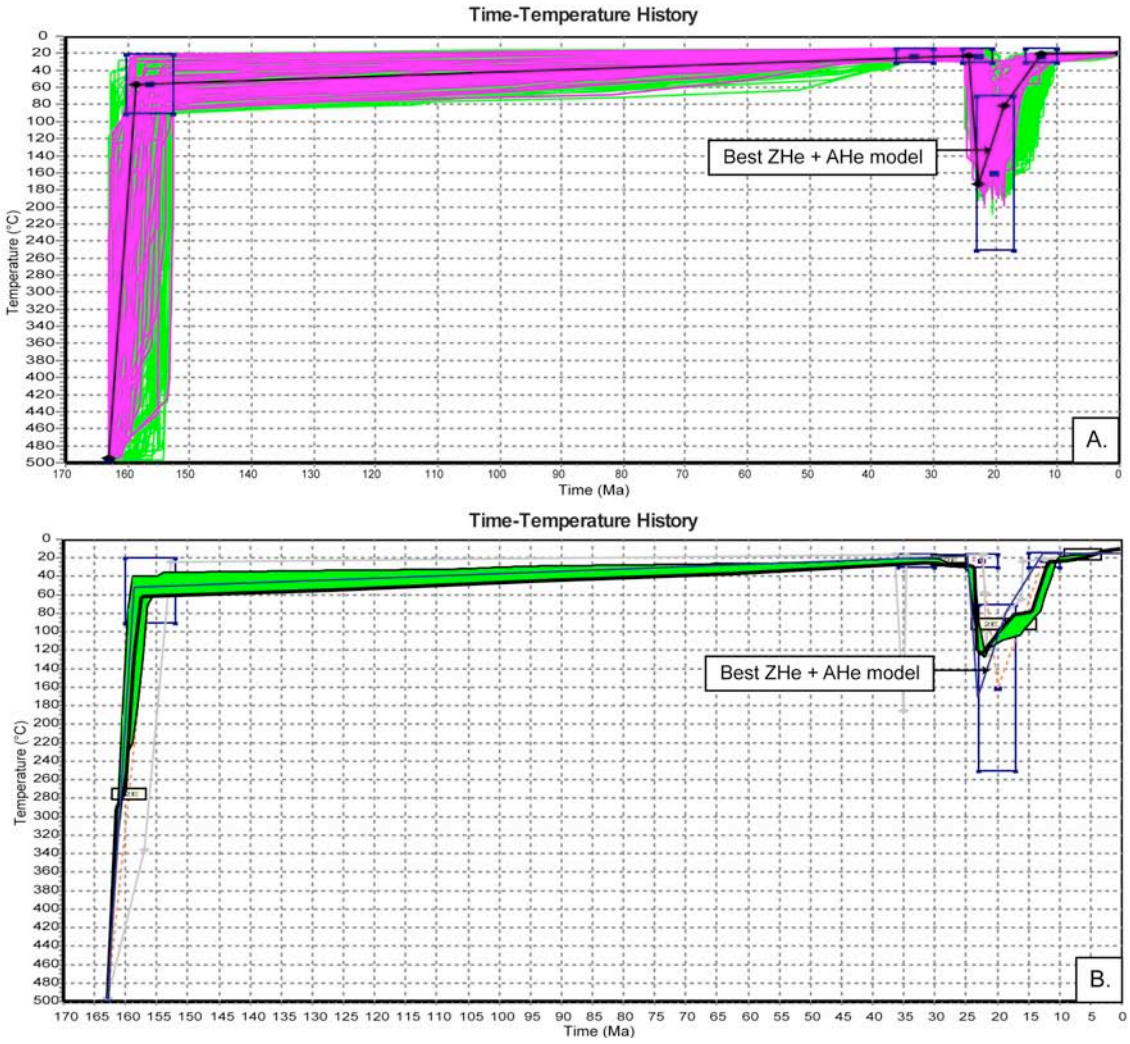

Figure 41A. Model with input parameters 145 ± 4 Ma (U-Th)/He zircon age and 19.26 ± 3.52 (U-Th)/He apatite age run for 2,000 iterations resulting in 216 acceptable paths (green) and 47 good paths (magenta). Geologically reasonable model (black) outlined to show similar thermal event to the one indicated by B and resulting in a 0.99 (U-Th)/He zircon GOF and a 0.63 (U-Th)/He apatite GOF. B. Model with input parameters BM-16 (34 Ma) from Schmauder (2005) and 19.26 ± 3.52 (U-Th)/He apatite age, run for 200,000 iterations resulting in 3 acceptable hits (green). Best hit (black) resulted in 0.56 AFT age GOF, 0.07 AFT length GOF, and 0.21 (U-Th)/He apatite GOF. Constraints A, B, D, E, and F used for background, and I used to force a Miocene event. Blue line added to B to show the most likely thermal event for both A and B. Note that the same age thermal event could result in ~145 Ma (U-Th)/He zircon, ~34 Ma AFT, and ~19 Ma (U-Th)/He apatite ages if the (U-Th)/He zircon samples were heated to 172°C while the AFT sample was only heated to 124°C.

VIII. Discussion

1. Lack of evidence for Eocene-aged Carlin-type mineralization at RBM

Characteristics of Bald Mountain, including its geographic position along the southern extension of the Carlin trend and presence of arsenian pyrite and marcasite which texturally resemble Carlin-type deposits, as well as the lack of other known Jurassic gold deposits in Nevada, offer the possibility that gold mineralization at Bald Mountain may be related to Eocene-aged hydrothermal activity as documented for other Carlin-type gold deposits in Nevada. Like the mineralization in the northern part of the Bald Mountain district, Carlin-type gold mineralization is commonly spatially associated with Mesozoic plutons (Cline et al., 2005; Ressel and Henry, 2006). Carlin-type deposits may be spatially associated with Mesozoic plutons because the intrusions indicate deep-crustal structural conduits, and the margins of intrusions are often densely fractured, resulting in zones of enhanced permeability (Heitt et al., 2003; Cline et al., 2005). Some gold is temporally associated with the Mesozoic intrusion (e.g. Goldstrike, Emsbo et al., 2000), but it is vein-style mineralization associated with sericitic alteration and is volumetrically insignificant compared with the overprinting Eocene-aged Carlin-style mineralization.

(U-Th)/He zircon ages presented in this study allow for the presence of a second hydrothermal system less than ~145 Ma at RBM, which may have overprinted Jurassic porphyry-style mineralization. Although (U-Th)/He zircon ages vary widely between zircons from individual samples, all ages are younger than the emplacement age of plutons defined by U/Pb dating, indicating (U-Th)/He zircon ages may be partially reset

by a later hydrothermal event. It is possible that an Eocene aged thermal event related to Carlin-type fluids could result in the partially reset (U-Th)/He zircon ages at RBM, as suggested by Arehart and Donelick (2006) in their thermochronology study of the Pipeline Carlin-type gold deposit. A thermal event, which reached temperatures of ~180°C for ~3 my, could partially reset (U-Th)/He zircon ages based on the HeFTy modeling outlined above. Although 3 my is a relatively long-lived hydrothermal event, shorter thermal events become very difficult to model with HeFTy. At Bald Mountain a second, lower temperature, Miocene event is required to reset (U-Th)/He apatite ages, and partially reset AFT ages, but does not preclude the presence of an Eocene thermal event.

An Eocene-aged Carlin-type system could be responsible for the Late-stage mineralization at RBM. Gold in the Deep Star Carlin-type deposit in the northern Carlin trend is hosted within a breccia body which contains local fluid streaming textures, grades outward into crackle breccias, and is cemented by quartz + kaolinite + marcasite, similar to the magmatic-hydrothermal breccias at RBM (Heitt et al., 2003). It is difficult to disprove the RBM breccia bodies are Eocene in age and related to Carlin-type mineralization, rather than the the Jurassic intrusive system. This could explain the relationship between gold mineralization and brecciation as opposed to a specific phase in the Jurassic intrusive system. It does not, however, explain the spatial association between breccia bodies and quartz monzodiorite dikes, the similar orientation of breccia bodies and Jurassic intrusions, or the syn- to post-breccia mafic dikes at RBM. Alternatively, the breccia bodies could be Jurassic magmatic-hydrothermal breccias as interpreted in this study, which later served as zones of favorable permeability during

Eocene hydrothermal activity. It is likely that later fluids would have also taken advantage of other faults and fractures that are unrelated to and postdate the breccia bodies. Such relationships have not been observed at RBM.

Breccia lenses, as opposed to favorable stratigraphic horizons, are the main control on gold mineralization at RBM. In contrast, Carlin-type deposits in the southern portion of the Bald Mountain mining district, as well as elsewhere in Nevada, are commonly stratigraphically controlled (Cline et al., 2005; Ilchik, 1990; Nutt and Hofstra, 2003). At RBM, ore occurs in breccia bodies where they cut the lower Paleozoic carbonates and where they cut the Mississippian Chainman Shale, a stratigraphic unit not mineralized elsewhere in the district. Breccias also host ore in some of the south district deposits at Bald Mountain, but are concordant with stratigraphy, occurring in the basal Pilot shale and the uppermost Guilmette limestones. Furthermore, the diorite porphyry dikes at RBM, have a high iron contents that would have facilitated gold deposition through sulfidation, similar to ore-bearing lamprophyre dikes in the Carlin trend (Bettles, 2002). However, they are unmineralized, are only propylitically altered, and cross-cut advanced argillic alteration at RBM. Nevertheless, it is possible that a tectonic or alteration event that pre-dated diorite porphyry intrusions resulted in ground preparation making other rock types more favorable hosts for a second post-Jurassic mineralization event.

At Deep Star, and most other Carlin-type deposits, Au is associated with As, Hg, Sb, Tl, ± W, ± Ag, ± Zn (Heitt et al., 2003; Arehart, 1996; Hofstra and Cline, 2000; Cline et al., 2005). A second elemental association of Pb, Bi, Cu, Mo, U, and V is present near the Deep Star orebody in the Little Boulder Basin stock but the relationship to gold is

unclear (Heitt et al., 2003). At Goldstrike, quartz veins with high Pb, Cu, Zn, As, Ag, Sb, Bi, and Te are present, and have been convincingly linked to the Jurassic Goldstrike stock and unrelated to the Carlin-type element suite (Emsbo et al., 2000). In contrast, gold mineralization at Jerritt Canyon, which is not spatially related to Mesozoic intrusion, is associated with As, Hg, Te, Tl, ± Sb (Patterson, 2009), and not associated with Bi or base metal mineralization. Au at RBM is associated with Sn, Bi, In ± Te, more closely resembling the geochemical signature of the Jurassic Goldstrike veins rather than an overprinting Carlin-type mineralization event. A separate As + Sb ± Tl ± Hg association is also present, and may be related to Late-stage mineralization, but is not associated with gold, supporting the interpretation that most of the gold at RBM was not deposited by Carlin-type ore fluids.

Arsenic-rich rims, which host most of the gold in Carlin-type deposits, do not appear to host gold at RBM. Ore stage pyrite in Carlin-type deposits, which texturally resembles Late-stage pyrite and marcasite at RBM, occurs as fine-grained "sooty pyrite" and forms rims on earlier pyrites (Wells and Mullins, 1973; Arehart et al., 1993; Cline et al., 1997). Ore-stage pyrite and marcasite from Carlin-type deposits, including Meikle (Emsbo, 1999), Betze-Post (Henkelman, 2000), and Turquoise Ridge (Cline et al., 2008) have been analyzed under a microprobe, and show a common elevated suite of elements that includes Au, As, Hg, Sb, Tl ± Te ± Cu. Nutt and Hofstra (2003) analyzed ore-stage pyrite from the Winrock Carlin-type deposit in the southern portion of the Bald Mountain mining district, and found that, like at other Carlin-type deposits, gold-bearing rims were elevated in As, Tl, Hg, and Sb. This elemental suite was analyzed for at RBM and, while some Late-stage pyrite and marcasite did contain elevated concentrations of As and Sb,

none of the twenty-one Late-stage pyrite and marcasite analyses run in this study identified gold above detection limit (~47 ppm). If gold is present in the Late-stage pyrite and marcasite at RBM, it is in considerably lower concentrations than have been identified in other Carlin-type deposits. In addition, all of the above studies have identified elevated Hg (generally >1,000 ppm), while only two pyrites analyzed in this study had elevated Hg (170 and 180 ppm). Unlike most Carlin-type deposits, free gold is present in kaolinite + pyrite cemented breccias unrelated to arsenian rims. Arsenopyrite is present in some high-grade samples associated with Main-stage mineralization, and is likely the source of the weak As-Au correlation at RBM, but records a higher temperature phase than Late-stage arsenian pyrite and marcasite, and is not generally associated with Carlin-type deposits. These characteristics support the interpretation by Nutt and Hofstra (2007) that Late-stage arsenian pyrite and marcasite did not mobilize significant gold at RBM.

While a second thermal event is indicated at RBM by partially reset (U-Th)/He zircon, AFT, and (U-Th)/He apatite dates, as well as the first $^{40}Ar/^{39}Ar$ step of the phlogopite date, they point to a Miocene hydrothermal event rather than an Eocene event (Schmauder 2005; this study). No thermochronometric data obtained in this or previous studies of the RBM deposit indicate hydrothermal fluid flow contemporaneous with neither the 42-36 Ma age defined for other Carlin-type deposits in Nevada (Hofstra and Cline, 2000; Arehart et al., 2003; Cline et al. 2005), nor the late Eocene volcanics present near RBM (Nutt and Hart, 2004; Mortensen et al., 2000).

2. Possibility of Miocene Mineralization

Miocene deposits have been identified elsewhere in Nevada and have produced greater than 40 million ounces of gold (Long et al., 1998). The closest early to middle Miocene gold deposits near Bald Mountain are a group of low-sulfidation epithermal deposits associated with bimodal volcanism that began approximately 16.5 Ma, and are tectonically related to continental rifting during Basin and Range extension (Noble, 1988; Christiansen and Yeats, 1992; John, 2001). These gold deposits are localized along a northwest-trending linear magnetic anomaly known as the Northern Nevada Rift, ~50 km west of Bald Mountain (Maybe, 1966; Zoback and Thompson, 1978). They are strongly structurally controlled, characterized by thin alteration zones with adularia-silica alteration, low base metal contents, and abundant silver-selenide minerals (John, 2001; John et al., 2003; Leavitt et al., 2004). While low-temperature thermochronometers indicate the potential for a hydrothermal event that may temporally overlap with these deposits, the lack of Miocene volcanic rocks, the widely distributed advanced argillic alteration assemblage, and the high base-metal content at RBM clearly distinguishes it from this group of deposits.

The two other Miocene ore deposit types that have been recognized in Nevada are high-sulfidation and intermediate epithermal deposits associated with western andesite assemblage volcanism, (John, 2001; Simmons et al., 2005). High sulfidation deposits are characterized by advanced argillic alteration assemblages, extensive alteration haloes, and high base-metal contents (John, 2001). While these characteristics are similar to RBM, the close spatial and temporal relationship between ore deposits and arc-related

magmatism, is absent, as Miocene arc-related volcanism is ~300km west of RBM (John, 2001).

If a Miocene thermal event at RBM did deposit gold, the mineralization is not spatially associated with recognizable Miocene magmatism. Rather than the Carlin-type deposits at Alligator Ridge, Yankee, and the Mooney Basin in the southern and eastern parts of the Bald Mountain district being Eocene, they, alternatively could be Miocene in age. Carlin-type deposits are inherently difficult to date (Hofstra and Cline, 2000; Arehart et al., 2003), and none of the deposits in the southern portion of the Bald Mountain mining district have been convincingly dated. Based on a ~35 Ma poorly to moderately consolidated tuff overlying silicified rocks near the Vantage deposit, Nutt and Hofstra (2003) interpreted mineralization at Alligator Ridge to be older than 35 Ma. The tuff contains smectite, but is interpreted as post-mineral based on a lack of silicification, sulfides, or anomalous concentrations of trace elements (Nutt and Hofstra, 2003). Ilchik (1990) dated seven alunite samples from the Vantage deposit by K-Ar. The alunite is most likely supergene in origin (Arehart et al., 1992), and the K-Ar dates, which range from 12.4 to 3.6 Ma, provide a minimum age of mineralization. Ilchik also identified offset of the ~35 Ma tuffs along the Vantage fault, which he interpreted to pre-date mineralization. Although these constraints are rather ambiguous, there is no unambiguous evidence that disproves the possibility for ~20 Ma Carlin-type mineralization in the southern part of the district and elsewhere in the district, including RBM. Nevertheless, the relationship between intrusions, brecciation, and mineralization at RBM, together with the trace-element geochemical signature of gold mineralization, as

described above, are not consistent with Carlin-type mineralization in the southern part of the district or elsewhere in Nevada.

3. Jurassic gold mineralization at RBM

Geological, petrographic, mineralogical and geochemical evidence suggests that the most likely age for gold mineralization at RBM is Jurassic. The association between the Jurassic intrusive rocks and gold mineralization has been consistently identified by previous research in the district, from Hill (1916), through Hitchborn et al. (1996) to Nutt and Hofstra (2007). Detailed mapping and petrography in this study have greatly refined the temporal and spatial relationships between gold mineralization and Jurassic intrusions. In addition, this study highlights the importance of magmatic-hydrothermal breccias in localizing gold at RBM.

The presence of three distinct mineralization events, first recognized by Hitchborn et al. (1996) is validated by this study. Potassic alteration, first identified in this study, overprinted by sericitic alteration, and related to quartz + molybdenite ± chalcopyrite mineralization, can be definitively identified as an early alteration assemblage based on truncated veins and molybdenite books at clast boundaries in magmatic-hydrothermal breccias. Recent drilling has identified a much larger porphyry stock south of RBM, associated with potassic alteration and quartz-molybdenite veining, which further defines the relationship between molybdenum mineralization and the felsic Jurassic porphyry system.

Silicification, advanced argillic alteration, and brecciation are spatially associated with quartz monzodiorite dikes, and indicate a shift from a ductile to a brittle tectonic

regime, as the porphyry system cooled. Gold mineralization is localized in breccia lenses at RBM, and is superimposed on the pre-existing base metal phase. While it is possible that the gold mineralization event is significantly later than brecciation, factor analysis of assays, coupled with microprobe analyses, indicates gold mineralization is associated with Bi and Sn. Magmatic-hydrothermal fluids released from an underlying magma chamber, which had undergone significant fractional crystallization, would be enriched in Bi, Sn, and Au, which are incompatible in reduced intrusions (Cerny et al., 2005; Mustard et al., 2006). At RBM these fluids came off late in the evolution of the underlying magma chamber, and were responsible for Main-stage mineralization. Late mafic dikes indicate that a significant mafic-recharge event occurred, which may have been coincident with some brecciation.

Late-stage iron sulfide mineralization was identified as a late mineralization phase superimposed on gold mineralization by Hitchborn et al. (1996), and Nutt and Hofstra (2007). Nutt and Hofstra (2007) concluded that late pyrite and marcasite formed from the destruction of earlier base metal sulfide minerals, either during collapse of the Jurassic hydrothermal system, or during supergene weathering. Petrography and microprobe analyses from this study indicate that while some of the Late-stage marcasite may have formed by destruction of earlier sulfides, most of it is geochemically different from earlier phases, is present well below the oxidation front, and formed from the collapse of the Jurassic hydrothermal system rather than by supergene processes. Ankerite + pyrite veins, which appear to post-date Late-stage arsenian marcasite mineralization, mark the final collapse of the Jurassic hydrothermal system.

While these factors alone do not rule out the possibility of a Carlin-type mineralization event at RBM, the presence of ~162 Ma diorite porphyry dikes, which are nowhere altered by Early, Main-, or Late-stage mineralization, have very low gold concentrations, and cross-cut advanced argillic alteration in the RBM pit as well as strongly sulfidized quartz monzodiorite dikes with high gold values south of the RBM deposit, strongly argue that gold mineralization at RBM is Jurassic in age. The only published study which has suggested that mineralization was younger than Jurassic was by Schmauder et al. (2005), who inferred that mineralization was related to Miocene hydrothermal activity. While the (U-Th)/He zircon apatite ages from this study are consistent with a Miocene thermal event, there have been no geologic features identified or evidence put forward that suggest that it was responsible for any gold mineralization.

Classification of RBM as an Intrusion-related Gold Deposit

The characteristics of RBM, as outlined in detail in this study, are consistent with Nutt and Hoftra's (2007) conclusion that RBM is a Jurassic intrusion-related (IR) gold deposit. IR gold deposits are a relatively newly defined type of ore deposit. Lang and Baker (2001) define this class of ore deposits as gold associated with:

> (1) metaluminous, subalkalic intrusions of intermediate to felsic composition that span the boundary between ilmenite and magnetite series; (2) carbonic hydrothermal fluids; (3) a metal assemblage which variably combines gold with elevated Bi, W, As, Mo, Te and/or Sb, and low concentrations of base metals; (4) a low sulfide mineral content, mostly <5 vol%, with a reduced ore mineral assemblage that typically

> comprises arsenopyrite, pyrrhotite, and pyrite and which lacks magnetite or hematite; (5) areally restricted, commonly weak hydrothermal alteration, except in systems formed at the shallowest depths spanned by these deposits; (6) a tectonic setting well inboard of inferred or recognized convergent plate boundaries, where continental magmatism commonly contains coeval intrusions of alkalic, metaluminous calc-alkalic, and peraluminous compositions; and (7) a location in magmatic provinces best formerly known for tungsten and/or tin deposits.

The pervasive nature of advanced argillic alteration, high total sulfide content, and breccia-hosted nature of the RBM deposit distinguish it from other IR gold deposits. Lang et al. (2000) have documented that variation in metal content, alteration assemblage, and extent of alteration, is in large part related to the depth of formation of IR deposits. This variation is best illustrated by a comparison of deep (Timbarra), moderate depth (Kidston) and shallow (Kori Kollo) IR gold deposits as they relate to RBM (Table 9).

	RBM	Carlin-type	
		Alligator Ridge	Deep Star
Reference	This Study	Illick, 1990; Nutt and Hofstra, 2003	Heitt et al., 2003
Ore Minerals	Primarily free Au within kaolinite-quartz-marcasite-pyrite matrices of breccias and as Au inclusions in pyrite and chalcopyrite, spatially associated with bismuth-telluride minerals, with lesser Au as electrum.	Au in arsenic-rich rims on marcasite and pyrite	Au in arsenic-rich pyrite and marcasite.
Deposit Geometry	High angle breccia lense crosscutting lithologic contacts.	Stratabound deposits, locally focused along folds and faults within a brecciated stratigraphic horizon.	Pods along high-angle long lived faults and low-angle bedding parallel zones which may be structurally reactivated. Highest gold grades present in intensely fractured fault intersections.
Regional Relationship to other deposits	Intrusive suite with other Au deposits hosted in and along cogenetic intrusions. Historic production of Cu, Ag, Sb, Au, and W (Smith 1976).	40 km long north to northeast striking mineral trend	Ore localized along the Gen-Post fault system. Many other ore bodies occur both north and south of the Deep Star deposit along this fault zone.
Host Rocks	Breccia lenses cutting equigranular dikes and sills, porphyritic dikes and plugs, skarn and hornfelsed siliciclastics.	Along a stratigraphic contact between thick bedded to massive carbonates and overlying calcareous clastic units.	Brecciated calc-silicates and lesser diorites. Increasing gold grades correlate with increasing breccia matrix to clast ratios.
Relationship to Magmatism	Strong spatial association between mineralization and equigranular quartz monzodiorite dikes along the margins of a large porphyry stock Intrusions pre- and post-date mineralization.	Late Eocene volcanic rocks present in the area but are interpreted to be younger than gold deposits.	Jurassic Goldstrike stock and lamprophyre dikes pre-date mineralization. Post-ore rhyolite dikes have been dated at 38.05 ± 0.09 and 38.98 ± 0.26 Ma. Synore rhyolite dikes are mineralized with gold and appear to be roughly the same age although alteration has prohibited reliable dating.
Depth of Formation	2-3 km	< 0.3 to 0.8 km	1-2 km
Hydrothermal Alteration	Au hosted within intensely quartz-kaolinite-marcasite altered matrix of breccias.	Decalcification and silicification in ore zones.	Inner ore-stage quartz-kaolinite alteration surrounded by pre-ore quartz-dolomite and outer quartz-sericite-pyrite.
Geochemical Associations	Au correlates with Sn, Bi, In ± W ± Te	Ore zone is enriched in Si, S, As, Sb, Tl, Hg, ± Ba	Au with As, Sb, Hg, Tl, and W with a weaker association with Zn and Ag

Table 9 **Comparison of key characteristics of the RBM deposit with other known gold deposits. Included are the Alligator Ridge and Deep Star Carlin-type deposits in Nevada to contrast with shallow (Kori Kollo), deep (Timbarra), and breccia-hosted (Kidston) IR gold deposits elsewhere in the world.**

Intrusion Related			
	Kori Kollo	Timbarra	Kidston
Reference	Fitzmayer, 1999	Mustard, 2001; Mustard et al., 2006,	Baker and Andrew, 1991
Ore Minerals	Electrum with early pyrite, pyrrhotite, native bismuth, bismuthinite, and jamesonite and lesser, later, electrum with pyrite, jamesonite, bismuthinite, marcasite, Fe-rich sphalerite, tetrahedrite, bournite and chalcopyrite with lesser galena, arsenopyrite, and stannite	Free Au with muscovite, chlorite, calcite, silver-bismuth telluride, lead-bismuth telluride, and rare galena and chalcopyrite	Free gold in sheeted veins and cavities filled by quartz-ankerite ± pyrite, pyrrhotite, sphalerite, chalcopyrite, molybdenite, galena, bismuthinite, and bismuth telluride minerals
Deposit Geometry	A zone of sheeted, steeply dipping sulfide veinlets cutting intrusions (Fitzmeyer, 1999), with high grade ore in structurally controlled hydrothermal breccias (Columba and Cunningham, 1993).	Gold disseminated in a flat-lying sheet within the upper 250 m of a pluton	An inverted funnel shape around the margins of a breccia pipe
Regional Relationship to other deposits	Within a north-trending Miocene belt of polymetallic vein deposits primarily exploited for Sn and Ag.	Within a belt of leucomonzogranites which have produced Sn, W, Mo, Ag, As, Bi, Cu, Pb, Zn, Au, fluorite, beryl, and topaz ores (Blevin and Cappell 1996 cited by Mustard, 2001))	Isolated ore deposit
Host Rocks	Dacite-andesite and granodiorite at depth.	Disseminated ore locally infilling primary miarolitic cavities within leucomonzogranite or microgranite	Brecciated rhyolite and lesser gneiss and granodiorite
Relationship to Magmatism	Subvolcanic intrusion possibly related to porphyry intrusion at depth.	Au hosted within carapace of the source intrusion (Thompson et al, 1999)	Mineralization associated with intrusion breccia temporally associated with intrusion of a late rhyolite phase
Depth of Formation	0.8 to 2.5 km	5 to 10 km depth	~3.5 km
Hydrothermal Alteration	Weak to incipient silicification, locally occuring as silica flooded patches. Sericite replacing feldspars, pyrite replacing primary Fe-Mg minerals as well as sericite, with trace amounts of disseminated sphalerite, chalcopyrite, and galena. Primary apatites altered to APS minerals + alunite.	Early quartz-K-feldspar-biotite-albite alteration overprinted by muscovite-chlorite-calcite mineralization temporally related to gold mineralization.	Breccia matrix completely replaced by muscovite and quartz along sheeted veins grading outward to partial replacement of host rocks by muscovite + ankerite.
Geochemical Associations	Au with Ag, As, Sb, Sn, Bi, Cu, Zn, Pb, and W (based on Long et al., 1992 qtd by Thompson, 1999).	Au correlates strongly with Bi, Ag, and Te and weakly with As, Sb, Mo, and Sn	Au with Bi, Mo, Cu, Pb, Zn, and As and overlies a zone of W-Mo veins.

Table 9. Continued.

The Timbarra gold deposit in New South Wales is considered by Mustard (2001) to be the deep granite-hosted end member of IR deposits. At Timbarra, gold occurs in miarolitic cavities concentrated in flat lying sheets below an aplite cap on, and aplite layers within, a large composite porphyry stock (Mustard et al., 2001). A study by Mustard (2006) on melt inclusions from the deposit indicates that Au, Mo, W, Bi, As, Sb, Cu, Pb, and Zn became enriched in the carapace of the stock during fractional crystallization. Mustard hypothesizes that the pressure of exsolved metal-bearing magmatic-hydrothermal fluids in the carapace did not exceed lithostatic load due to the deep level of emplacement (5-10 km), resulting in the disseminated mineralization style within late phases of the stock, rather than formation of magmatic-hydrothermal breccias.

Kidston is a breccia-hosted Au deposit that was emplaced at a considerably shallower depth than Timbarra. At Kidston, three phases of breccia are identified, with a phase 1 tourmaline-cemented breccia body, followed by a phase 2 collapse breccia, and a phase 3 hydrothermal intrusive breccia (Baker and Andrew, 1991). Stockwork quartz-magnetite-pyrite and stockwork quartz-molybdenite-pyrite ± arsenopyrite ± chalcopyrite mineralization is spatially and temporally associated with rhyolite intrusions that are cut by phase 3 brecciation. Gold occurs as free grains and as inclusions in pyrite, arsenopyrite, and bismuth tellurides associated with quartz + ankerite ± pyrite ± pyrrhotite alteration, which is concentrated in an inverted funnel-shaped zone around the margins of the the phase 3 hydrothemal breccia. The breccia pipe is cut by rhyolite dikes, and the pipe and mineralization are cut by andesite dikes. Baker and Andrew (1991) suggest the phase 3 hydrothermal breccia formed by either explosive release of volatiles from the crystallizing post-breccia rhyolite or interaction of the rhyolite with fluids in the

magma chamber. Ore grade gold mineralization was the result of cooling of ascending post-breccia magmatic fluids at ~3.5 km depth.

The IR deposits of the Bolivian tin belt are a series of shallow to subvolcanic felsic domes, and represent the shallow end member of the IR gold deposits (Fitzmayer, 1999; Lang and Baker, 2001). Deposits are characterized by intensely silicified lithocaps underlain by advanced argillic alteration assemblages and up to 10% sulfides (Sillitoe et al, 1998). Kori Kollo is the best-studied deposit in the belt, where gold occurs as electrum in high-angle sulfide veins associated with early sericitic alteration followed by advanced argillic alteration. The late-stage advanced argillic alteration, characterized by alunite, APS minerals, and marcasite distinguishes Kori Kollo from most other IR deposits (Columba and Cunningham, 1993; Fitzmayer, 1999). Fitzmayer argues that at Kori Kollo, acidic, oxidized fluids expelled from dacitic intrusions overwhelmed the buffering capacity of the host rocks, leading to the evolution of the hydrothermal system from reduced and near-neutral to oxidized and acidic fluids, resulting in late advanced argillic alteration. Korri Kollo, like RBM, has a much higher total sulfide content, with more abundant pyrite than other intrusion related deposits. Thompson et al. (1999) relate this to a shallow depth of emplacement, which allows enhanced magma degassing and sulfide precipitation.

RBM has characteristics of all of the IR deposits described above. Timbarra is a much deeper deposit than the 2-3 km depth of emplacement indicated by Nutt and Hofstra (2007) for RBM. Nevertheless, the spatial association of gold with equigranular quartz monzodiorite dikes and sills at RBM, particularly those which directly overly the main megacrystic quartz monzonite porphyry stock, indicate gold was enriched in late

phases of magmatism. The breccia-hosted character of Kidston, and temporal relationship of early Au-poor mineralization, brecciation, and late gold-rich mineralization is very similar to RBM. In addition, the description and genetic relationship of phase 3 brecciation with post-breccia intrusions at Kidston is similar to the magmatic-hydrothermal breccias at RBM. The high sulfide content and advanced argillic alteration assemblage at RBM indicate pervasive fluid flow similar to, though not as intense as, that inferred by Fitzmayer (1999) at Kori Kollo. RBM may therefore represent a hybrid deposit that formed at a depth between Kidston and Kori Kollo. In addition, the late mafic component indicated by mafic dikes at RBM is similar to the late-stage andesite identified at Kidston, and has been identified at many other IR deposits. Although their relationship to mineralization is unclear, Lang and Baker (2001) suggest that they may be important to the metallogenisis of IR deposits.

Implications for Exploration

Identification of RBM, and the other deposits in the north part of the Bald Mountain mining district, as an IR gold system has considerable implications for exploration in Nevada. Like Bald Mountain, IR deposits elsewhere generally form as a series of deposits over a relatively short time interval (Lang et al., 2000). In addition, they can form at variable depths, are associated with a wide range of host rocks, and are associated with alteration that is not extensive, making them difficult to identify (Lang et al., 2000). Considering the abundance of Jurassic intrusions in the region, the relatively new recognition of IR deposits as a distinct ore-deposit type, and the overwhelming stress

on exploration for Carlin-type gold deposits, other IR deposits are likely present in Nevada but have not yet been identified or recognized as such.

Intrusion-related gold deposits share some characteristics that can be used in exploration for new deposits. IR deposits are generally associated with the carapaces of large metaluminous to weakly peraluminous, calc-alkalic to subalkalic granitic to granodioritic intrusions that contain only minor concentrations of either magnetite or ilmenite (Lang et al., 2000). The direct source of metals from fractional crystallization of the magma chamber further constrains exploration to late crystallizing phases within an intrusive suite, focused around high-level cupola-shaped stocks within aerially extensive plutonic suites (Mustard et al., 2001). In addition, although the direct genetic relationship is unclear, the spatial association of gold deposits with a volumetrically minor mafic intrusive phase at RBM and other IR systems indicates a potentially valuable exploration feature to identify the most prospective intrusive suites. Geochemically, IR deposits can be vectored in on best by identification of Bi, and sometimes more distal As anomalies (Lang et al., 2000). Historic placer gold production and/or Sn-W mineralization is a key indicator of productive intrusive suites.

In Nevada, mineralization related to Jurassic intrusions may in some cases be misidentified as overprinting, Tertiary Carlin-type mineralization. There are Jurassic intrusions present near many Carlin-type ore deposits, including Goldstrike (Emsbo et al., 2003; Ressel and Henry, 2006) and Cortez (Elliott and Wells, 1968; McCormack and Hays, 2004). While most of the gold deposits identified in these districts are Eocene in age, it is possible that significant Jurassic mineralization is present but has not yet been identified. In particular, the presence of auriferous quartz-base metal sulfide veins

associated with the Goldstrike stock, and historic silver, copper, and lesser gold production associated with the Mill Canyon stock, indicate that these districts may also have a high potential for gold mineralization (Vanderburg, 1938; Gilluly and Masursky, 1965; Emsbo et al., 2000). While these two areas have been explored extensively, most exploration has been focused along specific stratigraphic carbonate-bearing horizons in the footwall of the Roberts Mountains Thrust (Leonardson and Rahn, 1995; Heitt et al., 2003; McCormack and Hays, 2004). It is possible that gold mineralization associated with Jurassic intrusions occurs in stratigraphic horizons that are not considered favorable hosts for Carlin-type mineralization. This relationship is clearly seen at Bald Mountain, where Carlin-type mineralization in the southern portion of the district is confined to a fixed stratigraphic horizon (Nutt and Hofstra, 2003) while IR mineralization is present in many different stratigraphic horizons (Nutt and Hofstra, 2007).

There are many Jurassic intrusions in Nevada that have historic tungsten, gold, and/or base metal mineralization that may not be thoroughly explored using modern exploration techniques. Most Jurassic intrusions have relatively abundant magnetite, are associated with copper-gold skarns, and are not likely to produce IR gold deposits. Non-magnetic intrusions with weak alteration assemblages and low sulfide contents are generally considered low potential ore-forming systems, and may not be well described in the current literature, making their potential difficult to assess. Nevertheless, the available literature on intrusive complexes in Nevada, summarized by duBray (2007), suggest some areas of high potential.

One of the most prominent mining districts in eastern Nevada associated with Jurassic intrusions is the Contact mining district in the northeastern corner of the state.

Historic workings in the Contact mining district have exploited primarily copper from quartz veins adjacent to a Jurassic granodiorite stock, and only produced 1,222 oz of gold between 1908 and 1965 (Lapointe et al., 1991). While mineralization is spatially associated with the granodiorite stock, alteration is most intense along later quartz monzonite and syenite dikes, arguing for a multiphase magmatic system (Lapointe et al., 1991). Anomalous tin and molybdenum reported from assays of dump material, along with the presence of borosilicates, suggest that the late phases of magmatism were highly evolved, and may have some potential for IR gold mineralization (Tingley, 1981). The evolution of the magma appears to be from a mafic to felsic magma, in contrast to the increasingly mafic recharge events at RBM. This, along with the high magnetite content of the intrusions, suggests that the Contact mining district may not be as highly prospective for IR gold deposits as Bald Mountain.

A large system of Jurassic intrusions is present around the historic Austin mining district, ~125 km southwest of Bald Mountain. The Austin mining district was a silver district mined heavily begininning in the 1860's. While historic records do not report exact ratios of metals in ore produced in the early years, better record keeping prevailed between 1902 and 1936, during which time 420,000 fine ounces of silver and 2,100 fine ounces of gold, along with 21,000 pounds of copper, and 194,000 pounds of lead were produced from lode deposits (Ross, 1953). Mineralization in this district is found in quartz veins cutting a Jurassic quartz monzonite stock, and in bedding-parallel fractures in adjacent quartzite. The stock has a very low magnetite content (<1%), and is cut by pegmatite, aplite, and late lamprophyre dikes, all indicating a high potential for intrusion-related gold deposition (Ross, 1953). Brecciated quartzite cemented by quartz, with

significant arsenopyrite, was exploited as lode deposits in the northern portions of the district. Ross has identified multiple phases of alteration and mineralization, with early high-temperature barren quartz and rhodocrosite overprinted by late chalcedonic quartz and calcite. Given the size of the Jurassic intrusion, presence of arsenopyrite and multiple alteration events, and the amount of silver produced from the district, IR gold mineralization should be explored for in this district. Jurassic intrusions are also present south of Austin, which may have potential for IR gold mineralization. Tungsten mineralization is associated with Jurassic granitic rocks in the Spencer Hot Springs area, but, thus far, no gold mineralization has been identified (Stager and Tingley, 1988). Gold mineralization is spatially associated with Jurassic granodiorite intrusions at Northumberland, but the intrusions are generally weakly altered and gold mineralization is considered to be Eocene in age (Ott, 1983; Kleinhampi and Ziony, 1984). In this area of central Nevada, the Austin district is the most prospective, and exploration should be focused on favorable host rocks such as carbonates adjacent to the quartz monzonite stock, particularly in zones that have arsenic anomalies and/or are intruded by late lamprophyre dikes.

There are a series of Jurassic intrusions between Bald Mountain and the Dolly Varden Mountains to the east that have a potential for IR gold mineralization. Breccia-hosted skarn mineralization has been identified in the Dolly Varden range related to quartz latite porphyry dikes associated with the Melrose stock (Atkinson et al., 1982). The stock contains 1-2% magnetite, and the associated mineralization is copper-rich and gold-poor, indicating it is best classified as a porphyry base-metal system as opposed to a IR system (Atkinson et al., 1982; Stubbs, 1984). Nevertheless, the shallow level of

emplacement, multiphase nature of the stock, and anomalous bismuth, indicate significant fractional crystallization, favorable evolution of the magma, and multiple magma recharge events that may have resulted in nearby IR deposits. Several other deposits to the west of the Dolly Varden range, including Delker and Mud Springs, appear to be related to Jurassic intrusions. The highest potential intrusive complex for IR gold in this area is Spruce Mountain, just east of Delker. While the age of the associated granitic intrusions is unknown, the presence of granite porphyry and late-stage lamprophyre dikes in some ore zones is similar to Bald Mountain (Lapointe et al., 1991). The property has historically produced lead and silver from skarn material, and has been recently explored as a copper-molybdenum porphyry system (Lapointe et al., 1991). In addition, a tungsten deposit apparently associated with similar intrusions was mined in the 1950s (Stager and Tingley, 1988). The presence of a porphyry copper-molybdenum deposit proximal to a tungsten deposit associated with a granite porphyry, which is intruded by late-stage mafic dikes strongly resembles the RBM deposit. Spruce Mountain stands out as a more felsic system than most of the Jurassic systems in Nevada, and has the highest potential for IR gold mineralization in eastern Nevada in the opinion of the author. In addition, other reduced Jurassic intrusions in this region, which have undergone considerable assimilation of reduced crustal material, and do not have associated magnetic anomalies, could have significant associated gold mineralization, but may be difficult to identify in the subsurface.

IX. Conclusion

The RBM deposit is best characterized as an IR deposit emplaced at a depth of <3 km. Gold partitioned into magmatic aqueous fluids exsolved from a magmatic melt during fractional crystallization of a large composite pluton. The fluids collected in the carapace of the evolving magma chamber. Early pulses of magmatism and fluid release were associated with prograde quartz veining, potassic alteration, and molybdenite + electrum + weak base metal and skarn mineralization. As the system cooled, the hydrothermal fluid flow began to collapse resulting in precipitation of silica along the latest intrusions and structures marked by equigranular quartz monzodiorite intrusions that were already slightly enriched with incompatible elements. Gold and other metals continued to become enriched in the underlying carapace until at some point, possibly due to the intrusion of primitive magma into the partially solidified and highly fractionated magma chamber, the fluid pressure of the carapace exceeded its lithostatic load, resulting in magmatic-hydrothermal brecciation. Gold was introduced with these later fluids as the system continued to release acidic volatiles into the overlying rocks and formed gold-bearing quartz-kaolinite-marcasite alteration in matrices of the breccias. As the hydrothermal system collapsed, surficial acidic fluids precipitated late arsenian marcasite, and CO_2 laden fluids penetrated the inner mineralized zones along late fracture sets resulting in a final episode of ankerite + pyrite mineralization.

Uplift and erosion during the Miocene (?) resulted in exposure of hypogene sulfides to oxidized meteoric water, and the formation of sulfuric acid which leached K, Na, and other cations, resulting in supergene argillic alteration. Cu, Zn, and other metals

that are mobile in an oxidized, acidic environment were leached from the oxidized portions of the deposit and reprecipitated as chalcocite and other supergene minerals at the oxide-sulfide interface. The clay-rich nature of the deposit led to channelized phreatic fluid flow, perched water tables, and an irregular supergene blanket that developed in isolated patches throughout the deposit. At some point in the Miocene, or later, a weak hydrothermal system formed, possibly as the result of Basin and Range tectonism, resulting in warm water (~70-200°C) upwelling along open fractures and reactivated Jurassic structures (e.g. the RBM fault). These fluids partially reset some (U-Th)/He ages but were likely short lived and had a minimal impact on metal mobilization.

X. References

Abdi, H., 2003, Factor rotations in factor analyses *in* Lewis-Beck, M., Bryman, A., and Futing, T. eds., Encyclopedia of Social Sciences Research Methods, Thousand Oaks, CA, Sage, 8 p.

Arehart, G.B., 1996, Characteristics and origin of sediment-hosted disseminated gold deposits: A review; Ore Geology Reviews, v. 11, p. 383-403.

Arehart, G.B., Chakurian, A.M., Tretbar, D.R., Christensen, J.N., McInnes, B.A., and Donelick, R.A., 2003, Evaluation of radioisotope dating of Carlin-type deposits in the Great Basin, western North America, and implications for deposit genesis: Economic Geology, v. 98, p. 235-248

Arehart, G.B., Chryssoulis, S.L., and Kesler, S.E., 1993, Gold and arsenic in iron sulfides from sediment-hosted disseminated gold deposits: Implications for depositional processes: Economic Geology, v. 88, p. 171-185.

Arehart, G.B., and Donelick, R.A., 2006, Thermal and isotopic profiling of the Pipeline hydrothermal system: Application to exploration for Carlin-type gold deposits: Journal of Geochemical Exploration, v. 91, p. 27-40.

Arehart, G.B., Kesler, S.E., O'Neil, J.R., and Foland, K.A., 1992, Evidence for the supergene origin of alunite in sediment-hosted micron gold deposits, Nevada: Economic Geology, V. 87, p. 263-270.

Atkinson, W.W., Jr., Kaczmarowski, J.H., and Erikson, A.J., Jr., 1982, Geology of a skarn-breccia orebody at the Victoria mine, Elko County, Nevada: Economic Geology, v. 77, p. 899-918.

Baker, E.M., and Andrew, A.S., 1991, Geologic, fluid inclusion, and stable isotope studies of the gold-bearing breccia pipe at Kidston, Queensland, Australia: Economic Geology, v. 86, p. 810-830.

Baker, T., Ebert, S., Rombach, C., and Ryan, C.G., 2006, Chemical compositions of fluid inclusions in intrusion-related gold systems, Alaska and Yukon, Using PIXE Microanalysis: Economic Geology, v. 101, p. 311-327.

Barton, M.D., 1990, Cretaceous magmatism, metamorphism, and metallogeny in the east-central Great Basin: Geological Society of America Memoir 174, p. 283-302.

Barton, M.D., Battles, D.A., Debout, G.E., Capo, R.C., Christensen, J.N., Davis, S.R., Hanson, R.B., Michelsen, C.J., Trim, H.E., 1988, Mesozoic contact metamorphism in the Western United States, *in* W.G. Ernst, ed., Metamorphism

and Crustal Evolution , Western Conterminous United States: Rubey Volume, v. 7, Prentice-Hall, Englewood Cliffs, New Jersey, p. 110-178.

Bettles, K., 2002, Exploration and geology, 1962 to 2002, at the Goldstrike Property, Carlin Trend, Nevada: Society of Economic Geologists Special Publication, v. 9, p. 275-298.

Blatt, H., and Tracy, R.J., 1995, Petrology, 2nd ed. WH Freeman and Company: New York, p. 61-80.

Burnham, C.W., 1985, Energy release in subvolcanic environments: Implications for breccia formation: Economic Geology, v. 80, p. 1515-1522.

Campbell, I.H., Ballard, J.R., Palin, J.M., Allen, C., and Faunes, A., 2006, U-Pb zircon geochronology of the granitic rocks from the Chuquicamata-El Abra porphyry copper belt of northern Chile: excimer laser ablation (ICP-MS) analysis: Economic Geology, v. 101, p. 1327-1344.

Castor, S.B., Boden, D.R., Henry, C.D., Cline, J.S., Hofstra, A.H., McIntosh, W.C., Tosdal, R.M., and Wooden, J.P., 2003, The Tuscarora Au-Ag District, Eocene volcanic-hosted epithermal deposits in the Carlin gold region, Nevada: Economic Geology, v. 98, p. 339-366.

Cerny, P., Blevin, P.L., Cuney, M., and London, D., 2005, Granite-related ore deposits: Economic Geology 100th anniversary volume, p. 337-370.

Christiansen, R.L., and Yeats, R.S., 1992, Post-Laramide geology of the U.S. Cordilleran region *in* Burchfiel, B.C., Lipman, P.W., and Zobak, M.L., eds. The Cordilleran Orogen: Conterminous U.S., v. G-3, p. 261-406.

Cline, J.S., Hofstra, A., Landis, G., and Rye, R., 1997, Ore fluids at the Getchell Carlin-type gold deposit, north-central Nevada *in* Vikre, P., Thompson, T.B., Bettles, K., Christensen, O., and Parrat, R., eds., Carlin-Type Gold Deposits Field Conference: Society of Economic Geologists Guidebook Series, v. 28, p. 155-166.

Cline, J.S., Hofstra, A.H., Muntean, J.L., Tosdal, R.M., and Hickey, K.A., 2005, Carlin-type gold deposits in Nevada, USA: Essential features, viable models, and comparisons to similar deposits: Economic Geology 100th Anniversary Volume, p. 451-484.

Cline, J., Muntean, J., Longo, A., Cassinerio, M., 2008, Collaborative research on fluid pathways and metal transport in Carlin-type gold deposits: insights from the Getchell deposit: USGS Mineral Resources External Research Program Report, October 2008, 128 p.

Columba, M.C., and Cunningham, C.G., 1993, Geologic model for the mineral deposits of the La Joya distrct, Oruro, Bolivia: Economic Geology, v. 88, p. 701-708.

Dilles, J.H., 1987, Petrology of the Yearington Batholith, Nevada: Evidence for evolution of porphyry copper ore fluids: Economic Geology, v. 82, p. 1750-1789.

Dilles, J.H., and Einaudi, M.T., 1992, Wall-rock alteration and hydrothermal flow paths about the Ann-Mason porphyry copper deposit, Nevada- a 6-km vertical reconstruction: Economic Geology, v. 87, p. 1963-2001.

Dilles, P.A., Wright, W.A., Monteleone, S.A., Russell, K.D., Marlowe, K.E., Wood, R.A., and Margolis, J., 1996, The geology of the West Archimedes Deposit: A new gold discovery in the Eureka Mining District, Eureka County, Nevada, *in* Coyner, A.R., and Fahey, P.L., eds., Geology and Ore Deposits of the American Cordillera: Geological Society of Nevada Symposium proceedings, Reno/Sparks, Nevada, April 1995, p. 159-171.

Donelick, R.A., and Schmauder, G.C., 2004 Bald Mountain and vicinity: apatite fission-track and ZHe data: Apatite to Zircon Report Number 576, University of Nevada, Reno, May 2004.

Donelick, R.A., O'Sullivan, P.B., and Ketcham, R.A., 2005, Apatite fission-track analyses: Reviews in Mineralogy and Geochemistry, v. 58, p. 49-94.

Dunai, T.J., 2005, Forward modeling and interpretation of (U-Th)/He ages: Reviews in Mineralogy and Geochemistry, v. 58, p. 259-274.

du Bray, E.A., 2007, Time, space, and composition relations among northern Nevada intrusive rocks and their metallogenic implications: Geosphere, v. 3, p. 381-405.

Einaudi, M.T.,1997, Mapping altered and mineralized rocks: an introduction to the "Anaconda Method:" Stanford University unpublished document, March 1997, 10 p.

Elliott, J.E., and Wells, J.D., 1968, Anomalous concentrations of gold, silver, and other metals in the Mill Canyon area, Cortez Quadrangle, Eureka and Lander counties, Nevada: US Geological Survey Circular, report C 606, 20 p.

Emsbo, P., 1999, Origin of the Meikle High-grade gold deposit from the superposition of late Devonian SEDEX and mid-Tertiary Carlin-type gold mineralization: unpublished dissertation, Colorado School of Mines, 288 p.

Emsbo, F., Hofstra, A.H., and Luaha, E.A., 2000, Jurassic auriferous polymetallic mineralization at the Goldstrike mine, Carlin Trend, Nevada [abs.]: Geology and Ore Deposits 2000: The Great Basin and Beyond Symposium, Geological Society of Nevada, Reno/Sparks, Nevada, May 2000, Proceedings, p. B2.

Faure, G., 1986, Principles of isotope geology (2^{nd} ed.): New York, NY, Wiley, 589 p.

Fitzmayer, J.R., 1999, Sulfide Mineralogy, wall-rock alteration, and geologic model of the Kori Kollo gold-silver deposit, Bolivia, Univerity of Utah unpublished MS thesis, 237 p.

Fournier, R.O., 1967, The porphyry copper deposit exposed in the Liberty open-pit mine near Ely, Nevada; Part 1, Syngenetic Formation: Economic Geology, v. 62, p. 57-81.

Fournier, R.O., 1989, Geochemistry and dynamics of the Yellowstone National Park hydrothermal system: Annual Review of Earth and Planetary Science, v. 52, p. 13-53.

Gilluly, J., and Masursky, H., 1965, Geology of the Cortez Quadrangle, Nevada: US Geological Survey Bulletin 1175, 117p.

Govett, G.J.S.,1983, Rock geochemistry in mineral exploration: Handbook of exploration geochemistry, Elsevier Scientific, New York, v. 3, 461p.

Gustafson, L.B., and Hunt, J.P., 1975, The porphyry copper deposit at El Salvador, Chile: Economic Geology, V. 70, p. 857-912.

Gehrels, G., and Ruiz, J., in review, U-Th-Pb geochronology of zircon by Laser Ablation Multicollector ICP Mass Spectromety at the Arizona LaserChron Center: Journal of Analytical Atomic Spectrometry

Harrison, T.M., Duncan, I., and McDougall, I., 1985, Diffusion of ^{40}Ar in biotite: Temperature, pressure and compositional effects: Geochimica et Cosmochimica Acta, v. 49, p. 2461-2468.

Hart, C.J.R., McCoy, D.T., Goldfarb, R.J., Smith, M., Roberts, P., Hulstein, R., Bakke, A.A., and Bundtzen, T.K., 2002, Geology, exploration, and discovery in the Tintina gold province, Alaska and Yukon: Society of Economic Geologists Spectial Publication 9, p. 241-274.

Harker, A., 1908, The geology of the Small Isles of Inverness-shire (Rhum, Canna, Eigg, Muck, etc.): Scotland Geol. Survey Mem., 210p.

Heitt, D.G., Dunbar, W.W., Thompson, T.B., and Jackson, R.G., 2003, Geology and geochemistry of the Deep Star gold deposit, Carlin Trend, Nevada: Economic Geology, v. 98, p. 1107-1135.

Henkelmann, C.A., 2000, Pyrite geochemistry across the Betze-Post deposit, northern Carlin trend, Nevada: unpublished MS thesis, University of Nevada, Las Vegas, 150p.

Henry, C.D., Elson, H.B., McIntosh, W.C., Heizler, M.T., and Castor, S.B., 1997, Brief duration of hydrothermal activity at Round Mountain, Nevada, determined from $^{40}Ar/^{39}Ar$ geochronology: Economic Geology, v. 92, p. 807-826.

Hickey, K., Tosdal, R., Dipple, G., Donelick, R., and Arehart, G., 2007, The thermal footprint of Carlin-type Au-deposits – defining the far-field extent of hydrothermal flow using low-temperature thermochronology *in* Andrew, C.T. and others, eds., Deeper Digging, Proceedings of the ninth biennial meeting of the Society of Geology Applied to Mineral Deposits: Irish Association for Economic Geology, Dubland, Ireland, August 20-23, 2007, p. 1251-1254.

Hill, J.M., 1916, Notes on some mining districts in Nevada: US Geological Survey Bulletin, 648, p. 152-161.

Hitchborn, A.D., Arbonies, D.G., Peters, S.G., Connors, K.A., Noble, D.C., Larson, L.T., Beebe, J.S., and McKee, E.H., 1996, Geology and gold deposits of the Bald Mountain Mining District, White Pine County, Nevada: *in* Coyner, A.R., and Fahey, P.L., eds., Geology and Ore Deposits of the American Cordillera, Symposium Proceedings, Geological Socitey ot Nevada, Reno, Nevada, p. 505-546.

Hofstra, A.H., and Cline, J.S., 2000, Characteristics and models for Carlin-type gold deposits: Reviews in Economic Geology, v. 13, p. 163-220.

Hose, R.K., and Blake, M.C. Jr., 1976, Geology and mineral deposits of White Pine County, Nevada: Nevada Bureau of Mines and Geology Bulletin 85, 105p.

Howard, K.A., 2003, Crustal structure in the Elko-Carlin region, Nevada, during Eocene gld mineralization; Ruby-East Humbolt metamorphic core complex as a guide to the deep crust: Economic Geology, v. 98, p. 249-268.

Ilchik, R.P., 1990, Geology and geochemistry of the Vantage gold deposits, Alligator Ridge-Bald Mountain mining district, Nevada: Economic Geology, v. 85, p. 50-75.

John, D.A., 2001, Miocene and early Pliocene epithermal gold-silver deposits in the northern Great Basin, western United States: characteristics, distribution, and

relationship to magmatism: Economic Geology, v. 96, p. 1827-1853.

John, D.A., Hofstra, A.H., Fleck, R.J., Brummer, J.E., and Saderholm, E.C., 2003, Geologic setting and genesis of the Mule Canyon low-sulfidation epithermal gold-silver deposit, North-Central Nevada: Economic Geology, v. 98, p. 425-463.

Johnston, M.K., Thompson, T.B., Emmons, D.L., and Jones, K., 2008, Geology of the Cove Mine, Lander County, Nevada, and genetic implications for the McCory-Cove hydrothermal system: Economic Geology, v. 103, p. 759-782.

Ketcham, R.A., 2005, Forward and Inverse Modeling of Low-Temperature Thermochronometry Data: Reviews in Mineralogy and Geochemistry, v. 58, p. 275-314.

Ketcham, R.A., 2008, HeFTy v. 1.5.5.<www.minsocam.org/MSA/RIM/software_rim58> (Update received electronic comm. April 1, 2008)

Ketcham, R.A., Donelick, R.A., and Donelick, M.B., 2000, AFTSolve: A program for multi-kinetic moderling of apatite fission-track data: Geological Materials Research, v. 2, p. 1-32.

Kleinhampi, F.J., and Ziony, J.I., Mineral resources of northern Nye County, Nevada: Nevada Bureau of Mines and Geology Bulletin 99B, 243p.

Lang, J.R., and Baker, T., 2001, Intrusion-related gold systems: the present level of understanding: Mineralium Deposita, v. 36, p. 477-489.

Lang, J.R., Baker, T., Hart, C.J.R., and Mortensen, J.K., 2000, An exploration model for intrusion-related gold systems: SEG Newsletter, v. 40, p. 7-15.

Lanphere, M.A., and Dalrymple, G.B., 1978, The use of $^{40}Ar/^{39}Ar$ data in evaluation of disturbed K-Ar systems: U.S. Geological Survey Open File Report OF 78-701, p. 241-243.

Lapointe, D.D., Tingley, J.V., and Jones, R.B., 1991, Mineral resources of Elko County, Nevada: Nevada Bureau of Mines and Geology Bulletin 106, 236 p.

Leavitt, E.D., Spell, T.L., Goldstrand, P.M., and Arehart, G.B., 2004, Geochronology of the Midas low-sulfidation epithermal gold-silver deposit, Elko County, Nevada: Economic Geology, v. 99, p. 1665-1686.

Leonardson, R.W., and Rahn, J.E., 1995, Geology of the Betze-Post gold deposits, Eureka County, Nevada in Coyner, A.R., and Fahey, P.L., eds., Geology and ore deposits of the American Cordilera; Symposium Proceedings, v. 1, p. 61-94.

Long, K.R., DeYoung, J.H., and Ludington, S.D., 1998, Database of significant deposits of gold, silver, copper, lead, and zinc in the United States, US Geological Survey Open-File Report 98-0206-A, 33p.

Long, K., Ludington, S., duBray, E., Andre-Ramos, O., McKee, E.H., 1992, Geology and mineral deposits of the La Joya district, Bolivia: SEG Newsletter 10:1, 13-16.

Mach, C.J., 2008, Unpublished field mapping, Barrick Gold Corp., December, 2008.

Margolis, J., 1997, Gold paragenesis in intrusion-marginal sediment-hosted gold mineralization at Eureka, Nevada, in Vikre, P. and others, eds., Carlin-type gold deposits field conference: Society of Economic Geologists, Guidebook Series, v. 28, p. 213-221.

Marlowe, C. and Russell, K., 2004, Summary and field trip stops, West Archimedes gold deposit, Northern Eureka mining district, Eureka County, Nevada, in Kredwell, D., Olmstead, L., French, G., and Rigdley, GSN SP 40, p. 119-127.

Marsh, T.M., Einaudi, M.T., and McWilliams, M., 1997, $^{40}Ar/^{39}Ar$ geochronology of Cu-Au an Au-Ag mineralization in the Portrerillos District, Chile: Economic Geology, v. 92, p. 784-806.

Maybe, D.R., 1966, Regional gravity and magnetic anomalies in part of Eureka County, Nevada *in* Hansen, D.A., et al., eds., Mining Geophysics: Tulsa, Oklahoma, Society of Exploration Geophysicists, v. 1, p. 77-83.

McDougall, I., and Harrison, M.T., 1999, Geochronology and Thermochronology by the $^{40}Ar/^{39}Ar$ Method. 2nd ed., Oxford University Press, New York.

McCormack, J.K., and Hays, R.C., 2004, Cresent Valley; a model for reconstruction of district mineralization in the Basin and Range: Geological Society of Nevada special publication, v. 40, p. 167-180.

McCoy, D.T., Newberry, R.J., Layer, P.W., DiMarchi, J.J., Bakke, A., Masterman, J.S., and Minehane, D.L., 1997, Plutonic related gold deposits of interior Alaska: Economic Geology Monograph 9, p. 151-190

McInnes, B.I.A., Evans, N.J., Fu, F.Q., and Garwin, S., 2005, Application of thermochronology to hydrothermal ore deposits: Reviews in Mineralogy and Geochemistry, v. 58, p. 467-498.

Miller, E.L., Gans, P.B., Wright, J.F., and Sutter, J.F., 1988, Metamorphic history of the east-central basin and range province: tectonic setting and relationship to magmatism *in* Ernst, W.G. ed., Metamorphism and crustal evolution of the western United States, Rubey Volume 7, p. 572-605.

Miller, D.M., and Hoisch, T.D., 1995, Jurassic tectonics of northeastern Nevada and northwestern Utah from the perspective of barometric studies: Geolocigal Society of America Special Paper 299, p. 267-294.

Morrell, B., Jory, J., Moss, K., Jones, A., Curnow, R., and Rice, T., 2009, Bald Mountain Mine December 2008 Reserves Technical Report, Barrick Bald Mountain, p. 10.

Mortenson, J.K., Thompson, J.F.H., and Tosdal, R.M., 2000, U-Pb age constrains on magmatism and mineralization in the northern Great Basin: Geology and Ore Deposits 2000: The Great Basin and Beyond Symposium, Geological Society of Nevada, Reno/Sparks, Nevada, May 2000, Proceedings, p. 419-438.

Mortenson, J.K., 2007, Unpublished U-Pb ID-TIMS zircon dates for Barrick Bald Mountain Exploration, May 16, 2007.

Muntean, J.L., Coward, M.P., and Tarnocai, C.A., 2007, Reactivated normal faults: controls on the formation of Carlin-type gold deposits in north-central Nevada *in* Reis, A.C., Butler, R.W.H., and Graham, R.H., eds., Deformation of the Continental Crust – The Legacy of Mike Coward: Geological Society of London Special Publications, v. 272, p. 573-589.

Muntean, J.L., and Einaudi, M.E., 2000, Porphyry gold deposits of the Refugio district, Maricunga belt, northern Chile: Economic Geology, v. 95, p. 1445-1472.

Mustard, R., 2001, Granite-hosted gold mineralization at Timbarra, northern New South Wales, Australia: Mineralium Deposita, v. 36, p. 542-562.

Mustard, R., Ulrich, T., Kamenetsky, V.S., and Memagh, T., 2006, Gold and metal enrichment in natural granitic melts during fractional crystallization: Geology, v. 34, p. 85-88.

Myers, G., Dennis, M.D., Wilkinson, W.H., Wendt, C.J., 1991, Precious-metal distribution in the Mount Hamilton polymetallic skarn system, Nevada: Geology and ore deposits of the Great Basin, Reno, NV, United States, p. 393-403.

Noble, D.C., 1988, Cenozoic volcanic rocks of the northwestern Great Basin: An overview: Geological Society of Nevada Special Publication 7, p. 31-42.

Nolan, T.B., 1962, The Eureka mining district, Nevada: US Geological Survey Professional Paper 406, 78p.

Nutt, C.J., 2000, Geologic map of the Alligator Ridge area, including the Buck Mountain East and Mooney Basin Summit quadrangles and parts of the Sunshine Well NE

and Long Valley Slough quadrangles, White Pine County, Nevada: US Geological Survey Map 1-2691, scale 1:24,000.

Nutt, C.J., and Hart, K.S., 2004, Geologic map of the Big Bald Mountain Quadrangle and part of the Tognini Spring Quadrangle: Nevada Bureau of Mines and Geology Map 145, scale 1:24,000, 9 p.

Nutt, C.J., and Hofstra, A.H., 2003, Alligator Ridge district, east-central Nevada; Carlin-type gold mineralization at shallow depths: Economic Geology, v. 98, p. 1225-1241.

Nutt, C.J., and Hofstra, A.H., 2007, Bald Mountain gold mining district, Nevada: a Jurassic reduced intrusion-related gold system: Economic Geology, v. 102, p. 1129-1155.

Nutt, C.J., Hofstra, A.H., Hart, K.S., and Mortensen, J.K., 2000, Structural setting and genesis of gold deposits in the Bald Mountain-Alligator Ridge area, east-central Nevada: Geology and Ore Deposits 2000: The Great Basin and Beyond Symposium, Geological Society of Nevada, Reno/Sparks, Nevada, May 2000, Proceedings, p. 513-537.

Ott, L.E., 1983, Geology and ore localization at the Northumberalnd gold mine, Nye County, Nevada: unpublished masters thesis, Montana College of Mineral Science and Technology, Butte, Montana, 52 p.

Price, J.G., The Nevada Minerals Industry 2007: Overview: Nevada Bureau of Mines and Geology Special Publication MI-2007, Reno, NV, p. 3-26.

Patterson, L.M., 2009, Documentation of the hydrothermal footprint of a carlin-type deposit at the district scale: Jerritt Canyon Mining District, Elko County, Nevada: University of Nevada, Reno unpublished MS thesis, 255 p.

Poole, F.G., Stewart, J.H., Palmer, A.R., Sandberg, C.A., Madrid, R.J., Ross, R.J., Hintze, L.F., Miller, M.M., and Wrucke, C.T., 1992, Latest Precambrian to latest Devonian time; Developmen of a continental margin *in* Burchfiel, B.C., Lipman, P.W., and Zobak, M.L., eds., The Cordilleran Orogen: Conterminous U.S., v. G-3, p. 9-56.

Rae, A., Davidson, G.J., and Danyushevsky, L.V., 2004, LA-ISPMS analysis of fine grained (<5 mm), Au-bearing, arseniferous pyrite from the Deep Star, a carlin-type gold deposit: Geological Society of Australia Abstracts, v. 73, p. 112.

Reiners, P.W., 2005, Zircon (U-Th)/He Thermochronometers: Reviews in Mineralogy and Geochemistry, v. 58, p. 151-179.

Reiners, P.W., Spell, T.L., Nicolescu, S., and Zanetti, K.A., 2004, Zircon (U-Th)/He thermochronometry: He diffusion and comparisons with $^{40}Ar/^{39}Ar$ dating: Geochimica Cosmochimica Acta, V. 68, p. 1857-1887.

Ressel, M.W., and Henry, C.D., 2006, Igneous geology of the Carlin trend, Nevada: development of the Eocene plutonic complex and significance for Carlin-type gold deposits: Economic Geology, v. 101, p. 347-383.

Rigby, J.K., 1960, Geology of the Buck Mountain-Bald Mountain area, southern Ruby Mountains, White Pine County, Nevada *in* Guidebook to the geology of east-central Nevada: Intermountain Association of Petrolium Geologists and eastern Nevada Geological Society 11th Annual Field Conference, Salt Lake City, Utah, 1960, p. 1773-1800.

Roberts, 1960, Alignment of mining districts in north-central Nevada: US Geological Society Professional Paper 400-B, p. B17-B19.

Ross, C.P., 1953, The geology and ore deposits of the Reese River District, Lander County, Nevada: Geological Survey Bulletin 997, 132 p.

Schmauder, G.C., 2005, Thermal and Chemical Profiling of the Bald Mountain District, White Pine County, Nevada, unpublished University of Reno MS thesis, 61p.

Schmauder, G.C., Arehart, G.B., and Donelick, R.A., 2005, Thermal and chemical profiling of the Bald Mountain district, White Pine County, Nevada, *in* Rhoden, H.N., Steininger, R.C., and Vikre, P.G., eds., Geological Society of Nevada Symposium 2005: Window to the World, Reno, Nevada, May 2005, p. 531-542.

Seedorf, E., Breitrick, R.A., Hasler, R.W., Fahey, P.L., Jeanne, R.A., Shaver, S.A., Stubbe, P., Troutman, T.W., and Manske, S.L., 1995, Overview of the Robinson District, White Pine County, Nevada, with emphasis on structural reconstruction of the Ely Porphyry Cu-(Mo-Au) system, Abstracts with programs, 1995 GSN Cordilleran Symposium.

Seedorff, E., Dilles, J.H., Proffett, J.M. jr., Einaudi, M.T., Zurcher, L., Stavart, W.J.A., Johnson, D.A., and Barton, M.D., 2005, Porphyry deposits: Characteristics and origin of hypogene features: Economic Geology 100th anniversary volume, p. 251-298.

Sillitoe, R.H., 1985, Ore-related breccias in volcanoplutonic arcs; Economic Geology, v. 80, p. 1467-1514.

Sillitoe, R.H., Steele, G.B., Thompson, J.H.F., and Lang, J.R., 1998, Advanced argillic lithocaps in the Bolivian tin-siver belt: Mineralium Deposita, v. 33, p. 539-546.

Simmons, S.F., White, N.C., and John, D.A., 2005 Geological Characteristics of Epithermal Precious and Base Metal Deposits: Economic Geology 100th Anniversary Volume, p. 485-522.

Smith, A.M., and Vanderburg, W.O., 1932, Placer mining in Nevada: University of Nevada Bulletin: Geology and Mining Series, Nevada Bureau of Mines and Geology, Reno, NV, v. 26, n. 8, 104p.

Smith, R.M., 1976, Mineral Resources *in* Geology and Mineral Resources of White Pine County: Nevada Bureau of Mines and Geology Bulletin 85, p. 36-99.

Snoke, A.W., and Howard, K.A., 1984, Geology of the Ruby Mountains-East Humbolt Range, Nevada: A Cordilleran metamorphic complex *in* Lintz, J., Jr., ed., Western geological excursions (Geological Society of America 1984 annuan meeting field trip guidebook): Mackay School of Mines, Reno, Nevada, p. 260-303.

Snoke, A.W., and Lush, A.P., 1984, Polyphase Mesozoic-Cenozoic deformational history of the northern Ruby Mountains-East Humboldt Range, Nevada: A Cordilleran metamorphic complex, *in* Lintz, J., Jr., ed., Western geological excursions (Geological Society of America 1984 annuan meeting field trip guidebook): Mackay School of Mines, Reno, Nevada, p. 232-260.

Snoke, A.W., and Miller, D.M., 1988, Metamorphic and tectonic history of the northeastern Great Basin *in* Ernst, W.G. ed., Metamorphism and crustal evolution of the western United States, Rubey Volume 7, p. 572-605.

Speed, R., Elison, M.W., and Heck, F.R., 1988, Phanerozoic tectonic evolution of the Great Basin *in* Ernst, W.G. ed., Metamorphism and crustal evolution of the western United States, Rubey Volume 7, p. 572-605.

Stager, H.K., and Tingley, J.V., 1988, Tungsten deposits in Nevada: Nevada Bureau of Mines and Geology Bulletin 105, 256p.

Staudacher, T.H., Jessberger, E.K., Dorflinger, D., and Kiko, J., 1978, A refined ultrahigh-vacuum furnace for rare gas analysis: Journal of Physics E: Scientific Instruments, v. 11, p. 781-784.

Stewart, J.H., 1980, Geology of Nevada: Nevada Bureau of Mines and Geology Special Publication 4, p. 1-135.

Stewart, J.H., and McKee, E.H., 1977, Geology and mineral deposits of Lander County, Nevada: Nevada Bureau of Mines and Geology Bulletin 88, 106p.

Stubbs, G.S., 1984, Geology of a contact zone: Dolly Varden Mountains, Elko County, Nevada: unpublished masters thesis, Cornell College, 86p.

Taylor, A. V., 1982, An introduction to error analysis: Mill Valley, California, University Science Books, 269 p.

Theodore, T.G., and Blake, D.W., 1978, Geology and geochemistry of the West Ore Body and associated skarns, Copper Canyon porphyry copper deposits, Lander County, Nevada: US Geological Survey Professional Paper, Report: P 798-C, 85 p.

Thompson, T.B., 2004, Igneous rocks of the northwestern part of the Bald Mountain district, Nevada: unpub. Placer Dome rept., 48 p.

Thompson, J.F.H., and Newberry, R.J., 2000, Gold deposits related to reduced granitic intrusions: Reviews in Economic Geology, v. 13, p. 377-400.

Thompson, J.F.H., Silltoe, R.H., Baker, T., Lang, J.R., and Mortensen, J.K., 1999, Intrusion-related gold deposits associated with tungsten-tin provinces: Mineralium Deposits, v. 34, p. 323-334.

Tingley, J.V., 1981, Summary report, mineral inventory of the Wells resource area, Elko District, Elko County, Nevada, NBMG Open-file report 81-4.

Vanderburg, W.O., 1938, Reconnaissance of mining districts in Eureka County, Nevada: U.S. Bureau of Mines Information Circular 7022, 66 p.

Vikre, P.G., 1998, Intrusion-related, polymetallic carbonate replacement deposits in the Eureka District, Eureka County, Nevada: Nevada Bureau of Mines and Geology Bulletin, v. 110, 52 p.

Wannamaker, P.E., and Doerner, W.M., 2002, Crustal structure of the Ruby Mountains and southern Carlin trend region, northeastern Nevada, from magnetotelluric data: Ore Geology Reviews, v. 21, p. 185-210.

Wells, J.D., and Mullins, T.E., 1973, Gold-bearing arsenian pyrite determined by microprobe analysis, Cortez and Carlin gold mines, Nevada: Economic Geology, v. 68, p. 187-201.

Westra, G., and Riedell, K.B., 1996, Geology of the Mount Hope stockwork molybdenum deposit, Eureka County, Nevada: Geological Society of Nevada, Geology and Ore Deposits of the American Cordillera Symposium, Reno-Sparks, Nevada, April 1995, Proceedings, p. 1639-1666.

Wright, B., 2006, Bald Mountain Intrusive Suites, Barrick internal memorandum, 12 p.

Zoback, M.L., and Thompson, G.A., 1978, Basin and Range rifting inn northern Nevada: Clues from a mid-Miocene rift and its subsequent offsets: Geology, v. 6, p. 111-116.

Appendix 1: Microprobe Analyses

Sulfide phases from 4 thin sections from the RBM deposit were analyzed using a JEOL electron probe microanalyzer (JXA-8900 (EPMA)) at the University of Nevada-Las Vegas. Conditions for the microprobe were set at an accelerating voltage of 20kV, a beam current of 10nA (1.0E-7A), and a beam diameter of 1μm. A suite of 17 major and trace elements selected to define elemental variations in sulfide phases that may be significant to gold mineralization were measured simultaneously using four wavelength dispersive (WDS) X-ray spectrometry as defined in table 1. Fine-grained marcasite is differentiated petrographically from pyrite based on its anisotropy but could not be consistently differentiated in some samples analyzed due to fine grain size and similar habits. Therefore fine-grained marcasite as described here may include some fine-grained pyrite. Spot analyses were each approximately 50 minutes. Gold was measured using the LIF-H to prevent potential peak overlaps that may occur when gold is analyzed using the PET-H.

Standards include pure metal CM1 standards for Ag, Sb, Sn, W, Bi; CM2 metal complexes for HgS, TlBr, ZnTe; pure metal Geller standard for gold, MAC standards for pyrite, chalcopyrite, sphalerite, galena, arsenic, apatite, and zircon. MAC pyrite, chalcopyrite, and chalcocite were run as unknowns using the same element suite and order used to analyze all other samples (Table 2). Experimental results on standards include: 320 ppm Cu and 180 ppm Si for MAC pyrite, 160 ppm Sb, 90 ppm Ag, and 210 ppm Si for MAC chalcopyrite, and 1,140 ppm Ag, 650 ppm Zn, and 140 ppm Si for MAC chalcocite. These data indicate possible problems in peak overlaps for Cu-Zn, Cu-

Ag, and S-Si. Anomalous Au was not detected in any of the standards. Pyrite and marcasite spots analyzed are presented in table 2 and other sulfide phases are presented in table 3.

Element	Detector	Peak Position (mm)	Peak Counts (sec.)	Background Counts (sec.)	Detection Limit (ppm)		
					Average	Min	Max
Ag	PETH	133.181	50	25	27	20	31
As	TAP	105.194	50	25	32	28	73
Au	LIF	88.675	500	250	47	27	80
Bi	PETJ	163.888	50	25	91	47	97
Ca	PETJ	107.65	30	10	24	19	46
Cu	TAP	**144.936**	30	15	191	154	511
Fe	LIF	**134.619**	30	15	55	38	61
Hg	PETH	180.83	30	15	106	62	116
Pb	PETJ	169.255	50	25	169	52	184
S	PETJ	**172.084**	30	15	21	13	22
Sb	PETJ	110.179	50	25	38	29	45
Si	TAP	77.429	30	10	21	19	29
Sn	PETJ	115.333	50	25	37	29	46
Te	PETJ	105.373	50	25	42	32	68
Tl	PETJ	174.929	100	50	1310000	589243	1410000
W	PETJ	223.7	50	25	93	82	197
Zn	LIF	99.746	50	25	56	42	71

Table 1. Analytical methods used for sample analyses. Bold peak positions are relatively abundant elements that were allowed to peak search to get better totals. Detection limit data are for pyrite and marcasite only. Other phases had higher variation.

Stage	ID #	Mineral	Description	Si	Ag	Fe	Cu	As	Hg	Zn	Au	Sb	S	Sn	W	Te	Bi	Ca	Tl	Pb	O	Total
Early	41	Early Pyrite	Euhedral brassy pyrite inclusions in chalcopyrite	0	0.007	45.61	0.053	0	0	0	0	0	52.273	0	0.022	0	0	0.007	0	0	0	97.972
Main	23	Massive Pyrite	Older darker pyrite chunks veined by 24	0.002	0	44.241	0	0.331	0.015	0	0	0	51.555	0	0	0	0	0	0	0	0.003	96.147
Main	29	Massive Pyrite	Anhedral pyrite vein in quartz	0.285	0	43.353	0.04	0.258	0	0.007	0	0	50.905	0.008	0	0	0	0.037	0	0	0.325	95.218
Main	31	Massive Pyrite	Pod of anhedral brassy pyrite	0.106	0	43.914	0.012	0.066	0.005	0	0	0	51.012	0.001	0.005	0.001	0	0.01	0	0	0.121	95.253
Main	44	Massive Pyrite	Massive pyrite vein (multiple bands ~ 10 µm in width)	0.034	0.003	45.618	0	0.178	0.006	0	0	0.008	52.101	0	0.019	0	0	0.011	0	0	0.039	98.017
Main	48	Massive Pyrite	Light pyrite vein in large dark pyrite pod	0.004	0	44.719	0.019	0.03	0	0.006	0	0	51.014	0	0.03	0.016	0	0	0	0	0.004	95.842
Main	49	Massive Pyrite	Dark pyrite veined by 48	0.001	0.002	45.79	0.009	0.014	0.009	0.008	0	0	51.88	0	0	0	0	0	0	0	0.001	97.714
Main	58	Anhedral Pyrite with Bi Inclusions	Pyrite around Bi-sulfide 55	0.001	0	44.653	0.002	0.274	0	0	0	0	51.147	0	0.015	0	0	0.003	0	0	0.001	96.096
Main	60	Anhedral Pyrite with Bi Inclusions	Dark pyrite with Bi-sulfied 59 in it	0.004	0	44.386	0	0.551	0.001	0	0	0	50.736	0	0.001	0	0	0.001	0	0	0.005	95.685
Main	68	Anhedral Pyrite	Pyrite near free Au grain	0.038	0	45.389	0.006	0.021	0	0	0	0	52.462	0	0.015	0	0	0.006	0	0	0.043	97.98
Euhedral (Late?)	28	Early Pyrite	5 µm euhedral bright pyrite	0.857	0	43.105	0.069	0.273	0.006	0.001	0	0.005	53.923	0	0	0.01	0	0.055	0	0	0.976	99.28
Euhedral (Late?)	63	Late Pyrite	Euhedral fine pyrite	0.086	0	42.551	0.058	7.964	0	0	0	0.093	46.347	0	0	0	0	0.029	0	0	0.098	97.226
Late	24	Late Veining	Light pyrite veining in large pod cutting and surrounding 2	0.008	0.002	46.265	0.031	0.164	0.003	0.007	0	0	53.156	0	0	0	0	0.001	0	0	0.009	99.646
Late	25	Atoll Marcasite	Atoll pyrite	0.134	0	43.56	0	0.074	0	0.001	0	0	51.474	0	0.011	0	0	0.026	0	0	0.152	95.432
Late	27	Atoll Marcasite	Atoll pyrite	0.083	0	43.937	0	0.068	0.002	0	0	0	51.487	0	0	0.007	0	0.014	0	0	0.094	95.692
Late	30	Marcasite Rim	Irregular 2-5 µm rim on 9	0.484	0	41.774	0.061	0.838	0	0.023	0	0	47.673	0.019	0	0	0	0.016	0	0	0.552	91.44
Late	32	Late Veining	Intersection of two µm-scale late maracsite veinlets in a marcasite stockwork	0.06	0	43.107	0.112	0.75	0	0.004	0	0.006	50.878	0.031	0	0	0	0.008	0	0	0.068	95.024
Late	33	Atoll Marcasite	Irregular atoll rimming on silicates	0.027	0	39.36	0	3.589	0.011	0.013	0	0.12	38.308	0.005	0.014	0.001	0	0.021	0	0	0.031	81.5
Late	34	Marcasite Core	Fine anhedral pyrite rimmed by atoll pyrite	0.057	0	42.444	0	3.579	0	0.023	0	0.067	50.576	0.009	0	0.004	0	0.022	0	0	0.065	96.846
Late	35	Atoll Marcasite	Atoll Pyrite	0.029	0.001	43.647	0.119	2.058	0.017	0.018	0	0.025	50.61	0.01	0.01	0.009	0.093	0.013	0	0	0.033	96.692
Late	36	Anhedral Marcasite	Large pod of anhedral pyrite	0.018	0	44.304	0.197	0.856	0.007	0.015	0	0.035	50.991	0	0.005	0	0.013	0.022	0	0	0.021	96.484
Late	37	Anhedral Marcasite	Edge of anhedral pyrite mass (#37-39)	0.011	0.003	43.853	0.103	1.692	0.018	0.012	0	0.061	50.548	0	0.004	0	0.007	0.007	0	0	0.013	96.332
Late	38	Anhedral Marcasite	Core of anhedral pyrite mass (#37-39)	0.005	0.002	43.598	0.223	2.32	0	0.008	0	0.062	50.438	0.007	0.013	0	0.024	0.014	0	0	0.005	96.719
Late	39	Anhedral Marcasite	Edge of anhedral pyrite mass (#37-39)	0.012	0.001	43.087	0.151	2.628	0	0.008	0	0.074	50.313	0.002	0.018	0.002	0.07	0.012	0	0	0.014	96.392
Late	40	Late Veining	Late marcasite vein cutting chalcopyrite	0.049	0.007	44.879	0.381	0	0.003	0	0	0	51.52	0.005	0	0.007	0	0.015	0	0	0.056	96.922
Late	50	Marcasite Rim	Thin pyrite rim along 51	2.232	0.006	42.684	0.013	0.168	0	0	0	0	47.33	0.01	0	0	0	0.011	0	0	2.543	94.997

Late	51	Marcasite Rim	Thick pyrite rim outside of 50	0.025	0	43.991	0.032	0.067	0.001	0.013	0	0	51.234	0.001	0.021	0	0	0.031	0	0	0.028	95.444
Late	64	Atoll Marcasite	Botryoidal pyrite	0.074	0	44.107	0.029	4.383	0	0.002	0	0.012	48.435	0	0	0	0	0.007	0	0	0.084	97.133
Late	65	Anhedral Marcasite	Core of pyrite pod	0.01	0.006	44.017	0.02	0.11	0	0	0	0	50.864	0.001	0.012	0	0	0.005	0	0	0.012	95.057
Late	66	Marcasite Rim	Rim around 65	0.327	0	42.927	0	0.493	0	0.007	0	0.007	48.911	0.02	0	0.002	0	0.039	0	0	0.373	93.106
Late	72	Anhedral Marcasite	Light color late pyrite pod	0.069	0	46.168	0.017	0.043	0	0	0	0	56.279	0	0	0	0	0.015	0	0	0.078	102.67
Standard	45		Pyrite Standard	0.018	0	45.902	0.032	0	0	0	0	0	52.529	0	0	0.003	0	0.001	0	0	0.02	98.505
Standard	46		Chalcopyrite Standard	0.021	0.009	30.185	34.04	0	0	0.016	0	0	34.708	0.004	0	0.002	0	0	0	0	0.024	99.01
Standard	47		Chalcocite Standard	0.014	0.114	0.004	89.14	0	0	0.065	0	0	20.392	0	0	0	0	0	0	0	0.016	109.75

Table 2. Table of pyrite and marcasite analyzed. Note that description is based on best analyses under scanning electron microscopy and could not differentiate pyrite from marcasite. Values in grey are below the average detection limit for the pyrites analyzed. Totals <96% and >102% are highlighted in red.

Mineral	ID #	Si	Ag	Fe	Cu	As	Hg	Zn	Au	Sb	S	Sn	W	Te	Bi	Ca	Tl	Pb	O	Total
Arsenopyrite	73	0.013	0	34.941	0.03	40.54	0	0.003	0	0.012	21.87	0	0.036	0.008	0	0.005	0	0	0.015	97.473
Tennantite	18	0	0.044	5.252	35.534	4.036	0.021	7.964	0	20.081	25.353	0.042	0	0	0	0	0	0	0	98.327
Bismuth Telluride	54	0.051	0.139	2.029	0	0	0	0	0	0	5.483	0	0	28.503	51.497	0	0	6.483	0.058	94.243
Bismuth Telluride	55	0.083	0.028	3.503	0	0	0	0.003	0	0	7.855	0	0	25.944	48.598	0	0	6.844	0.095	92.953
Bismuth Telluride	56	0.042	0.023	3.314	0	0	0	0.005	0	0	5.888	0	0	28.132	52.16	0	0	4.307	0.047	93.918
Bismuth Telluride	57	0.054	0.013	8.578	0	0	0	0	0	0	11.871	0	0	22.043	40.519	0	0	6.121	0.062	89.261
Bismuth Telluride	59	0.061	0.173	3.556	0.058	0	0	0	0	0	6.651	0	0	28.061	51.778	0	0	3.276	0.069	93.683
Bismuth Telluride	61	0.095	0.372	4.037	0.239	0	0	0	0	0	7.645	0	0	28.693	51.418	0	0	3.599	0.109	96.207
Chalcopyrite	**19**	**0.054**	**0.039**	**29.285**	**33.067**	**0**	**0**	**0.019**	**0.008**	**0.003**	**34.821**	**0**	**0**	**0.006**	**0**	**0.033**	**0**	**0**	**0.061**	**97.396**
Chalcopyrite	**20**	**0.012**	**0.03**	**30.861**	**31.519**	**0.018**	**0**	**0.03**	**0.001**	**0.004**	**33.119**	**0.002**	**0**	**0**	**0**	**0.018**	**0**	**0**	**0.013**	**95.627**
Gold	52	1.552	0	3.08	0	0.009	1.224	0	79.023	0	2.841	0	0	0	0.652	0.062	0	0	1.768	90.211
Gold	53	3.066	0	5.716	0.037	0.01	0.936	0.02	54.691	0	5.848	0	0	0	0.314	0.094	0	0	3.493	74.225
Gold	67	0.112	0	2.125	0	0	1.602	0	94.647	0	0.735	0	0	0	0.7	0.015	0	0	0.127	100.063

Table 3. Microprobe analyses on elements other than pyrite. All elements are reported in weight percent. Gold was detected above the detection limit of 0.0027% in sample 19. In samples 1-20 Au was identified in the PET-H, the method used at the time of analyses at the lab. However, during this study, it was identified that it is better to analyze gold in the LIF-H because there may be peak overlaps between gold and iron in the PET-H. For this reason spot analyses 1-18 on pyrite are not reported. Chalcopyrite samples 19 and 20 are included because they were the only chalcopyrite analyses. It is possible that the 80 ppm Au identified in sample 19 is a result of peak overlap, however, this is higher than was identified in other samples, and may indicate some gold in chalcopyrite.

Appendix 2: Spearman Correlation Matrix								
	Au	Ag	Al	As	Ba	Bi	Be	Ca
Ag	0.303	1						
Al	-0.105	-0.169	1					
As	0.326	0.439	-0.146	1				
Ba	-0.259	-0.211	0.328	-0.246	1			
Bi	0.458	0.416	-0.306	0.168	-0.278	1		
Be	-0.15	-0.186	0.615	-0.375	0.424	-0.206	1	
Ca	0.059	-0.062	-0.201	-0.427	-0.007	0.243	0.239	1
Cd	0.294	0.556	0.147	0.343	-0.032	0.177	0.064	-0.075
Ce	-0.048	-0.132	0.562	0.066	0.236	-0.197	0.402	-0.156
Co	0.34	0.06	0.094	0.058	0.028	0.173	0.292	0.26
Cr	0.086	-0.103	-0.002	0.238	0.162	-0.112	-0.134	-0.429
Cs	0.077	-0.096	0.263	-0.287	0.266	0.032	0.622	0.391
Cu	0.245	0.463	-0.109	0.286	0.061	0.329	-0.159	0.008
Fe	0.39	0.114	0.021	0.356	-0.037	0.154	0.232	0.131
Ga	-0.108	-0.19	0.886	-0.05	0.325	-0.275	0.509	-0.265
Ge	0.186	-0.023	0.296	0.13	0.283	-0.036	0.337	-0.033
Hf	0.121	0.009	0.428	0.174	0.185	0.037	0.169	-0.272
Hg	0.183	0.374	-0.121	0.522	-0.261	0.144	-0.412	-0.311
In	0.57	0.34	0.072	0.289	-0.194	0.412	0.038	0.16
K	-0.223	-0.203	0.356	-0.356	0.463	-0.25	0.594	0.188
La	-0.048	-0.182	0.407	0.092	0.282	-0.186	0.302	-0.176
Li	0.098	0.035	0.176	0.078	-0.121	0.223	0.121	-0.089
Mg	-0.044	-0.108	-0.163	-0.449	0.08	0.097	0.26	0.834
Mn	0.192	0.085	-0.147	-0.23	-0.174	0.289	0.27	0.747
Na	-0.017	-0.161	0.349	-0.292	0.357	-0.174	0.568	0.231
Nb	-0.065	-0.241	0.766	-0.152	0.371	-0.23	0.442	-0.239
Ni	0.25	-0.082	0.217	0.064	0.195	-0.011	0.292	0.032
Mo	0.317	0.092	0.101	0.283	-0.082	0.075	-0.124	-0.316
P	0.087	-0.174	0.285	0.101	0.35	-0.178	0.201	-0.155
Pb	0.125	0.488	0.334	0.286	0.02	0.003	0.196	-0.203
Rb	-0.225	-0.195	0.254	-0.315	0.423	-0.191	0.544	0.166
Re	0.45	0.115	0.138	0.18	-0.092	0.117	0.084	-0.037
S	0.351	0.084	0.189	0.339	-0.084	-0.049	0.057	-0.142
Sb	0.254	0.493	-0.322	0.655	-0.282	0.323	-0.488	-0.35
Se	-0.041	-0.054	-0.007	0.082	0.269	0.074	-0.043	-0.081
Sn	0.551	0.395	0.125	0.242	-0.206	0.476	0.166	0.192
Sr	0.013	-0.134	0.032	0.001	0.094	0.022	0.041	-0.109
Ti	-0.036	-0.28	0.545	0.019	0.393	-0.189	0.206	-0.32
Ta	-0.091	-0.186	0.826	-0.161	0.292	-0.254	0.521	-0.208
Th	-0.119	-0.152	0.879	-0.118	0.29	-0.308	0.581	-0.213
Te	0.514	0.237	-0.063	0.394	-0.117	0.412	-0.167	-0.267
Tl	0.22	0.144	0.125	0.44	0.019	-0.039	-0.067	-0.382
U	0.154	-0.126	0.397	0.189	0.258	-0.148	0.175	-0.306
V	0.037	-0.259	0.141	0.183	0.262	-0.187	-0.025	-0.395
W	0.299	0.421	-0.109	0.534	-0.316	0.301	-0.248	-0.176
Y	0.166	-0.158	0.374	-0.02	0.348	-0.074	0.407	-0.022
Zn	0.311	0.317	0.134	0.098	-0.039	0.179	0.315	0.317
Zr	0.043	-0.026	0.246	0.201	0.217	0.02	0.088	-0.284

Appendix 2: Spearman Correlation Matrix Continued								
	Cd	Ce	Co	Cr	Cs	Cu	Fe	Ga
Ag								
Al								
As								
Ba								
Bi								
Be								
Ca								
Cd	1							
Ce	0.048	1						
Co	0.316	0.173	1					
Cr	-0.018	0.074	0.113	1				
Cs	0.032	0.203	0.352	0.01	1			
Cu	0.309	-0.09	0.249	0.14	-0.102	1		
Fe	0.222	0.274	0.577	0.153	0.336	0.114	1	
Ga	0.07	0.551	0.056	0.113	0.206	-0.04	0.052	1
Ge	0.179	0.414	0.356	0.417	0.376	0.157	0.525	0.356
Hf	0.085	0.361	0.106	0.375	0.099	0.184	0.106	0.491
Hg	0.33	-0.016	-0.074	0.047	-0.4	0.307	0.053	-0.115
In	0.39	0.123	0.294	-0.144	0.155	0.238	0.471	-0.005
K	-0.109	0.268	0.074	0.058	0.711	-0.228	0.102	0.316
La	-0.043	0.91	0.154	0.255	0.178	-0.04	0.289	0.445
Li	0.028	0.192	0.189	0.012	0.027	0.129	0.054	0.213
Mg	-0.094	-0.154	0.19	-0.304	0.505	-0.071	0.09	-0.229
Mn	0.133	-0.061	0.513	-0.455	0.392	-0.018	0.375	-0.274
Na	-0.04	0.223	0.12	0.001	0.554	-0.294	0.252	0.258
Nb	0.069	0.446	0.057	0.148	0.206	-0.063	-0.007	0.787
Ni	0.211	0.206	0.755	0.448	0.289	0.232	0.497	0.168
Mo	0.164	-0.013	0.048	0.311	-0.132	0.198	0.134	0.083
P	0.028	0.319	0.222	0.501	0.09	0.195	0.199	0.36
Pb	0.573	0.196	0.055	-0.108	0.02	0.033	0.126	0.257
Rb	-0.164	0.265	0.086	0.1	0.728	-0.21	0.123	0.253
Re	0.281	0.098	0.548	0.345	0.181	0.25	0.353	0.175
S	0.171	0.258	0.392	0.334	0.09	0.125	0.446	0.214
Sb	0.241	-0.167	-0.143	0.077	-0.439	0.349	0.078	-0.258
Se	-0.094	-0.005	-0.001	0.336	0.001	0.258	0.034	0.137
Sn	0.413	0.13	0.358	-0.205	0.262	0.171	0.44	0.048
Sr	-0.114	0.11	-0.094	0.194	0.091	-0.105	0.007	0.064
Ti	-0.068	0.45	0.051	0.509	0.138	0.055	0.087	0.645
Ta	0.122	0.452	0.021	-0.06	0.196	-0.145	-0.031	0.795
Th	0.155	0.629	0.049	-0.063	0.21	-0.163	0.05	0.792
Te	0.209	-0.045	0.123	0.378	0.006	0.114	0.295	0.019
Tl	0.167	0.236	0.199	0.395	0.133	0.097	0.284	0.185
U	0.181	0.368	0.234	0.499	0.122	0.17	0.187	0.414
V	-0.165	0.225	0.022	0.788	0.066	0.062	0.133	0.303
W	0.222	0.046	0.007	-0.148	-0.321	0.189	0.245	-0.123
Y	0.169	0.411	0.492	0.497	0.382	0.13	0.373	0.407
Zn	0.611	0.121	0.684	-0.14	0.269	0.194	0.516	0.004
Zr	-0.007	0.311	0.086	0.49	0.107	0.188	0.126	0.353

Appendix 2: Spearman Correlation Matrix Continued								
	Ge	Hf	Hg	In	K	La	Li	Mg
Ag								
Al								
As								
Ba								
Bi								
Be								
Ca								
Cd								
Ce								
Co								
Cr								
Cs								
Cu								
Fe								
Ga								
Ge	1							
Hf	0.277	1						
Hg	-0.068	0.094	1					
In	0.241	0.127	0.231	1				
K	0.273	0	-0.42	-0.188	1			
La	0.463	0.35	-0.069	0.045	0.246	1		
Li	0.009	0.244	0.113	0.13	-0.106	0.174	1	
Mg	-0.023	-0.269	-0.363	-0.036	0.407	-0.184	-0.234	1
Mn	-0.009	-0.275	-0.174	0.325	0.066	-0.173	0.007	0.629
Na	0.259	0.038	-0.33	0.081	0.671	0.159	-0.204	0.323
Nb	0.298	0.46	-0.152	-0.016	0.302	0.37	0.203	-0.205
Ni	0.495	0.273	-0.104	0.19	0.073	0.274	0.139	0.009
Mo	0.134	0.252	0.206	0.289	-0.21	0.004	0.022	-0.319
P	0.461	0.432	-0.063	0.067	0.112	0.426	0.087	-0.224
Pb	0.161	0.017	0.227	0.249	0.029	0.088	0.001	-0.194
Rb	0.265	0.006	-0.42	-0.225	0.959	0.276	-0.059	0.402
Re	0.409	0.224	0.039	0.277	-0.032	0.094	0.096	-0.096
S	0.449	0.155	0.057	0.295	-0.009	0.28	0.064	-0.181
Sb	-0.136	0.111	0.551	0.182	-0.534	-0.121	0.051	-0.373
Se	0.333	0.142	-0.055	-0.111	0.09	0.157	-0.03	-0.073
Sn	0.235	0.176	0.183	0.84	-0.138	0.027	0.217	0.018
Sr	0.116	0.04	-0.04	-0.14	0.328	0.163	-0.023	-0.006
Ti	0.421	0.637	-0.094	-0.064	0.23	0.502	0.165	-0.235
Ta	0.24	0.324	-0.135	0.035	0.304	0.312	0.207	-0.219
Th	0.267	0.355	-0.078	0.064	0.318	0.442	0.129	-0.19
Te	0.265	0.234	0.153	0.234	-0.113	0.005	-0.027	-0.224
Tl	0.31	0.264	0.286	0.104	0.189	0.276	0.046	-0.26
U	0.4	0.516	0.092	0.124	0.089	0.437	0.138	-0.305
V	0.386	0.453	-0.092	-0.159	0.162	0.405	0.035	-0.259
W	-0.089	0.085	0.469	0.441	-0.485	0.002	0.239	-0.333
Y	0.594	0.453	-0.206	0.07	0.263	0.484	0.144	-0.015
Zn	0.265	-0.031	0.015	0.458	-0.013	0.04	0.107	0.21
Zr	0.303	0.921	0.056	0.025	0.035	0.368	0.186	-0.236

Appendix 2: Spearman Correlation Matrix Continued								
	Mn	Na	Nb	Ni	Mo	P	Pb	Rb
Ag								
Al								
As								
Ba								
Bi								
Be								
Ca								
Cd								
Ce								
Co								
Cr								
Cs								
Cu								
Fe								
Ga								
Ge								
Hf								
Hg								
In								
K								
La								
Li								
Mg								
Mn	1							
Na	0.202	1						
Nb	-0.241	0.308	1					
Ni	0.151	0.138	0.18	1				
Mo	-0.222	0.021	0.192	0.239	1			
P	-0.273	0.149	0.358	0.512	0.229	1		
Pb	-0.01	0.07	0.132	0.021	0.07	-0.082	1	
Rb	0.061	0.576	0.221	0.067	-0.267	0.082	-0.017	1
Re	0.068	0.085	0.182	0.542	0.434	0.329	0.166	-0.057
S	-0.042	0.099	0.132	0.463	0.299	0.369	0.229	-0.037
Sb	-0.221	-0.478	-0.312	-0.109	0.26	-0.106	0.15	-0.479
Se	-0.293	-0.083	0.112	0.165	-0.061	0.314	-0.115	0.148
Sn	0.389	0.09	0.021	0.19	0.173	-0.033	0.345	-0.148
Sr	-0.217	0.237	0.148	-0.092	0.084	0.098	-0.091	0.33
Ti	-0.422	0.206	0.734	0.295	0.202	0.532	-0.016	0.208
Ta	-0.138	0.325	0.874	0.094	0.152	0.209	0.295	0.195
Th	-0.115	0.349	0.709	0.127	0.067	0.249	0.351	0.217
Te	-0.188	0.006	0.059	0.206	0.377	0.15	0.137	-0.097
Tl	-0.232	0.097	0.14	0.193	0.177	0.169	0.153	0.219
U	-0.331	0.093	0.464	0.518	0.383	0.561	0.047	0.049
V	-0.527	0.094	0.33	0.394	0.312	0.572	-0.18	0.201
W	0.031	-0.258	-0.163	-0.06	0.183	-0.098	0.222	-0.457
Y	-0.018	0.229	0.444	0.661	0.113	0.601	0.04	0.268
Zn	0.55	0.092	-0.021	0.561	0.015	0.046	0.365	-0.049
Zr	-0.33	0.01	0.351	0.286	0.181	0.479	-0.107	0.09

Appendix 2: Spearman Correlation Matrix Continued								
	Re	S	Sb	Se	Sn	Sr	Ti	Ta
Ag								
Al								
As								
Ba								
Bi								
Be								
Ca								
Cd								
Ce								
Co								
Cr								
Cs								
Cu								
Fe								
Ga								
Ge								
Hf								
Hg								
In								
K								
La								
Li								
Mg								
Mn								
Na								
Nb								
Ni								
Mo								
P								
Pb								
Rb								
Re	1							
S	0.697	1						
Sb	-0.043	-0.003	1					
Se	0.054	0.068	-0.002	1				
Sn	0.298	0.237	0.149	-0.158	1			
Sr	-0.016	-0.012	-0.131	0.139	-0.123	1		
Ti	0.184	0.192	-0.128	0.31	-0.1	0.225	1	
Ta	0.151	0.167	-0.342	-0.049	0.106	0.037	0.497	1
Th	0.112	0.176	-0.31	-0.095	0.123	-0.024	0.424	0.836
Te	0.368	0.311	0.339	0.217	0.216	0.186	0.178	-0.054
Tl	0.289	0.438	0.188	0.092	0.105	0.26	0.259	0.056
U	0.434	0.375	-0.046	0.264	0.065	0.09	0.55	0.368
V	0.274	0.306	0.032	0.451	-0.256	0.249	0.71	0.072
W	-0.023	0.056	0.64	-0.125	0.429	-0.176	-0.135	-0.128
Y	0.481	0.392	-0.266	0.279	0.108	0.059	0.552	0.313
Zn	0.355	0.289	-0.011	-0.183	0.495	-0.289	-0.183	0.079
Zr	0.171	0.118	0.15	0.238	0.059	0.083	0.65	0.142

Appendix 2: Spearman Correlation Matrix Continued								
	Th	Te	Tl	U	V	W	Y	Zn
Ag								
Al								
As								
Ba								
Bi								
Be								
Ca								
Cd								
Ce								
Co								
Cr								
Cs								
Cu								
Fe								
Ga								
Ge								
Hf								
Hg								
In								
K								
La								
Li								
Mg								
Mn								
Na								
Nb								
Ni								
Mo								
P								
Pb								
Rb								
Re								
S								
Sb								
Se								
Sn								
Sr								
Ti								
Ta								
Th	1							
Te	-0.093	1						
Tl	0.063	0.339	1					
U	0.346	0.229	0.299	1				
V	0.025	0.366	0.368	0.596	1			
W	-0.081	0.144	0.064	-0.046	-0.154	1		
Y	0.33	0.208	0.223	0.587	0.522	-0.218	1	
Zn	0.154	0.026	-0.01	0.107	-0.275	0.165	0.307	1
Zr	0.173	0.229	0.291	0.49	0.575	0.043	0.446	-0.116